地震研究所彙報
Bull. Earthq. Res. Inst.
Univ. Tokyo
Vol. 71 (1996) pp. 103–226

Study on the Propagation of Love Waves across Irregular Structures of the Moho Discontinuity

Mitsuru YOSHIDA

Earthquake Research Institute, University of Tokyo

(Received August 14, 1996)

Abstract

Propagation of Love waves across irregular structures with sloping angles of the Moho discontinuity is investigated with particular attention given to the characteristics of phase velocities, its directional dependence and scattering. The structures under investigation are exemplified by such sloping structures as those seen at mountain roots and the Moho discontinuity in the continental margins between two continental plates. A finite difference method is applied to solve problems using numerical simulations.

It is assumed that the mountain root structure has a Moho discontinuity, which protrudes into the mantle with a slope of 20–30 degrees, while the Earth's free surface is assumed to be a plane. In the computation scheme, two- and three-dimensional second order partial derivative equations are approximated by a central difference representation. Displacement and stress continuities are assumed as the boundary condition between media having different elastic properties. The accuracy of the numerical simulation is regorously examined with respect to transmission coefficients and phase velocities, compared to the analytical solutions obtained for a vertical boundary model and a uniform wave guide.

Phase velocities calculated from Fourier transformations over the concave interface expose various distinct anomalies, which are somewhat different from those of the transitional zone of an ocean-continent obtained by BOORE (1970). The phase velocity shows a slight increase with an increase of the period when waves propagate from the windward (wave's incoming direction) edge of the mountain foot to the center of the deep mountain root area. On the other hand, from the mountain root area to the leeward (wave's propagating direction) mountain foot, the phase velocity increases greatly with the increase of period. In the shorter period range, the phase velocity for the windward path towards mountain root area is higher than that from the mountain root area towards the leeward edge. In the longer period range, the relationship between phase velocity and period is reversed.

The phase velocity dispersion curves for both models with linear and the stepwise interface boundary across the mountain root are calculated. Defining the propagation from the thinner to thicker crust as a downdip propagation and the reverse case as an updip propagation, the mean phase velocity dispersion curve for the path through the mountain root follows the middle of the two curves for downdip and updip propagations. The mean phase velocity dispersion curve approaches those for the thickest (D-structure) and the thinnest (S-structure) horizontally-layered structures at short and long periods, respectively. To interpret the mean phase velocity in terms of a horizontally layered structure, the "weighting coefficient" to construct synthetic elastic parameters is introduced. The weighting coefficient is defined as the ratio of the area possessing an arbitrary medium to the area of the laterally heterogeneous layer.

The phase velocity anomaly and the directional dependence can be explained by spectral phase shifts between nonuniform and uniform wave guides. These spectral phase shifts are oscillated along the interface to a small extent at the windward edge, a moderate extent at the central mountain area and a large extent at the leeward edge area. The tomographic snap shots of particle displacement

of Love waves clearly show that interference between the incident and scattered waves produces peculiar phase and amplitude distributions on the free surface, as well as near the irregular boundaries of the Moho discontinuity. They also show that interference between the waves of multiple scattering generated at different irregular boundaries makes new incorporated scattered waves.

The scattered waves, consisting of transmitted waves, reflected waves, diffracted waves and body waves, possess two resonance wavelengths. One is the resonance caused by the coupling between the interface and the uniform wave guide. The other is the resonance related only to the uniform wave guide. The scattering characteristics of Love waves are in harmony with those of shallow water waves in a semi-circular bay that flanks a continental shelf. The energy of the scattered waves on the free surface is largest at the leeward edge, intermediate at the center and weakest at the windward edge along the interface. These energy partition corresponds well to the magnitude of the spectral phase shifts of Love waves on the free surface.

To analyze the amplitude components of Love waves across the mountain root structure, the transmission and reflection coefficients were calculated taking into consideration multiple reflections inside the concave interface. For a concave structure whose slopes consist of several steps, at the windward edge of the concave interface, the transmission coefficients can be explained by multiple reflections except at short periods. At the midpoint of the interface, the transmission coefficients can be explained by multiple reflections over the entire period range. At the leeward edge of the interface, the transmission coefficients cannot be explained by multiple reflections, especially at long periods.

On the other hand, body wave energy is predominantly radiated at short and long periods for the downdip and updip propagations, respectively. These results suggest that the transmission coefficients, which could not be explained by multiple reflections, are closely influenced by the radiation characteristics of body wave energy. For the concave structure whose slopes vary smoothly, the transmission coefficients over the interface can be explained well by the theory of multiple reflections, except at a few short periods. Furthermore, it is found that the transmission coefficients at the midpoint of the interface are very close to those of downdip propagation for the medium model with a step of the Moho discontinuity. The model consists of two media with different crustal thickness, one has the thinnest crust and the other the thickest crust for the mountain root structure. This result suggests that at the midpoint of the concave interface the interference of diffracted waves is weak. In this way, Love waves superimposed by scattered waves can be reasonably explained by the multiple reflection of Love waves and the diffraction of body waves.

The effects of narrow-width heterogeneous Moho boundaries in the transverse direction upon Love wave propagation over the mountain root structure were investigated using the three-dimensional (3-D) finite difference method. It is understood from 3-D simulations that the characteristics of the phase velocities and the transmission coefficients over the mountain root, for a period range from 20 to 50 sec, are almost equivalent to those for 2-D problems in the cases in which heterogeneous boundaries in the transverse direction are far from the great circle path by more than half the maximum wavelength of the incident waves, the sloping angle of heterogeneous boundaries in the transverse direction is less than thirty degrees, and that for the oblique incidence of the waves the angle of incidence is less than about thirty degrees. The radial and vertical components of scattered waves are effectively generated when the waves are obliquely incident upon irregular fronts. The maximum amplitudes of those waves are less than ten percent of those for the dominated transverse component. When the effects of the heterogeneous boundaries in the transverse direction are weak, the characteristics of the transmission coefficient for 3-D simulations agree well with those obtained from the ray theory of multiple reflections of Love waves inside the mountain root and more finely than those for 2-D simulations, especially at short periods near 20 sec.

Table of Contents

Preface

The problems of the propagation of surface waves for nonuniform wave guides are important because lateral heterogeneity abounds in the crust and the upper mantle of the earth. When surface waves encounter geometric irregularities in their path, scattered waves are excited. The scattered waves cause anomalies in propagating waves such as augumentation, attenuation and phase distortion. Therefore, precise knowledge concerning the effects of scattering on surface waves is indispensable to get detailed information about the heterogeneous structure of the media.

The scattering of Love waves was studied by MAL and HERREA (1965) for model with a rectangular constriction between a surface layer and half space, with respect to amplitude and phase perturbation. ALSOP (1966) and GREGERSEN and ALSOP (1974) analyzed transmission and reflection coefficients of Love waves for a model with a vertical discontinuity. ITS and YANOVSKAYA (1983) analyzed those coefficients in the case of inclined incidence on a curved interface of vertically inhomogeneous media. These theoretical studies, however, did not extend to discussions of the effects of scattering on phase velocity dispersion.

Large-scale lateral heterogeneities generally dominate at plate boundaries, such as the ocean to continent and the continent to continent boundaries. Using numerical methods, the propagation of Love waves for an ocean-continent type model was studied by BOORE (1970). He treated a model with a sloping transitional zone having a dip angle of 10° in welded contact between horizontal layers with thick (continent) and thin (ocean) crusts. The notable characteristics obtained in that study are that waves propagating into the thinning crust have anomalously high phase velocities and vice versa. However, the mechanism generating anisotropy was not fully investigated. Through numerical model experiments, LYSMER and DRAKE (1971), DRAKE and BOLT (1980), and BOLT and DRAKE (1986) studied Love wave propagation for a similar ocean-continent model with a subducting slab forming a dip angle of 45° and insisted that conversion from the fundamental to the first higher modes is strong in a limited short period range.

On the other hand, LEVANDER (1985) emphasized that Rayleigh waves in a continental sloping structure with a dip angle of 40° show stable and interpretable phase velocity dispersion without oscillations.

The present thesis investigates the propagation of Love waves across continental mountain root structures by means of the finite difference scheme. The model of the mountain root structure has a thick crust with the Moho discontinuity protruding into the mantle at a high dip angle 20°–30°. The thesis consists of five major parts.

In Part 1, phase velocities of Love waves propagating into the thinning and thickenning regions and over the whole interface are determined. The characteristics of the phase velocity anomaly, which are very different from those of the ocean-continent transitional zone, are found. The mean phase velocity dispersion curve over the interface is approximated by a horizontally layered structure using synthetic elastic parameters, produced by introducing "weighting coefficients."

In Part 2, the origin of the anisotropy is elucidated by inspecting variations of phase calculated at array stations over the interface. The fluctuations of the phase and amplitude components due to the scattering, inside and outside the interface, are shown visually with tomographic snap shots of particle displacements.

In Part 3, the mechanism generating the scattering is studied. Discussions mainly concentrate on interference between the scattered waves generated at different locations of the interface, which plays an important role in the generation of a new scattered wave. Finally, the dispersion characteristics and the energy partition of the scattered waves are investigated with special attention to the scattering characteristics of long waves propagated along a continental shelf with a semi-circular bay, obtained by MOMOI (1981). Analogy between Love waves and long waves is discussed.

In Part 4, the transmission and reflection coefficients of Love waves over the concave interface are quantitatively studied. Taking into consideration the effects of multiple reflections of Love waves inside the interface, the theory for computing location-dependent transmission coefficients is developed and applied to the interpretation of Love waves over the interface. The energy partitioned into body waves is also investigated for the downdip and updip propagations. On the basis of this information, Love waves over the concave interface, contaminated by scattered waves, can be explained in detail by the combination of the multiple reflection of Love waves and the diffraction of body waves.

In Part 5, the effects of heterogeneous Moho boundaries in the transverse direction upon the propagation of Love waves are quantitatively studied using the three-dimensional (3-D) finite difference method. Typical topographical situations of 3-D media, in which the characteristics of phase velocities and transmission coefficients over the mountain root are almost equivalent to those of 2-D problems, are found through 3-D simulations based on many kinds of 3-D media with tilted or vertical boundaries in the transverse direction. Scattered waves of P–SV components, generated due to the heterogeneous boundaries in the transverse direction, are shown together with the predominant Love waves.

Part 1

Phase Velocity Anomaly of Love Waves across Irregular Structures of the Moho Discontinuity

1.1 Introduction

Problems of Love wave propagation in laterally heterogeneous media, such as reflection, transmission and scattering at vertical or sloping discontinuities, have been theoretically investigated hitherto (SATO, 1961; HUDSON and KNOPOFF, 1964; KNOPOFF and HUDSON, 1964; ALSOP, 1966; ISHII and YAMAZAKI, 1973; ITS and YANOVSKAYA, 1983, 1985). These problems were mainly solved using the Green function technique and the representation theorem.

Paying attention to sloping structures, interesting results have been obtained such that phase velocities dependent on propagation direction (anisotropy) appear in Love (BOORE, 1970) and Rayleigh waves (LEVANDER, 1985) travelling transitional zones with slope angles of 10° or 20°, while anisotropy does not appear clearly in the case of much lower dipping layers of less than 3° (YAMAZAKI and ISHII, 1973; ISHII and YAMAZAKI, 1973).

SATO (1966) derived phase and group velocity dispersion formulae for media with a transitional zone. The formula determines phase velocity only from the thickness below the observation point (X)

$$(X, \omega) = C(H, \omega),$$

where $C(H, \omega)$ is the phase velocity of the horizontal layer with the thickness H at angular frequency ω. However, from the model experiment on dispersive Rayleigh waves propagating in Plastic–Aluminum (P–A model) with dipping boundary, ABE and SUZUKI (1970) concluded that the analysis of observed group velocity does not support the formula of SATO (1966) for the case of a dip angle of 7.0°.

In this P–A model, whose velocity contrast is strong, YAMAZAKI and ISHII (1973) suggested that there is a considerable contribution from higher modes in the theoretical seismograms.

The irregular structures between the ocean-continent boundary have been studied using the finite element method by several authors: LYSMER and DRAKE (1971) studied the energy partition of incident oceanic Love waves of the fundamental mode and found that at a period of 25 sec, on the oceanic side of the model including the dipping slab, the total energy in the reflected modes is found to be approximately 1–3 percent of the incident energy, and the one in the transmitted higher modes to be 34–36 percent of the incident energy. Analyzing a similar transitional zone, DRAKE and BOLT (1980) found that between periods of 20 and 11 sec, 90 percent of the energy of fundamental mode Love waves incident from the oceanic side is transmitted as the first higher mode.

BOLT and DRAKE (1986) confirmed that, in the propagation of Love waves from the ocean to the continent, a subduction zone with a dip angle of 45° significantly

scatters, at short periods, the energy of Love waves of the fundamental mode into that of the first higher mode.

Using the finite difference method, LEVANDER (1985) investigated Rayleigh wave propagation in continental structures with irregular boundaries. He found that a slope of the lithosphere–asthenosphere boundary of 30–40° produced a minor directional dependence (2–4% at periods of about 50 sec) in Rayleigh wave phase velocities measured from updip and downdip travelling waves. The directional dependence is usually less than half that observed in numerical experiments of Love wave propagation in a similar structure.

It is understood from these numerical model studies of surface waves that in laterally heterogeneous media, Rayleigh waves exhibit very stable and interpretable dispersions, even in irregular structures with a dip angle of about 40° (LEVANDER, 1985), while Love waves produce unstable dispersion with oscillations in the sloping layers with a dip angle of 10° (BOORE, 1970), which is significantly outside the lower and upper limits of the dispersion curves for the two extreme uniform wave guides in the irregular structures.

The anomaly of Love wave dispersion in the irregular structures might be caused by the effects of strong scattering generated at the irregular layer boundaries. However, the effects of scattered waves on Love wave velocity have not been studied. On the other hand, Love wave velocities propagated along the great circle are conventionally used for studying the regional and global crust and/or mantle structures. Considering this situation, it is very important to develop a study of the relationship between the velocity and the scattering of Love waves propagated in irregular structures with sloping layer boundaries having high dip angles of more than 10°.

In this chapeter we investigate problems associated with the propagation of Love waves across irregular structures with a surface layer forming a concave structure into the downward portion and sloping layer boundaries having dip angles of 20–30° and 90°. The main subjects investigated are the essential properties of phase velocities of Love waves propagated in irregular crustal structures; namely, the existence and the characteristics of phase velocity anisotropy, relations between phase velocities (apparent phase velocities) and irregular crustal structures and constraints on approximating irregular structures with horizontal layers. To study these subjects we use the finite difference method, because it permits us to use the surface wave eigenfunction for the incident wave and we can work with complex structures. Furthermore, we can obtain the spatio-temporal variations of the whole space of seismic wave fields from the surface to the inner parts of the crust and mantle.

The numerical methods are also used in engineering seismology for studying seismic response of the ground surface. Therefore, at this point we briefly review the kinds and the characteristics of numerical methods. The numerical methods are classified into the following groups (KOKETSU and TAKENAKA, 1989; OHORI *et al.*, 1990; HORIKE *et al.*, 1990; HISADA *et al.*, 1991; TAKENAKA, 1993, 1995).

(1) The interior method:

A) The finite difference method (FDM) (BOORE, 1972; SATO, 1972; VIRIEUX, 1984; LEVANDER, 1985; VIDALE and HELMBERGER, 1988; YAMANAKA *et al.*, 1989; YOSHIDA, 1993; YOSHIDA and YAMADA, 1993).

B) The finite element method (FEM) (LYSMER and DRAKE, 1971; GELLER *et al.*, 1979; ZAMA, 1981; SUZUKI and HAKUNO, 1984; BOLT and DRAKE, 1986).

C) The spectral method (BERG and SKOVGAARD, 1990; DAUDT *et al.*, 1989; KOSLOFF *et al.*, 1984; FURUMURA and TAKENAKA, 1992).

(2) The boundary method:

D) The Aki–Larner method (AKI and LARNER, 1970; BOUCHON and AKI, 1977; BARD and BOUCHON, 1980a, b; KOKETSU, 1987; HORIKE, 1988).

E) The boundary integral equation method (BIEM) (WONG, 1979; SANCHEZ-SESMA and ESQUIVEL, 1979; DRAVINSKI, 1982).

F) The boundary element method (BEM) (BANERJEE and BUTTERFIELD, 1977; HISADA *et al.*, 1991).

G) The discrete wavenumber boundary element method (BOUCHON, 1985; KAWASE, 1988).

H) The T-matrix method (WATERMAN, 1969, 1976).

(3) The wavefunction method (TRIFUNAC, 1971; SANCHEZ-SESMA, 1985) for a semi-circular type structure.

(4) The Gaussian beam method (ČERVENÝ, 1983; YOMOGIDA, 1989) with distributed energy, based on the ray theory.

(5) The hybrid method represented by the combination of FEM+BEM (KELLY *et al.*, 1979) and Normal Mode Method+FEM (REGAN and HARKRIDER, 1989).

The interior method (1) is suitable for investigating spatio-temporal variations of seismic wave fields in complex structures. The boundary method (2) is employed for rather simple structures and can determine the wave motion in high accuracy. The wave function method (3) has a very fast computation time, but it can be applied in the limited topography of the medium. The Gaussian beam method (4) is useful for problems including the shadow zone or the caustic. However, determination of beam width is unresolved. The hybrid method (5) is applicable for the media with a transitional zone between homogeneous and inhomogeneous wave fields.

The Aki–Larner method (AKI andLARNER, 1970), using the fast Fourier transformation FFT, is a version of the Rayleigh–Fourier method, which is based on the Rayleigh hypothesis that the scattered field near and on an interface can be expanded in terms of plane waves propagating or exponentially damped in a single direction, namely, away from the interface (TAKENAKA, 1995). This method might not give the correct solution for media with a steep interface (SHINOZAKI, 1988).

The formulation of BEM is based on the representation theorem (e.g., AKI and RICHARDS, 1980). In BEM the Green's functions both for displacement and traction are used as weight functions. The boundary integral equations in the space domain are discretized by a similar technique to FEM. One of the biggest disadvantages of BEM is the time-consuming effort required to evaluate the Green function for a half

space (TAKENAKA, 1995).

As discussed by HORIKE *et al.* (1990), the choice of numerical method depends on type of incident wave, shape of interface, frequency range, and capacity and speed of the available computer.

Although the numerical methods described above are mainly applied to 2-D problems, some have been developed and used for 3-D problems. In engineering seismology, seismic responses of 3-D sedimentary basins are numerically studied by HORIKE *et al.* (1990), OHORI *et al.* (1990) using the Aki–Larner method, TOSHINAWA and OHMACHI (1992) with FEM, FRANKEL and VIDALE (1992) with FDM, KATO *et al.* (1993) with the Gaussian beam method, and HISADA *et al.* (1993) with BEM. In 2-D or 3-D analyses, amplitude increase and elongation of the duration on the sedimentary basin, due to the vertical incidence of S waves, are demonstrated at periods of 1–10 sec.

1.2 Models

We assume a surface layer over isotropic semi-infinite media in our simulation. The continental crust is thick, about 35 km, compared to the oceanic one of 6 km (e.g., GILLULY *et al.*, 1968; KANAMORI, 1982; UTSU, 1984).

Among continental structures, there seems to exist regions in which a uniform continental structure with a thick crust is adjacent to one with thicker crust having a dip angle of 90° (e.g., near the eastern Swiss Alps region (WERNER and KISSLING, 1988)), or the structure forms a great mountain range with the Moho discontinuity at high dip angles 30–90° (e.g., near the region of the Tibetan Plateau (CHEN and MOLNAR, 1981; HONDA and SAKAI, 1988)). Hence, we try to approximate the former with Model C (Fig. 1) and the latter with Models D (Fig. 1) and E (Fig. 6(d)). In Models D and E, the sloping structures are approximated by several steps and oblique lines, respectively. Model D makes modelling the sloping structure easy in terms of a horizontally layered structure, while Model E is used to compare scattering characteristics to those for Model D. Although we progress with studies for Models C, D and E in the present work, Models A and B in Fig. 1 are used to examine the stability and the accuracy of the numerical computation. Model B is also used for comparing present computational results with those previously obtained by several authors.

The Model B, named "Higuchi's Model" (HIGUCHI, 1932), has been frequently assumed for investigating reflections in the plane wave incident problems (SATO, 1961; ALSOP, 1966; BOOR, 1970) and consists of four different media contacting along a vertical line. Shear wave velocities and rigidities for layers L_1, L_2, L_3, and L_4 in this model are denoted by (β_1, μ_1), (β_2, μ_2), (β_3, μ_3) and (β_4, μ_4), respectively. There is the following relation.

$$\begin{aligned} (1/\beta_1)-(1/\beta_2)&=(1/\beta_3)-(1/\beta_4) \\ \mu_1/\mu_2&=\mu_3/\mu_4 \end{aligned} \tag{1.1}$$

where L_1 and L_3 are the crust with the thickness (H) of 35 km, L_2 and L_4 the mantle.

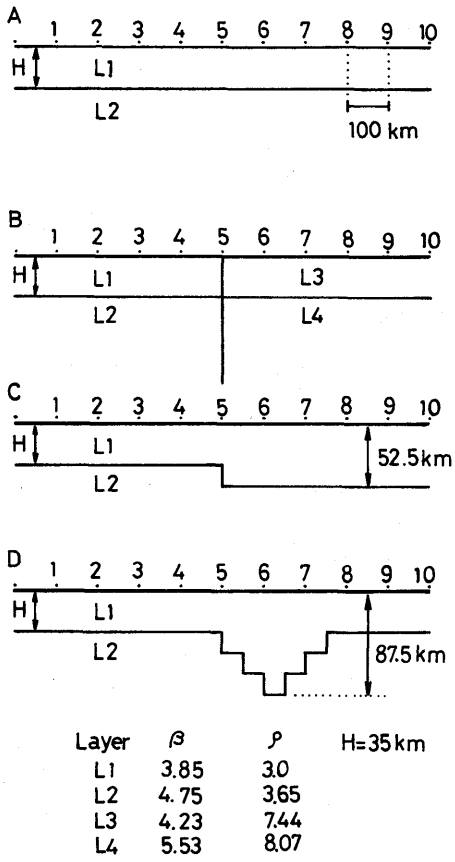

Layer	β	ρ	H=35 km
L1	3.85	3.0	
L2	4.75	3.65	
L3	4.23	7.44	
L4	5.53	8.07	

Fig. 1. Schematic diagrams of two-dimensional elastic models. A: the uniform wave guide model with two layers, B: the model by HIGUCHI (1932) with a vertical discontinuity, C: the Moho discontinuity model with a step, D: the 凹 -type Moho discontinuity model with six steps. The thickness of the surface layer is denoted by H. The S-wave velocity (β) and density (ρ) for layers L_1, L_2, L_3 and L_4 are given in units of km/s and g/cm^3, respectively. Numerals on the ground surface represent station site numbers.

Equation (1.1), obtained by HIGUCHI (1932), is a solution for perfect reflections and transmissions of a fundamental mode to a fundamental mode.

At the bottom of Fig. 1 values of shear wave velocities and densities, designated by (β,ρ), are given in units of km/s and g/cm^3, respectively. The values for layers L_1 and L_2 correspond respectively to the continental crustal and mantle elastic constants, but those for layers L_3 and L_4 arbitrary ones (BOORE, 1970). On the free surface in each model the site numbers are indicated at intervals of 100 km, and the waves propagate from smaller to larger site numbers. For Model C, the case in which the waves propagate inversely is also investigated.

1.3 Computation Using the Finite Difference Method

1.3.1 Equations of Wave Motion

The basic equation for the propagation of Love waves in a two-dimensional x–z coordinate (BOORE, 1970; SATO, 1978) is given by

$$\nabla^2 v_i = \frac{\partial^2 v_i}{\partial x^2} + \frac{\partial^2 v_i}{\partial z^2} = \frac{1}{\beta_i^2}\frac{\partial^2 v_i}{\partial t^2} \tag{1.2}$$

where v_i is the displacement in the y direction, i the kind of media, and β_i the shear wave velocities. We apply the centered finite difference formula to the above equation. With the abbreviation of i we obtain from the last term of Eq. (1.2)

$$v_{m,n,p+1} = 2v_{m,n,p} = v_{m,n,p-1} + \beta^2(\Delta t)^2 \nabla^2 v \tag{1.3}$$

where

$$\nabla^2 v = (v_{m+1,n,p} - 2v_{m,n,p} + v_{m-1,n,p})/\Delta x^2 + (v_{m,n+1,p} - 2v_{m,n,p} + v_{m,n-1,p})/\Delta z^2 \tag{1.4}$$

where Δx, Δz are the grid space in the x, z directions and Δt the time increment. v is a function of x, z and t, respectively denoted as subscripts of m, n and p.

1.3.2 Boundary Conditions

The boundary condition on the free surface is given by

$$\mu(\partial v/\partial z) = 0 . \tag{1.5}$$

At the boundary between the two media i and j, stress and displacement are continuous:

$$\mu_i(\partial v_i/\partial n) = \mu_j(\partial v_j/\partial n) \tag{1.6}$$

$$v_i = v_j \tag{1.7}$$

where $\partial/\partial n$ corresponds to a partial derivative normal to the interface.

By approximating the spatial derivative with the finite difference, Eq. (1.5) is reduced to

$$\mu[v(m,n+1,p) - v(m,n-1,p)]/2\Delta z = 0 , \tag{1.8}$$

so that, the displacement at a fictitious layer $z=(n-1)\Delta z$ is obtained from the following 'mirror image' condition

$$v(m,n-1,p) = v(m,n+1,p) . \tag{1.9}$$

If the discontinuity between the media i and j is parallel to the x-axis and on the line $z=n\Delta z$, Eq. (1.6) is approximated as

$$\begin{aligned}\mu_i[v_i(m,n,p) - v_i(m,n-1,p)]/\Delta z \\ = \mu_j[v_j(m,n+1,p) - v_j(m,n,p)]/\Delta z .\end{aligned} \tag{1.10}$$

Similarly, if the discontinuity is parallel to the z-axis and on the line $x=m\Delta x$, Eq. (1.6) is reduced to

$$\mu_i[v_i(m,n,p) - v_i(m-1,n,p)]/\Delta x = \mu_j[v_j(m+1,n,p) - v_j(m,n,p)]/\Delta x , \tag{1.11}$$

while Eq. (1.7) can be written as

$$v_i(m,n,p)=v_j(m,n,p)\,. \tag{1.12}$$

For the horizontal discontinuity, the displacement at a grid point (m,n) on the discontinuity is given, using Eqs. (1.10) and (1.12), as

$$v_i(m,n,p)=v_j(m,n,p)=[\mu_i v_i(m,n-1,p)+\mu_j v_j(m,n+1,p)]/(\mu_i+\mu_j)\,. \tag{1.13}$$

Similarly, for the vertical discontinuity, using Eqs. (1.11) and (1.12), the displacement at a grid point (m,n) on the discontinuity is written as

$$v_i(m,n,p)=v_j(m,n,p)=[\mu_i v_i(m-1,n,p)+\mu_j v_j(m+1,n,p)]/(\mu_i+\mu_j)\,. \tag{1.14}$$

Taking into consideration the displacement $v_{m,n-1,p}$ at a fictitious layer in Eq. (1.9), the displacement on the free surface is calculated from the Laplacian of Eq. (1.4).

1.3.3 Conditions for a Line Source

Initial values are given by

$$\begin{aligned}(v)_{t=0}&=f(x,z)\\(\partial v/\partial t)_{t=0}&=g(x,z)\end{aligned} \tag{1.15}$$

where $f(x,z)$ and $g(x,z)$ are determined from the normal mode solutions for uniform wave guides (SAITO, 1967) and such functions are calculated by the procedure for calculating theoretical seismograms by YOSHIDA (1983). In the present work a strike-slip point source and a step function are assumed as the fault type of the seismic source and the temporal variations of relative slip, respectively. The waves computed correspond to the fundamental mode Love waves excited at the azimuth of 90°, as measured counterclockwise from the fault strike, with the shortest epicentral distance of 100 km (left edge of the crustal structures shown in Fig. 1), and with a travel time of 82.21 s (the time $t=0$ in Eq. (1.15)). These plane Love waves are assumed to be incident on the uniform wave guide and propagate towards the right.

1.3.4 Stability Conditions of Time-Space Coordinate

The computational space has a horizontal length (x-axis) of 1000 km and a vertical length (z-axis) of 500 km. The grid interval $\Delta x(=\Delta z)$ is 5 km in Model B. In other models, Δx and Δz are assumed to be 5.0 and 8.75 km, respectively. The time increment Δt is 0.5 s in Model B, while $\Delta t=0.7$ s is assumed in other models. These discrete parameters satisfy the stability condition given by

$$(\beta_{\max}\Delta t/\Delta h)^2<1/2 \tag{1.16}$$

Δh is the minimum spatial grid sampling between Δx and (BOORE, 1970), and $\beta_{\max}$ is the maximum shear wave velocity among the models. The absorbing boundary conditions at the edges of the computational grid have been previously implemented by means of various techniques (e.g., SMITH, 1974; CLAYTON and ENGQUIST, 1977, 1980; CHANG and MCMECHAN, 1989). However, some problems remain (HINO, 1988). In the present work, we prepared large enough grid space not to be affected by artificial reflections.

1.3.5 Accuracy of Computations

We examine the accuracy of computations in the study of transmission coefficients and phase velocities. The amplitude spectra shown in Fig. 2(a) indicate that the predominant period of the incident waves is about 30 s.

Using seismograms numerically obtained at sites 4, 5 and 6 in Model A, the averages of mean phase velocities between pairs of stations (4, 5), (5, 6) and (4, 6) determined by Fourier transformations (SATO, 1955) are shown in Fig. 2(b). The figure shows that, compared to the normal mode solutions of the characteristic equation, errors are within 0.7% in most of the period range. Consequently, the computed phase velocities are estimated with a high accuracy.

SATO (1961) analytically solved "Higuchi's Model" (Model B in Fig. 1) and gave the expression for transmission coefficient (A_T) for a plane Love wave incidence under the condition (1.1), which is written as

$$A_T=2\mu_1\xi_1A_0/(\mu_1\xi_1+\mu_2\xi_2)=2\mu_3\xi_3/(\mu_3\xi_1+\mu_4\xi_3) \tag{1.17}$$

$$\xi_1=\omega/c_1, \qquad \xi_3=\omega/c_3 \tag{1.18}$$

where c_1 and c_3 are the phase velocities in the layers (L_1, L_2) and (L_3, L_4), respectively.

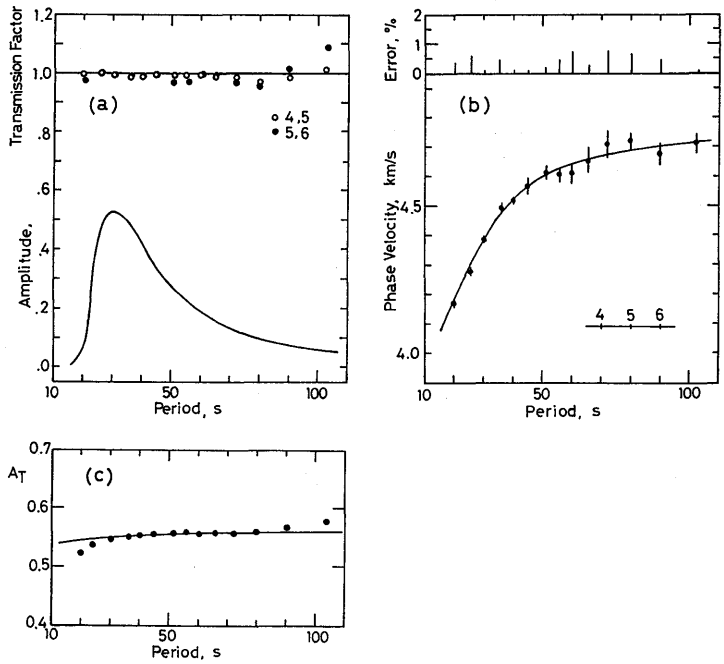

Fig. 2. (a) Amplitude spectra of the incident wave. (b) Average phase velocities (solid circles) and standard errors (vertical bars) for a station pair of (4, 5), (5, 6) and (4, 6) along with the theoretical phase velocity (a solid line), calculated for model A in Fig. 1. The absolute errors are shown in units of % at the top. (c) Transmission factors (solid circles) calculated from Eq. (1.19) and the transmission factor A (a solid line) obtained from Eq. (1.17) for model B in Fig. 1.

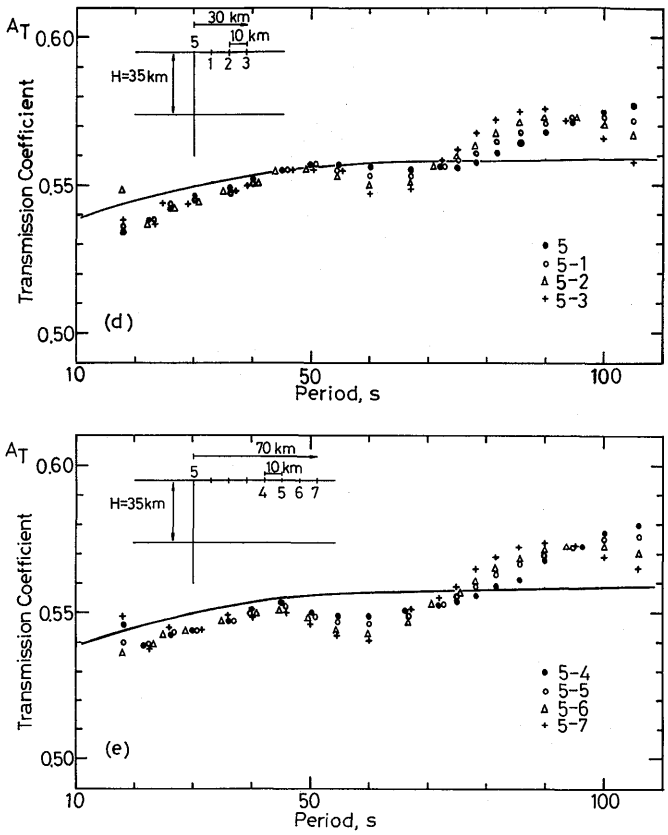

Fig. 2. (d), (e) Transmission coefficients near the vertical discontinuity.

A_0 is the amplitude of the incident waves and ω is the angular frequency. The transmission coefficient $T(\omega)$ obtained from the finite difference simulation is determined from the following equation.

$$T(\omega)=Q(\omega)/P(\omega) \tag{1.19}$$

$P(\omega)$ and $Q(\omega)$ are respectively the amplitude spectra of the seismograms at site 5 for the uniform wave guide (Model A in Fig. 1) and for "Higuchi's Model" (Model B in Fig. 1). Transmission coefficients determined by Eqs. (1.17) and (1.19) are shown in Fig. 2(c) by solid lines and solid circles, respectively. Although $T(\omega)$ has a tendency to be slightly smaller for short periods and slightly larger for long periods, both coefficients agree very well over wide range of periods. To examine the effects of the existence of a vertical discontinuity in the medium, $T(\omega)$ near the discontinuity were calculated in detail and are shown in Fig. 2(d), (e). The characteristics of $T(\omega)$ are very similar to Fig. 2(c), suggesting that the computation is stable.

1.3.6 Snap Shots of Waveforms

In Fig. 3, the distributions of free-surface displacement (snap shots) calculated at various times are shown for the models in Fig. 1. The snap shots (B) correspond to

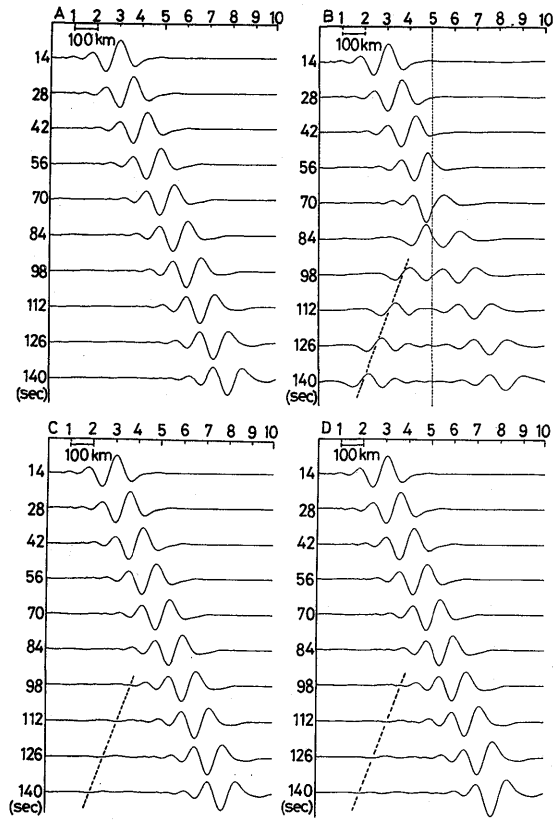

Fig. 3. The surface displacements at different instants of time for models A, B, C and D (denoted at the upper left part of the figure) in Fig. 1. The vertical interface is given by the dashed line below site 5 in model B. The reflected waves appear near the dotted oblique lines in the models B, C and D.

those for "Higuchi's Model," in which a vertical dotted line is marked at site 5 located at a vertical boundary. After a time-lapse of about 98 s, the reflected waves with the amplitudes comparable to those of transmitted waves propagate leftwards. These features agree well with the numerical results of BOORE (1970). We also see from the figure that the reflected waves, of course, do not appear in the snap shots (A) corresponding to Model A, while they appear slightly in snap shots (C) and (D), corresponding to Models C and D, respectively (obliquely dashed lines indicate the reflected waves).

The seismograms at sites from 1 to 10 are shown in Fig. 4 for Models A, B, and C given in Fig. 1. The reflected waves are observed to propagate along the dotted lines. Transmission coefficients and phase velocities shown in Fig. 2 are obtained by analyzing the waveforms given in Fig. 4. The seismograms for Model C are analyzed in the next section. The seismograms for Model D are shown in later sections in detail with shorter site intervals.

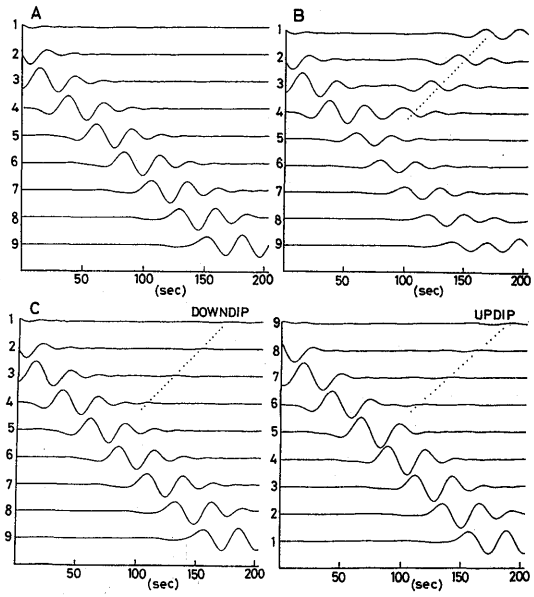

Fig. 4. Computed seismograms of Love waves for various sites along the surface for models A, B and C (denoted at upper left part of the figure) in Fig. 1. The reflected waves appear to propagate along the dotted lines. The time of the origin of the seismograms corresponds to $t=0$ in the Eq. (1.15).

1.4 Irregular Crustal Structure with a Dip Angle of 90°

If Love waves are incident on irregular boundaries, conversions between different Love wave modes and from Love waves to SH body waves are expected to occur (MAL and HERREA, 1965). It is known that the generation of converted waves depends on the impedence contrast at the irregular boundaries and the wave period (MALISCHEWSKY, 1976; NIAZY and KAZI, 1980). The behavior of converted waves is investigated in Part 3. In Sections 1.4 and 1.5, we consider dispersion characteristics of phase velocities (apparent phase velocities) of Love waves contaminated by the converted waves.

Plane Love waves are incident in Model C (Fig. 1) from the left or right side. Following BOORE (1970), we define propagation from the thinner to thicker parts of the layer as downdip propagation and the reverse case as updip propagation. In this section, we study the transmission coefficients and the dependence of velocities on propagation direction, just above the step of the discontinuity. These problems have not been investigated until now for a continental structure with a vertical discontinuity.

Spectra of incident waves, transmission coefficients and phase velocity dispersion curves for the two propagation modes are shown in Fig. 5. Figure 5(b) shows the amplitude spectra for updip and downdip propagations. The transmission coefficients (Fig. 5(a)) are determined from (1.19) at site 5 in Model C (Fig. 1). The phase velocity $c(\omega)$ is determined using the following formula (SATO, 1958; DZIEWONSKI

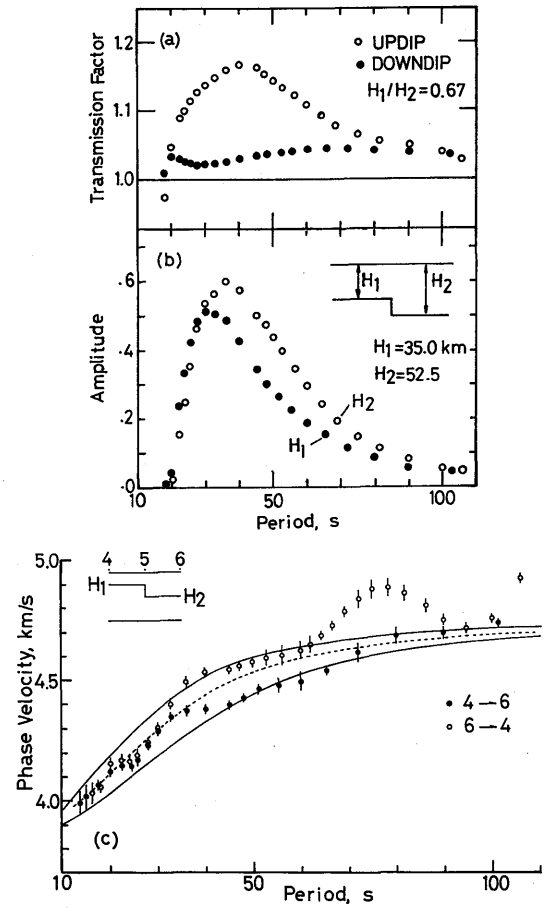

Fig. 5. (a) Transmission factors for updip (open circles) and downdip (solid circles) propagations calculated for model C in Fig. 1. (b) Amplitude spectra of incident plane Love waves for downdip and updip propagations. The thicknesses of surface layers H_1 and H_2 are assumed to be 35.0 and 52.5 km, respectively. (c) Phase velocities for downdip (solid circles) and updip (open circles) propagations over the region between sites 4 and 6. Phase velocity errors are shown by vertical bars. Phase velocities calculated for the three-layer model approximating the region between sites 4 and 6 are denoted by dotted lines. In the three-layer model, the elastic parameters at depths from H_1 to H_2 consist of synthetic density and rigidity, in which each has the average value between the crust and the mantle (see text for details). Two solid lines designate the phase velocities calculated for the uniform wave guide models with a crustal thickness of H_1 or H_2.

and HALES, 1972; BÅTH, 1974).

$$c(\omega)=\omega(r_2-r_1)/\{\omega(t_{02}-t_{01})+[\phi_{02}(\omega)-\phi_{01}(\omega)]+2m\pi\} \qquad (1.19)'$$

where ω and m are the angular frequency and integer, respectively. ϕ_{01} and ϕ_{02} are phase spectra of Love waves at epicentral distances r_1 and r_2 along the great circle path, start times of the wave trains being t_{01} and t_{02}, respectively. In this formula, we

can determine the phase velocity without knowledge of the initial phases of surface waves (YOSHIDA, 1982) and instrumental phase characteristics. Using this method, the phase velocities (Fig. 5(c)) are obtained by a Fourier transformation analysis of seismograms at sites 4 and 6, 100 km respectively in the left and right directions from site 5, just above the vertical discontinuity. The standard errors are calculated on the basis of error estimations shown in Fig. 2(b) and given by vertical bars.

Two solid lines in Fig. 5(c) show the phase velocities of upper and lower limits (the solutions for the uniform wave guides with crustal thicknesses of H_1 and H_2, respectively, for Model C. Dotted lines are phase velocities calculated for a new horizontally layered structure that consists of three layers: the first layer is the crust with thickness H_1, the second layer has, at depths from H_1 to H_2, synthetic layer parameters in which density and rigidity take mean values between crust and mantle, the third layer is the mantle below the depth of H_2. Phase velocities shown by dotted lines indicate approximately mean values of upper and lower limits.

We see from Fig. 5 that for downdip propagation the transmission coefficients are about 1.03 in the whole period range and are slightly smaller at a period of 30 s (corresponding to the predominant period of the incident waves), and that the phase velocities become slower at periods of 40–70 s, approaching the lower limits of phase velocities calculated for Model C. The dispersion curve is comparatively stable.

On the contrary, for the updip propagation the transmission coefficients have their maximum value (about 1.18) near a period of 40 s, decreasing abruptly to 1.0 towards short (20 s) and long (100 s) periods, and the phase velocities show such a remarkable variation that they exceed the upper limits by about 0.2 km/s at periods of 70–80 s. This variation is presumed for the characteristics of phase component to be distorted more strongly in the updip propagation than in the downdip propagation, due to the existence of a step in the Moho discontinuity.

The reason why phase and amplitude components are strongly distorted for updip propagation has not been investigated; however, as will be investigated in Part 4, it is known that the effects of SH waves converted from Love waves are strong at long periods for updip propagation. The dependence of phase velocities on propagation direction described above generally agrees with the phase velocity anisotropy appearing in the sloping layer of the ocean-continent boundary (BOORE, 1970).

It is a notable feature that phase velocities at periods less than 30 s, for both the downdip and updip propagations, are approximately equal to average phase velocities between upper and lower limits (dotted lines in Fig. 5(c)). The wavelength of Love waves at a period of 30 s is about 130 km (phase velocity: 4.3 km/s) and the shallowest depth of the Moho discontinuity ($H_1=35$ km) corresponds to about 27% of this wavelength. These computation results suggest that the phase velocities of waves with a wavelength (λ) shorter than $\lambda < H_1/0.27$ do not suffer strongly from the effects of laterally heterogeneous structures. The characteristics of phase velocities for different parameters of H_1 and H_2 are investigated in Part 2.

It can be concluded from this subsection that the characteristics of phase velocity anisotropy for the media with a vertical discontinuity are very similar to those for the

media with a sloping layer.

1.5 Irregular Crustal Structures with a Slope Angle of about 20°–30°

Media with transitional layers have been studied by several authors. Most of them studied the ocean-continent boundaries with sloping layers having a dip angle of 45° (LYSMER and DRAKE, 1971; DRAKE and BOLT, 1980; BOLT and DRAKE, 1986). AKI and LARNER (1970) treated the problems of SH waves across a concave crustal structure and obtained simply variations of amplitude and phase delays over the interface. LEVANDER (1985) investigated Rayleigh wave propagation in the continental concave crustal structure with a slope angle of 21° and obtained phase velocities over the interface. However, he did not extend the study to the problems of scattering and inversion of Rayleigh waves. In this section, we investigate the dispersive property of Love waves across the concave crustal structure and cultivate a better understanding of the problems related to Love wave inversion.

1.5.1 Model of the Moho Discontinuity with a Slope Angle of about 20°–30°

In Model D of Fig. 1, the Moho discontinuity is concave and consists of a combination of a set of steps of the Moho discontinuity. As the height of step is 17.5 km and the wavelengths of the incident waves are 100–250 km, the wavelengths are sufficiently large compared to the height of the step. Hence, it can be said that Model D is an approximation of the sloping Moho discontinuity with an angle of about 20° (Fig. 6(a)). To observe in detail the property of the dispersion of the waveforms, the new site numbers are designated as shown in Fig. 6(a).

Site numbers 4, 5, 6, 7 and 8 in Fig. 1 correspond to those of 1, 5, 9, 13 and 17 in Fig. 6(a), respectively. In Fig. 6(b) the waveforms at sites 1–17 are shown (numerals to the right of the figure correspond to the site numbers given in Model D of Fig. 1). From the figure we see that (1) the front of the incident waves consists of trough (t1), peak (p1), trough (t2) and peak (p2), and (2) the first trough (t1) gradually increases long period components and the second peak (p2) increases its amplitude. From the variations of these waveforms, we can see that Love waves exhibit normal dispersion.

1.5.2 Phase Velocity Anisotropy

Phase velocities calculated for three pairs of stations (5, 10), (10, 15) and (5, 15) inside the irregular structure are shown in Fig. 6(c). The standard errors are given by vertical bars. For the downdip propagation (5, 10), phase velocities near periods of 19 and 23 s are close to the upper limits of (normal mode solutions for the uniform wave guide with a crustal thickness of 35 km), and phase velocities of 4.0 and 4.05 km/s at periods of 26 and 42 s, respectively, are close to the lower limits (normal mode solutions for the uniform wave guide with a crustal thickness of 87.5 km). At periods of 28–36 s, phase velocities of 4.2–4.3 km/s indicate approximately mean values between the upper and lower limits. Thus oscillations of phase velocities are remarkable in the period range 18–46 s.

On the contrary, for the updip propagation (10, 15) phase velocities at periods less than 19 s are slightly larger than the lower limit of 3.9 km/s, and a minimum value

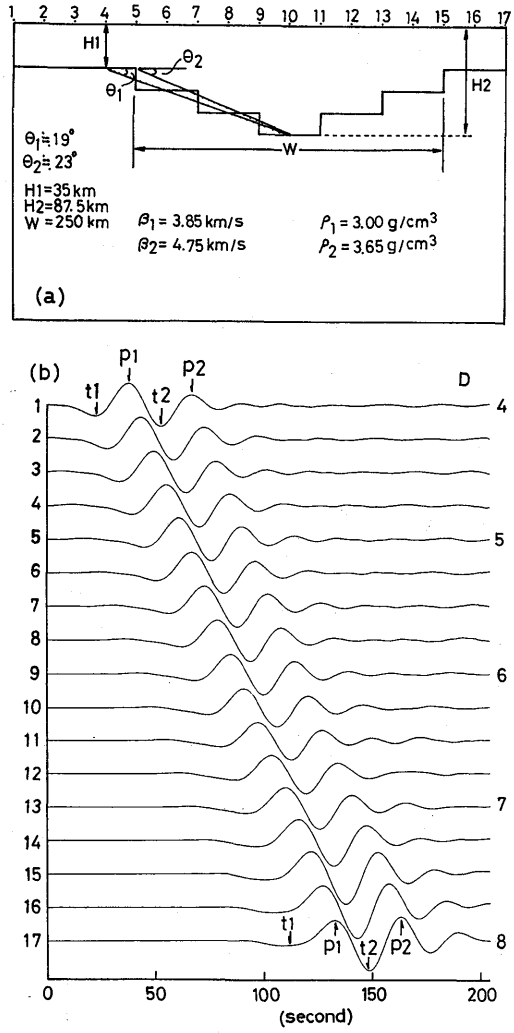

Fig. 6. (a) Schematic diagrams of model D in Fig. 1 near the nonuniform wave guide. The interval between station sites is 25 km. Subscripts 1 and 2 attached to the elastic parameters denote crust and mantle, respectively. (b) Computed seismograms of Love waves at various sites; the numerals along the ordinates correspond to the station site numbers in (a). The numerals to the right correspond to those in model D in Fig. 1. At the locations of the first trough (t1), peak (p1) and the second trough (t2), peak (p2) in the seismograms, the vertical arrows are indicated for sites 1 and 17.

of 3.8 km/s near at a period of 22 s is lower by about 0.15 km/s than the lower limits.

For periods greater than 22 s, phase velocities increase gradually up to a period of 46 s with increasing periods. Notable characteristics are that phase velocities are larger than the lower limits at periods longer than 35 s. Phase velocities near a period of 46 s are approaching the upper limit of 4.58 km/s, but they never exceed the upper limit.

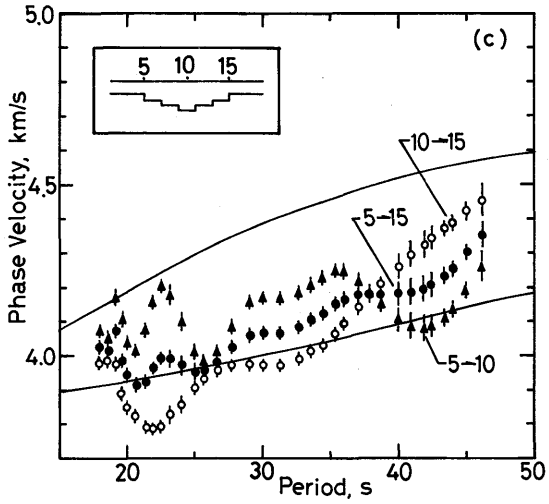

Fig. 6. (c) Phase velocities over the region of the nonuniform wave guide; downdip (solid triangles) and updip (open circles) propagations and the entire region (solid circles). Phase velocity errors are shown by vertical bars. Two solid curves denote theoretical phase velocities calculated for the uniform wave guides with a crustal thickness of 35 or 87.5 km, calculated using the normal mode theory.

Comparing phase velocities for downdip propagation with those for updip propagation, we can point out the following interesting characteristics:

(1) At several periods, the phase velocities for downdip and updip propagations are almost equal.

(2) At short periods, phase velocities for downdip propagation are larger than those for updip propagation.

(3) At long periods, the situation is reversed.

These characteristics could not be found in irregular structures with a dip angle of 90°, such as in Section 1.4, or a transitional zone between the ocean and the continent by BOORE (1970). The appearance of anisotropy is presumed to be caused by the scattering of Love waves generated at the boundary of the concave interface of the Moho discontinuity and the phase components of transmitted waves are distorted by scattering (TSUKUDA, 1972; MOMOI, 1981). Contribution of scattered waves to phase velocity anisotropy is investigated in detail in Parts 2 and 3.

1.5.3 Smoothly Varying Moho Discontinuity

To examine the effects of the irregularity of the sloping layer boundaries on the phase velocity dispersion, this subsection investigates a concave structure (Model E) whose sloping layer boundaries vary smoothly. In Model E, the six steps forming the slope of the concave structure in Model D are replaced by oblique lines with a dip angle of 30°. Phase velocities determined for this model for downdip and updip propagations are shown in Fig. 6(d).

The figure shows that the general characteristics of the phase velocity dispersion featured in Model D (Fig. 6(c)) are found again. The phase velocities for downdip

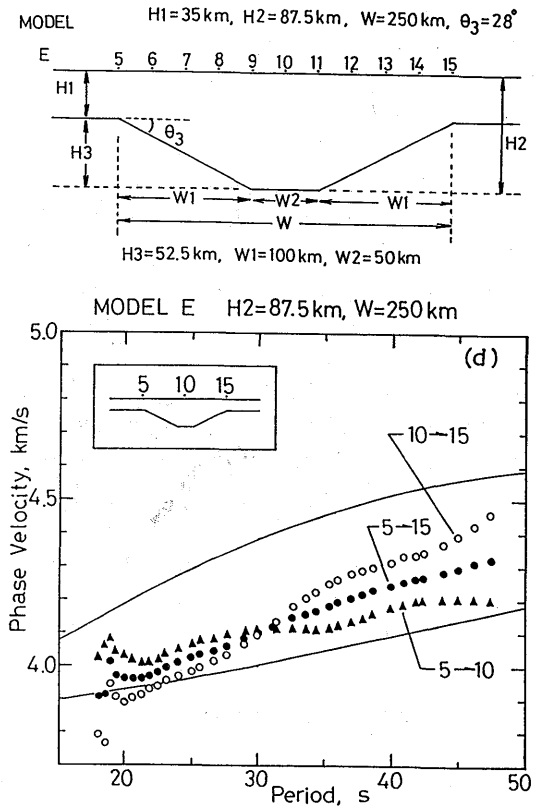

Fig. 6. (d) Top: Schematic diagram of the Model E. In this model, several steps consisting the slopes of the concave structure in Model D are replaced by oblique lines whose dip angles are 28°. The elastic parameters in the media are assumed to be the same as those indicated in Model D. Bottom: Phase velocities over the interface. Legend as for (c).

propagation are high at short periods compared to those for updip propagation, while the situation is reversed at long periods. However, the oscillations of phase velocities in Model D are not observed in Model E. The phase velocity dispersion curve for Model E can be obtained by smoothing that for Model D. The above results suggest that the phase velocity dispersion is stable if the slope of the layer boundaries varies smoothly. The relationship between phase velocity dispersion and phase spectral characteristics of Love waves over the interface is discussed in later sections.

1.5.4 Mean Phase Velocities for Irregular Crustal Structures

Mean phase velocities between sites (5, 15) indicate middle values between the downdip and updip propagations and do not take account of the average of the upper and lower limits (Figs. 6(c), (d)). The mean phase velocities approach the lower limits at short periods while they approach the upper limits at long periods.

These characteristics might be explained by the relationship between phase velocity and medium in that the phase velocities at short periods are more strongly influenced by the shallower medium while those at long periods are more strongly

influenced by the deeper medium. Namely, the effects of lateral heterogeneity on phase velocities decrease with an increasing period.

1.5.5 Approximation of Irregular Crustal Structures Using a Horizontally Layered Structure

We now consider the inversion of Love waves across a mountain root structure. In the inversion of observed surface wave data, irregular structures are frequently approximated by a horizontally layered structure. Therefore, we compare the mean phase velocities for the region of the concave interface (5, 15) (Fig. 7(a)) with phase velocities calculated from two models (a) and (b). These two models are approximated by horizontally layered structures for the region mentioned above and are inserted at the upper left part of Fig. 7(a).

At this point, let us introduce the "weighting coefficient," which is used for making synthetic layer parameters for horizontally layered structures and is defined as "the ratio of the horizontal length of the layer possessing an arbitrary medium to the whole horizontal length of the laterally heterogeneous layer" (see also Fig. 7(e)).

The region between sites 3 and 17, which are 50 km from the left or right edge of the concave interface, partly include the vertical boundaries of the Moho discontinuity inside each layer. Using the weighting coefficients, the region is approximated by a horizontally layered structure (Model (a)) which includes, to a small extent,

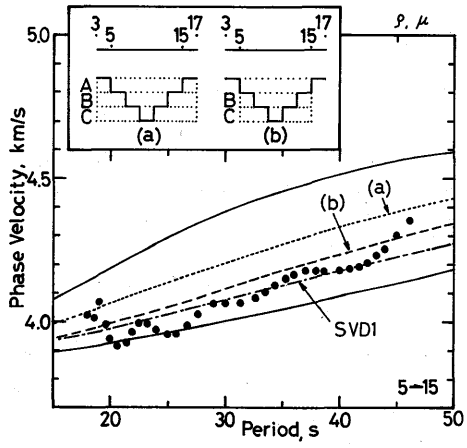

Fig. 7. (a) Average phase velocities (solid circles) over the region between sites 5 and 15. The phase velocities for models (a) and (b) at the upper left are shown by dotted and dashed lines, respectively. Models (a) and (b) are approximations for the nonuniform wave guide, in which each layer of nonuniform layers A, B and C is replaced by one uniform layer constructed using synthetic layer parameters of density and rigidity (see text for details). The parameters are calculated through the Eqs. (1.20) and (1.21) in the text, using weighting coefficients defined as "the ratio of the horizontal length of a layer possessing an arbitrary medium to the horizontal length of the laterally heterogeneous layer." For the two solid curves, see the caption in Fig. 6(c). The phase velocities computed for model SVD1, which was determined using the singular value decomposition technique, are shown by a dash-dot line.

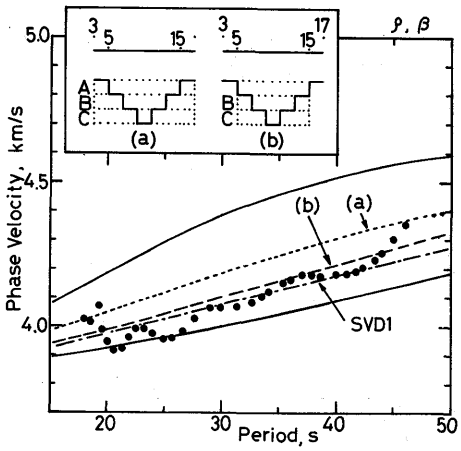

Fig. 7. (b) Models (a) and (b) are approximations for the nonuniform wave guide, in which each layer of nonuniform layers A, B and C is replaced by one uniform layer constructed using synthetic layer parameters of density and S-wave velocity. For SVD1 see the caption for (a). Note that the phase velocities for models (a) and (b), constructed using synthetic density and S-wave velocity, are closer to the mean phase velocities (solid circles) than those for the respective models (a) and (b), constructed using synthetic density and rigidity.

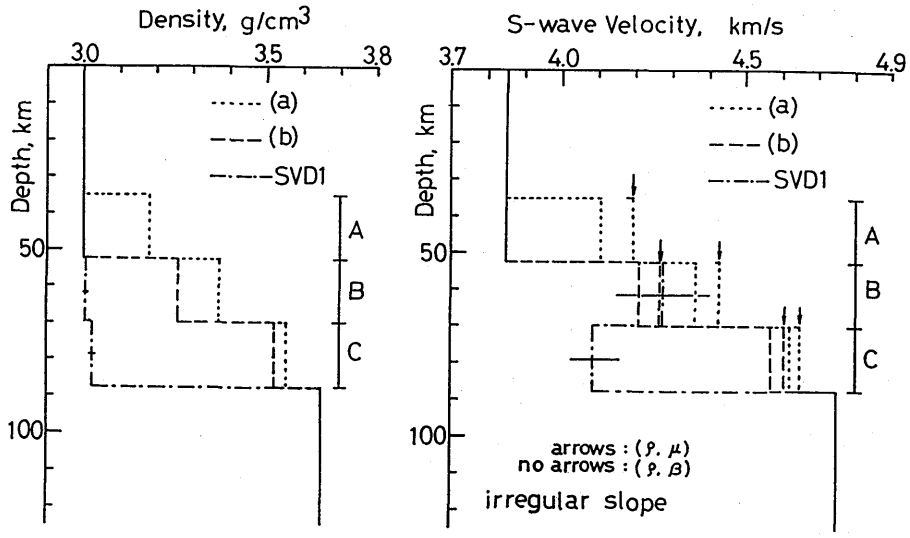

Fig. 7. (c) The density and S-wave velocity structures for models (a), (b) and SVD1. For the S-wave velocities determined using synthetic density and rigidity, the vertical arrows are given in both models (a) and (b). The standard errors are indicated by horizontal bars for densities and S-wave velocities of model SVD1. The depth ranges for each layer A, B and C in models (a) and (b) are indicated in the right.

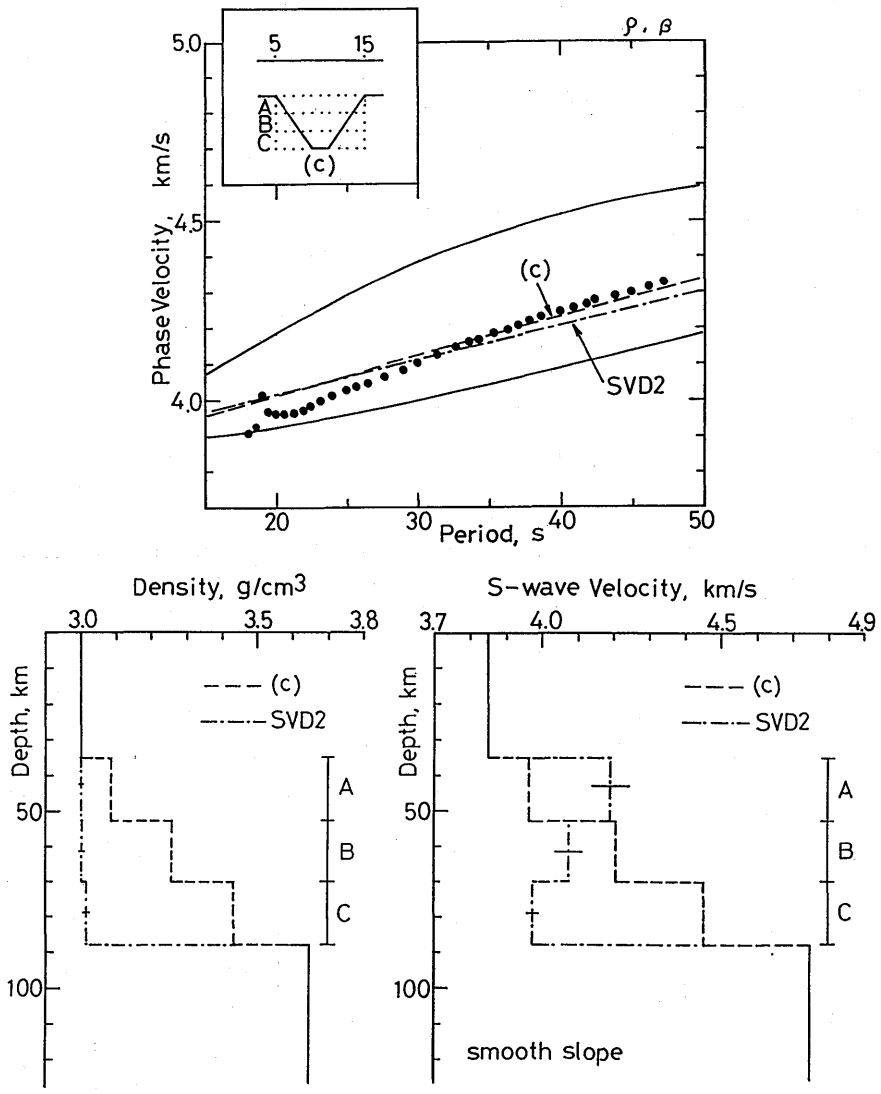

Fig. 7. (d) Top: Average phase velocities (solid circles) over the region between the sites (5, 15) for Model E (Fig. 6(d)). The phase velocities for model (c) at upper left are shown by a dashed line. Model (c) is an approximation for the nonuniform wave guide, in which each layer of the nonuniform wave guides A, B and C is replaced by one uniform layer constructed using synthetic layer parameters of density and S-wave velocity. The parameters are calculated through Eq. (1.22) in the text, using the weighting coefficients (see text for details). The phase velocities for model SVD2, which were determined using the singular value decomposition method, are shown by a das–dot line. For the two solid curves, see the caption for Fig. 6(c). Bottom: The density and S-wave velocity structures for models (c) and SVD2. The standard errors are indicated by horizontal bars for the density and S-wave velocities for model SVD2. The depth ranges for each layer A, B and C in model (c) are indicated to the right.

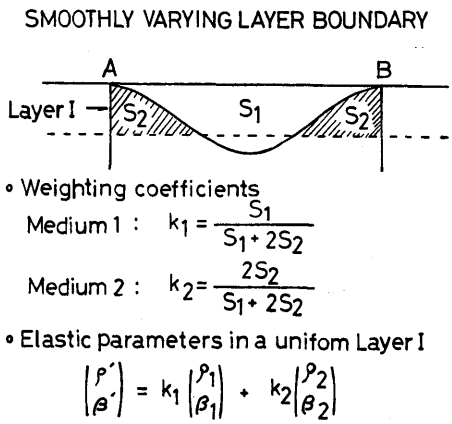

Fig. 7. (e) An example of an approximation of a smoothly varying layer boundary by a uniform layer. S_1 and S_2 within the irregular layer designated as Layer I between the region from A to B denote the area for media 1 and 2, respectively. Using the "weighting coefficient" defined as the ratio of the area of the layer possessing an arbitrary medium to the entire area of the laterally heterogeneous layer, the weighting coefficients k_1 and k_2 for the media 1 and 2 are determined from the expressions given at the middle of the figure. Synthetic layer parameters of density ρ' and S-wave velocity β', for approximating the irregular structure with a smoothly varying layer boundary by a uniform layer are obtained from the equation at the bottom. Subscripts 1 and 2 attached to density and S-wave velocity correspond to the nature of the medium.

areas outside the concave interface, because the outside areas should be strongly affected by scattered waves. Model (a) includes horizontal layers A, B and C for the region. As written in Eq. (1.20), the layers A, B and C are constituted by new elastic parameters of density and rigidity which are synthesized using weighting coefficients (5/7, 2/7, $\cdots$, etc.).

The region between sites 5 and 15 partly include the vertical boundaries of the Moho discontinuity inside each layer. Model (b) is an approximation with a horizontally layered structure for the region merely within the concave interface. The horizontal layers B and C for the region, as written in Eq. (1.21), are constituted by new elastic parameters of density and rigidity synthesized using the weighting coefficients (3/5, 2/5, $\cdots$, etc.).

Namely, if we denote density of the crust and the mantle as ρ_1, ρ_2 and rigidity as μ_1, μ_2, in Model (a), synthesized density and rigidity are given by

$$\text{Layer A:} \quad \begin{pmatrix} \rho'_A \\ \mu'_A \end{pmatrix} = \frac{5}{7}\begin{pmatrix} \rho_1 \\ \mu_1 \end{pmatrix} + \frac{2}{7}\begin{pmatrix} \rho_2 \\ \mu_2 \end{pmatrix}$$

$$\text{Layer B:} \quad \begin{pmatrix} \rho'_B \\ \mu'_B \end{pmatrix} = \frac{3}{7}\begin{pmatrix} \rho_1 \\ \mu_1 \end{pmatrix} + \frac{4}{7}\begin{pmatrix} \rho_2 \\ \mu_2 \end{pmatrix} \qquad (1.20)$$

$$\text{Layer C:} \quad \begin{pmatrix} \rho'_C \\ \mu'_C \end{pmatrix} = \frac{1}{7}\begin{pmatrix} \rho_1 \\ \mu_1 \end{pmatrix} + \frac{6}{7}\begin{pmatrix} \rho_2 \\ \mu_2 \end{pmatrix}$$

and those in Model (b),

$$\text{Layer B:} \quad \begin{pmatrix}\rho'_B\\ \mu'_B\end{pmatrix} = \frac{3}{5}\begin{pmatrix}\rho_1\\ \mu_1\end{pmatrix} + \frac{2}{5}\begin{pmatrix}\rho_2\\ \mu_2\end{pmatrix}$$

$$\text{Layer C:} \quad \begin{pmatrix}\rho'_C\\ \mu'_C\end{pmatrix} = \frac{1}{5}\begin{pmatrix}\rho_1\\ \mu_1\end{pmatrix} + \frac{4}{5}\begin{pmatrix}\rho_2\\ \mu_2\end{pmatrix} \tag{1.21}$$

The upper and lower limits of phase velocities and mean phase velocities (solid circles) between two sites (5, 15), are shown in Fig. 7(a), and they are the same as those given in Fig. 6(d). The dotted (a) and broken (b) lines in Fig. 7(a) are phase velocities calculated for the horizontally layered structures of Models (a) and (b), which are shown in the upper left part of the figure.

From the figure we see that the mean phase velocities between two sites (5, 15) agree with those for Model (b) rather than for Model (a) in the period range 20–45 s. The phase velocities for Model (a) are higher by about 0.1 km/s than the mean phase velocities for the region of the concave interface in the period range described above. It is inferred that this discrepancy is caused by an overestimation of irregular layers for Model (a). Namely, the mantle is contributed too much for the regions (3–5) and (15–17) for the construction of a horizontally layered structure. On the contrary, the phase velocities for Model (b) are generally close to the mean values for the region of the concave interface (5, 15), although they differ a little at several periods.

Surface wave data are generally inverted using shear wave velocity and density. Therefore, using the same weighting coefficients given in Eqs. (1.20) and (1.21), we obtained uniform wave guides constituted by the two elastic parameters, and calculated phase velocities for the uniform wave guides (Fig. 7(b)). The phase velocities obtained for Models (a) and (b) in Fig. 7(b) are very close to those in Fig. 7(a). But we notice that the phase velocities calculated for Models (a) and (b) in Fig. 7(b) are closer to the observed mean phase velocities (solid circles) than those in Fig. 7(a). Between the two dispersion curves for Models (a) and (b) in Fig. 7(b), the later explains better the mean phase velocities.

The singular value decomposition technique (JACKSON, 1972; WIGGINS, 1972; MATSU'URA and HIRATA, 1982; SAITO, 1983; YOSHIDA, 1986, 1990a, b; YOSHIDA and KAWASAKI, 1991) is frequently used for the inversion of surface waves. In Figs. 7(a) and (b), the phase velocities calculated for structure models obtained using the technique, designated as SVD1, are also shown together with those for Models (a) and (b). The phase velocities for Model (b) in Fig. 7(b) are slightly higher than, but very close to those for SVD1 in a whole period range.

The above results suggest that, even in such cases that the scattered waves are generated by irregular structures, phase velocities obtained on the free surface over the irregular structures can be interpreted from horizontal layers approximated using synthesized elastic parameters.

The structures of shear wave velocities and densities of Models (a) and (b), obtained using the weighting coefficients and the singular value decomposition, are

shown in Fig. 7(c). The figure shows that the shear wave velocities obtained using weighted density and rigidity parameters are higher than those obtained using weighted density and shear wave velocity parameters. This result is consistent with the dispersion characteristics in that the phase velocities for Models (a) and (b) in Fig. 7(a) are higher than those for Models (a) and (b) in Fig. 7(b), respectively.

From our observations the structures of shear wave velocity and density in Fig. 7(c) are more realistically depicted by Model (b), because shear wave velocity and density increase with increasing depth, while shear wave velocities for Model SVD1 decrease with increasing depth. It should be noted here that inversion using the singular value decomposition is performed with a priori knowledge of the maximum depth of the concave structure.

The numerical experiments of the above inversion of Love waves suggest that crustal or mantle structures obtained by Love wave data have some problems.

In the case that the slope of the layer boundaries of irregular structures varies smoothly, we take the weighting coefficients defined as "the ratio of the area of the layer possessing an arbitrary medium to the whole area of the laterally heterogeneous layer" (see Fig. 7(e)).

Here, we investigate the relationship between the horizontal layers obtained using the weighting coefficients and the mean phase velocities over the irregular structure represented by Model E (Fig. 6(d)). The mean phase velocities are shown in Fig. 7 (d). Adopting the weighting coefficients defined above for Model E (designated as Model (c) in Fig. 7(d)), the synthesized density and the shear wave velocity in Model (c) are given by

$$\begin{aligned}
&\text{Layer A:} && \begin{pmatrix}\rho'_A\\ \beta'_A\end{pmatrix}=0.867\begin{pmatrix}\rho_1\\ \beta_1\end{pmatrix}+0.133\begin{pmatrix}\rho_2\\ \beta_2\end{pmatrix}\\
&\text{Layer B:} && \begin{pmatrix}\rho'_B\\ \beta'_B\end{pmatrix}=0.600\begin{pmatrix}\rho_1\\ \beta_1\end{pmatrix}+0.400\begin{pmatrix}\rho_2\\ \beta_2\end{pmatrix} \qquad (1.22)\\
&\text{Layer C:} && \begin{pmatrix}\rho'_C\\ \beta'_C\end{pmatrix}=0.333\begin{pmatrix}\rho_1\\ \beta_1\end{pmatrix}+0.667\begin{pmatrix}\rho_2\\ \beta_2\end{pmatrix}
\end{aligned}$$

The upper and lower limits of the phase velocities (solid lines) and the mean phase velocities (solid circles) between the two sites (5, 15) for Model (c) are shown in Fig. 7(d), together with the phase velocity dispersion curves calculated for Model (c) and Model SVD2, which was obtained from the inversions, using the method of singular value decomposition.

The difference in the phase velocity dispersion curves between Models (c) and SVD2 is very small. But we notice from Fig. 7(d) that Model (c) is superior to Model SVD2, because density and shear wave velocity increase with depth, while the shear wave velocity for Model SVD2 decreases with depth, as found in the previous numerical experiment (Fig. 7(c)).

These results lead to the conclusion that the phase velocities of Love waves across irregular structures can be explained well in terms of synthesized elastic parameters using the weighting coefficients.

In Fig. 7(e), for the irregular structure with a smoothly varying layer boundary, the weighting coefficients of k_1 and k_2 and the synthetic density ρ' and rigidity μ' are shown in a general form. S_1 and S_2 within the irregular layer designated as Layer I, between locations A and B, denote the areas for media 1 and 2, respectively.

If we approximate Layer I with a uniform layer, following the definition of the weighting coefficients described above, the weighting coefficients k_1 and k_2 for media 1 and 2 are determined as

$$\begin{aligned} k_1 &= S_1/(S_1+2S_2) \\ k_2 &= 2S_2/(S_1+2S_2) \end{aligned} \tag{1.23}$$

It is obvious that the denominator of (S_1+2S_2) is the whole area of the laterally heterogeneous Layer I. Using these weighting coefficients, synthetic layer parameters for a uniform layer for Layer I are obtained from

$$\begin{pmatrix} \rho' \\ \beta' \end{pmatrix} = k_1 \begin{pmatrix} \rho_1 \\ \beta_1 \end{pmatrix} + k_2 \begin{pmatrix} \rho_2 \\ \beta_2 \end{pmatrix} \tag{1.24}$$

where suffixes attached to density and shear wave velocity indicate the medium.

It should be noted here that the weighting coefficients used in Eqs. (1.20) and (1.21) are equivalent to those in Eq. (1.23). The reason is that the concept of "horizontal length" used for the determination of weighting coefficients in Eqs. (1.20) and (1.21) can be replaced by the "area," because the vertical widths in layers A, B and C shown in Fig. 7(a) are constant.

1.6 Consideration of Phase Velocities

Models C and D in Fig. 1 may correspond to the tectonic steps of the Himalaya and the Tibetan plateau with a crust thickness of 55–85 km (CHEN and MOLNAR, 1981). In continental regions with a thick crust as mentioned above, phase velocities over the interface should exhibit the velocity characteristics obtained in the previous sections, if the irregular boundaries are similar to those for Models C, D and E.

The computational results obtained in this chapter suggest that phase velocity greatly depends on the propagating direction of the waves in the sloping layers. Therefore, in the cases of shallow underground basin structures (e.g., KOKETSU *et al.*, 1991; YOSHIDA, 1992) or soft sedimentary layers (HIGASHI and KUDO, 1992), phase velocity anomalies similar to those obtained in the previous section can be detected at periods shorter than 20 s, if the slope angle is greater than 20°.

1.7 Concluding Remarks of Part 1

Characteristics of the propagation of Love waves in irregular structures corresponding to continental underground structures, such as the continent–continent boundaries and the great mountain ranges, have been investigated using the finite difference method, and important and interesting results are obtained:

For a simple model with a step (width: 17.5 km) of the Moho discontinuity, as shown in Model C in Fig. 1,

(1) For the updip propagation oscillations of phase velocities occur at periods longer than 70 s.

(2) For the downdip propagation phase velocities do not show a distinct jump.

(3) Phase velocities for updip propagation are larger than those for downdip propagation in the period range 30–100 s, and show apparent anisotropy.

For mountain root structures with a slope angle of 20°–30° for the Moho discontinuity, as shown in Models D (Fig. 1) and E (Fig. 6(d)) (the horizontal distance is 250 km and the maximum widt of the Moho discntinuity is 52.5 km at the center; the structure is symmetrical; the slope of the Moho discontinuity consists of several steps and oblique lines in Models D and E, respectively).

(4) For both Models D and E, phase velocities for downdip and updip propagations along a horizontal distance of 125 km show an apparent anisotropy. For Model D, in the period range 18–37 s, phase velocities for downdip propagation are higher than those for updip propagation. In the period range 38–46 s, they are reversed. For Model E, at periods shorter than 30 s, phase velocities for downdip propagation are higher than those for updip propagation. At periods longer than 30 s, they are reversed.

(5) For Model D, downdip propagation phase velocities show several oscillations in the period range 18–46 s, while updip propagation phase velocities increase monotonously in the period range 22–46 s.

(6) For Model E, the phase velocities for both downdip and updip propagations are stable compared to those for Model D.

(7) Mean phase velocities for the region of the concave interface take middle values between downdip and updip propagations.

(8) However, the mean phase velocities do not take middle values between upper and lower limits, which correspond to phase velocities for the thinnest (S-structure) and thickest (D-structure) crustal structures, respectively. The mean phase velocities can be explained with a dispersion curve calculated for a horizontally layered structure which is constructed using the "weighting coefficient."

(9) The "weighting coefficient," which is defined as the ratio of the horizontal area of the layer possessing an arbitrary medium to the entire horizontal area of the laterally heterogeneous layer," is introduced to construct a horizontally layered structure for approximating arbitrary irregular layers.

(10) The mean phase velocity dispersion curve for the concave interface approaches the dispersion curve for D-structure at short periods, and approaches that for S-structure at long periods.

(11) The structures of shear wave velocity and density obtained using the weighting coefficients are more realistic than those obtained using the singular value decomposition technique for the inversion of Love waves.

Part 2

Peculiarity of Phase and Amplitude of Lowe Waves across Irregular Structures of the Moho Discontinuity

2.1 Introduction

It has been found in the finite difference simulations discussed in Part 1 that Love waves across a symmetrical mountain root structure, which forms a great mountain range with a crustal thickness of 35–87.5 km and a heteogeneous Moho discontinuity of a slope angle of 20–30°, show phase velocity dispersions greatly dependent on propagation direction. The anisotropy was also found in the laterally heterogeneous structure (BOORE, 1970; LEVANDER, 1985). The characteristics, however, differ somewhat.

The origin of anisotropy in the sloping layer and the concave structure could be caused by effects of scattering of Love waves. MAL and HERRA (1965) studied the scattering of Love waves in a crust with vertical discontinuities. They found a greater phase shift in the fundamental mode for a larger inhomogeneous area. MALISCHEWSKI (1976) studied the relationship between incident angle and reflection and transmission coefficients of surface waves including mode conversion. NIAZY and KAZI (1980) studied the scattering problems of Love waves for welded layered quarter-spaces and found that when a wave is travelling from a hard to a soft medium, the transmission coefficients for low frequencies are larger than those for high frequencies. There have been many investigations of problems concerning scattering and diffraction of P, SV and Rayleigh waves (WONG, 1982; FUJII *et al.*, 1984; DRAVINSKI and MOSSESSIAN, 1987; KAWASE, 1988; SANCHEZ-SESMA and CAMPILLO, 1991) or SH waves (SANCHEZ-SESMA, 1990) by topographic features in an elastic half-space. In these studies, however, the relationships between the characteristics of phase velocity dispersion and phase or amplitude anomaly over irregularly layered structures have not been investigated.

In Part 1, the study focuses on the characteristics of phase velocity dispersion over media with step and concave structures. To make clear the characteristics of anisotropy, we have to minutely investigate spatio-temporal variations of phase spectra. Therefore, in this chapter, the phase spectra of Love waves across the mountain root structures represented by Models D and E (Figs. 6(a) and (d)) are investigated not only on the free surface but also within elastic media through a set of tomographic snap shots at various instants in time. The characteristics of phase velocity and amplitude spectra for various simple models are also investigated.

2.2 Analysis of Phase Velocity and Phase Spectral Characteristics

We examine in detail the relationships between phase velocities and phase spectra of Love waves obtained for the mountain root structures. Fig. 8(a) shows the difference between phase spectra obtained for the nonuniform wave guide of Model D and for the uniform wave guide of Model A. The phase spectral differences are caused

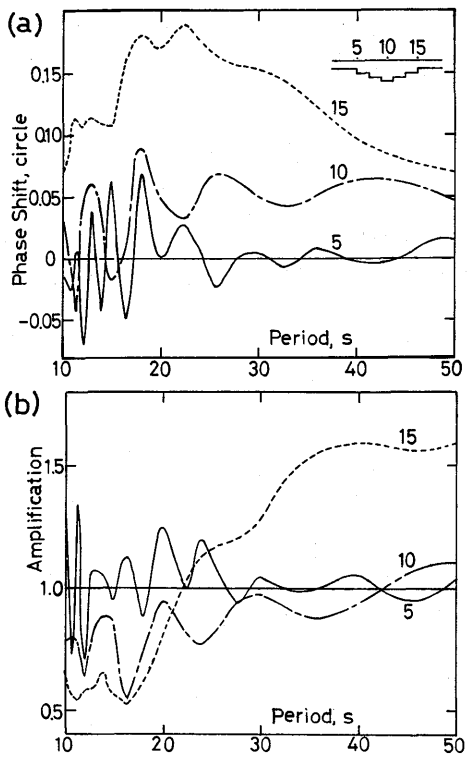

Fig. 8. Perturbations of phase (a) and amplitude (b) spectra of the displacement component of Love waves at sites 5, 10 and 15 for Model D, obtained by a Fourier transformation. The phase shift in (a) denotes the phase spectral difference between the spectra of the waves for the nonuniform wave guide and those for the uniform wave guide (Model A) in units of a circle (1 circle$=2\pi$ radian). The amplification in (b) shows the ratio of the amplitude spectra of the waves for the nonuniform wave guide to those for the uniform wave guide.

only by irregular layer boundaries and we define the difference in the spectra at sites 5, 10 and 15 as $\delta\phi_5^{H_e}$, $\delta\phi_{10}^{H_e}$ and $\delta\phi_{15}^{H_e}$, respectively. On the other hand, we define phase spectra of Love waves obtained for Model A as $\phi_5^{H_0}$, $\phi_{10}^{H_0}$, and $\phi_{15}^{H_0}$, at the sites mentioned above, respectively. Then, the phase spectra at the respective sites are written as follows.

$$\begin{aligned}\phi_5&=\phi_5^{H_0}+\delta\phi_5^{H_e}\\ \phi_{10}&=\phi_{10}^{H_0}+\delta\phi_{10}^{H_e}\\ \phi_{15}&=\phi_{15}^{H_0}+\delta\phi_{15}^{H_e}\end{aligned}\qquad(2.1)$$

Substituting Eq. (2.1) into $\phi_{01}(\omega)$ and $\phi_{02}(\omega)$ in Eq. (1.19), phase velocities are determined from the equation;

$$c(\omega)=\omega(r_{10}-r_5)/\{(\phi_{10}^{H_0}-\phi_5^{H_0})+(\delta\phi_{10}^{H_e}-\delta\phi_5^{H_e})+2m\pi\}\qquad(2.2)$$

for downdip propagation, and

$$c(\omega)=\omega(r_{15}-r_{10})/\{(\phi_{15}^{H_0}-\phi_{10}^{H_0})+(\delta\phi_{15}^{H_e}-\delta\phi_{10}^{H_e})+2m\pi\} \tag{2.3}$$

for updip propagation. For the wave propagation in the uniform wave guide, the relation

$$\begin{aligned}\phi_{15}^{H_0}-\phi_{10}^{H_0}&=\phi_{10}^{H_0}-\phi_{5}^{H_0}\\ r_{15}-r_{10}&=r_{10}-r_5\end{aligned} \tag{2.4}$$

should be satisfied. Therefore, from Eqs. (2.2), (2.3) and (2.4), $c(\omega)$ for downdip propagation is greater than that for updip propagation in the period range 20–38 s, because the relation

$$\delta\phi_{15}^{H_e}-\delta\phi_{10}^{H_e}>\delta\phi_{10}^{H_e}-\delta\phi_{5}^{H_e} \tag{2.5}$$

is valid (Fig. 8).

On the contrary, for periods longer than 38 s, $c(\omega)$ is greater for updip propagation than for downdip propagation, because the following inequality is valid

$$\delta\phi_{10}^{H_e}-\delta\phi_{5}^{H_e}>\delta\phi_{15}^{H_e}-\delta\phi_{10}^{H_e}. \tag{2.6}$$

Thus, we can understand that the directional dependence of phase velocity is caused by significant differences in phase shifts (Fig. 8) between station pairs (5, 10) and (10, 15).

2.3 Site Dependent Phase Spectra

In the case of the plane Love wave incidence for Model D, the phase spectral characteristics on the free surface are shown in detail in Fig. 9. The ordinate indicates phase spectral differences between Models D and A at each site.

The sites from 1 to 5 are located outside the concave Moho discontinuity. In this domain, the phase variation is significant at short periods near 20 s.

As sites from 5 to 10 in the domain defined by downdip propagation, the phase shifts increase slightly as site number increases. They are approximately constant in the period range 20–50 s at site 10.

The phase shifts at sites from 11 to 15, in the domain defined by updip propagation, increase as site number increaes.

Sites from 16 to 19 are located outside the concave Moho discontinuity. The phase shifts, however, exist conspicuously. The characteristics show maximum variations at periods near 20 s, and decrease as period increaes. It is interesting that phase shifts exceed those at sites from 1 to 5, which are also outside the interface.

These phase characteristics are summarized as follows. In the period range 20–50 s, the phase variation is smallest at site 5, intermediate at 10, and largest at 15.

In this way, it is understood from Fig. 9 that the phase variations of Love waves across the interface are systematically and strongly related to the propagating direction of the waves. This systematic variation is, as will be investigated in Part 3, in good harmony with systematically varying amplitude spectra of scattered waves.

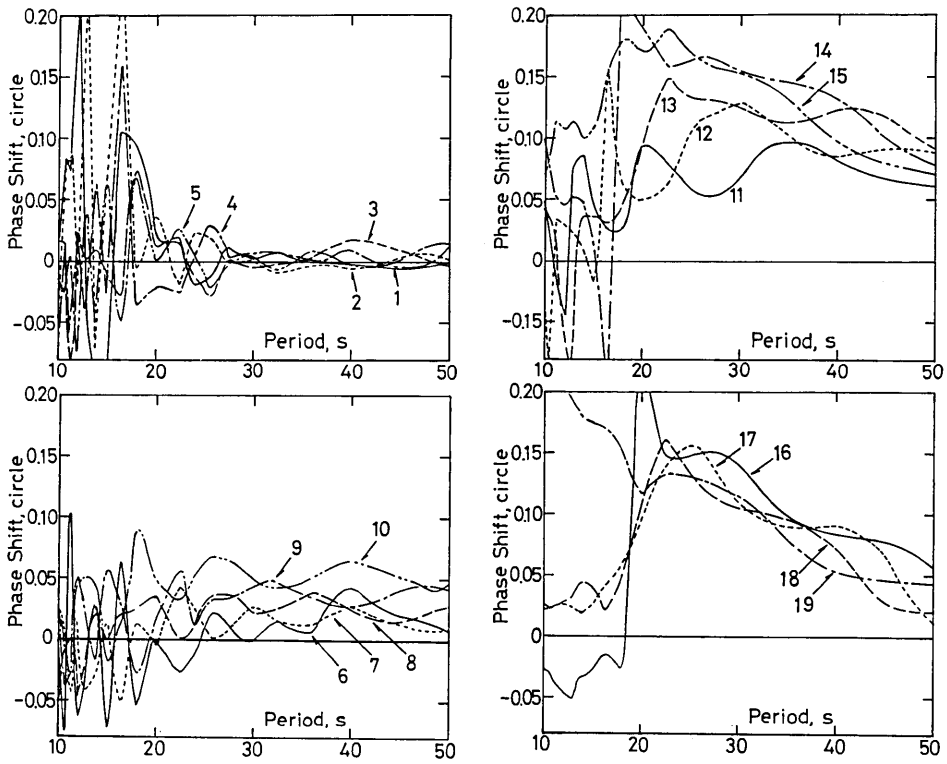

Fig. 9. The phase shift at sites from 1 to 19 in units of a circle (1 circle=2π radian). The numbers attached to the curves correspond to those in Fig. 6(a).

2.4 Site Dependent Amplitude Spectra

In Fig. 8(b), the Fourier amplitude variations are also shown by plotting the ratios of amplitude spectra for Model D to those for Model A, calculated at sites 5, 10 and 15.

Distinct features of amplitude characteristics are found as follows: At site 5, the amplifications are large at short periods near 20 s, compared to values of about 1.0 in the period range 30–40 s. At site 10, the amplifications generally increase as period increaes, but, they are smaller than 1.0 over the whole period range shorter than 42 s. At site 15, the amplifications become remarkably large at periods longer than 30 s. They approach 1.6 at a period of 42 s. The above features point out that amplitude variations, as well as the phase variations, are greatest when the incident plane Love waves are passing the concave structure from its far side.

Next, Let us observe in detail the amplitude characteristics in Fig. 10. The figure shows the amplitude characteristics at the set of sites shown in Fig. 9. The amplitude characterestics near sites 5, 10 and 15 respectively resemble those at sites 5, 10 and 15. They vary systematically as the number increases. The amplitude characteristics at sites from 16 to 19, outside the interface, show gradual decreases of amplitude as the number increases.

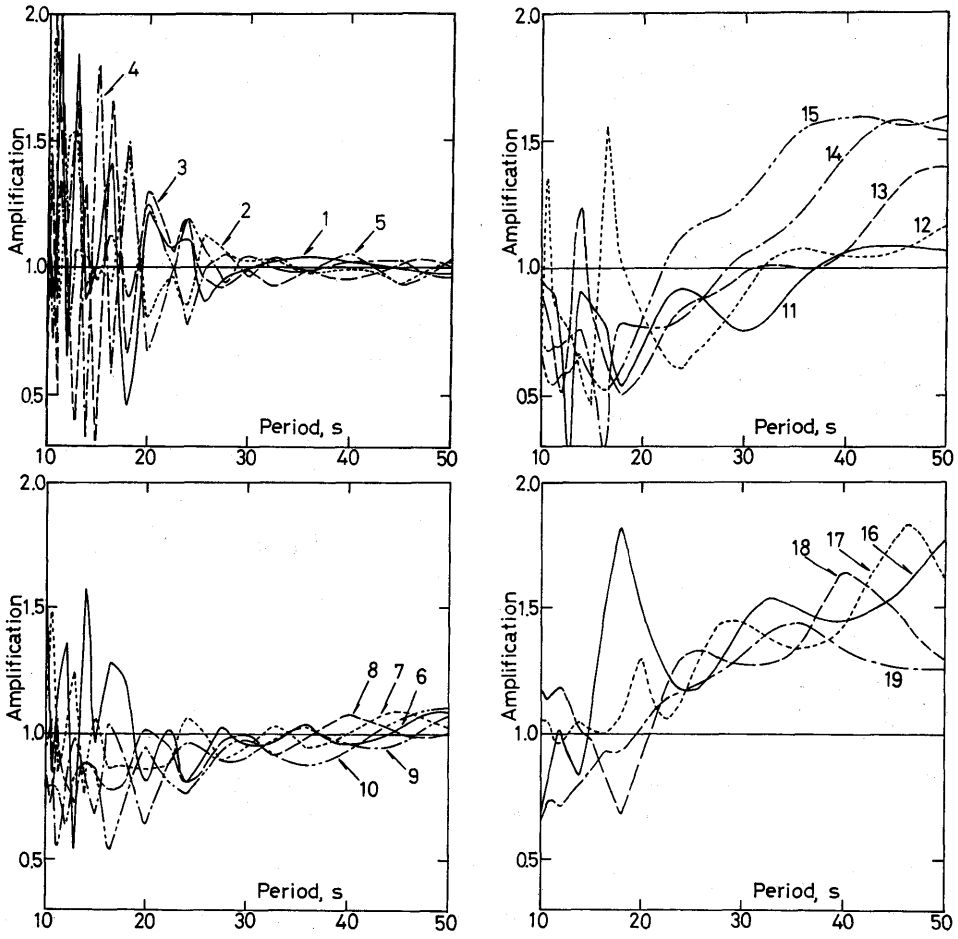

Fig. 10. The amplification at sites from 1 to 19. For the numbers see the caption of Fig. 9.

The systematic variations of amplitude characteristics observed from Fig. 10, as well as those of the phase characteristics, are closely related to the growth of scattered waves and radiation mode of body wave energy dependent on propagating direction, which will be investigated in Part 4.

2.5 Phase and Amplitude Spectra of Love Waves across the Concave Structure with Smoothly Varying Layer Boundaries

As was shown in Fig. 6(d), the phase velocities for a concave structure (Model E) whose layer boundaries are varying smoothly are stable compared to those for Model D. The phase shifts and amplifications for Model E at sites 5, 10 and 15, were calculated and are shown in Fig. 11. These characteristics correspond to those in Fig. 8 for Model D.

We see from Fig. 11 that all the phase shifts at the three sites vary smoothly over

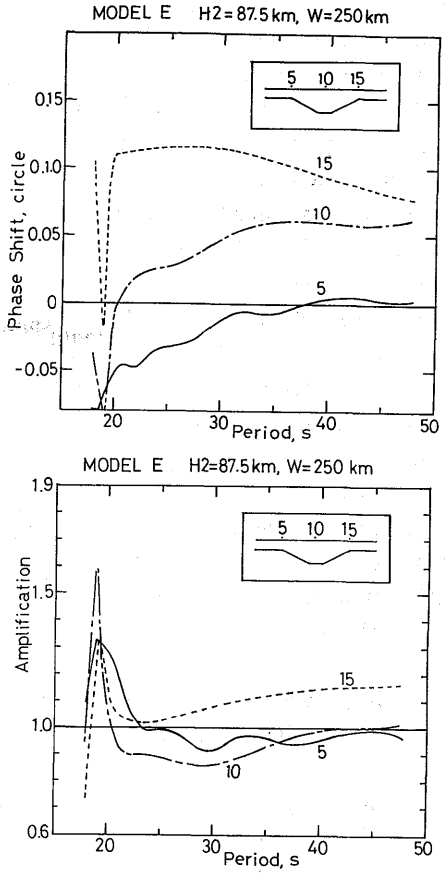

Fig. 11. Perturbations of the phase (Top) and amplitude (Bottom) spectra of the displacement component of Love waves at sites 5, 10 and 15 for Model E. Legend as for Fig. 8. For the symbols of H2 and W see Fig. 6(d).

the entire period range of 20–48 s and the relative differences of phase shifts between station pairs (5, 10) and (10, 15) show smooth variations. This suggests that phase velocity anisotropy can be reliably detected.

The amplifications in Fig. 11 also show smooth variations, but the characteristics whereby amplifications increase with decreasing period at sites 10 and 15, at short periods of 20–30 s are somewhat different from those for Model D. The characteristics of large amplifications at short periods near 20 s at sites 10 and 15 for Model E are not found in Model D, and are investigated later in this chapter using different models of irregular structures.

2.6 Irregularity of Phase and Amplitude

In the prvious section, variations of phase spectral characteristics on a free surface, both inside and outside the concave structure of the Moho discontinuity, were quantitatively investigated. Considering a fact that these variations of phase

characteristics are caused by irregular structures of the Moho discontinuity, the variations of the phase characteristics should be strong inside the media. To inspect in detail variations of amplitude and phase characteristics, snap shots of the displacement field in the media are shown in Fig. 12 for nonuniform and uniform wave guides. These tomographic snap shots represent the two-dimensional wave motion field at $T=140$ s, after a plane Love wave incidence upon the media. The positive (solid lines) and negative (broken Lines) displacements correspond to the particle motions upwards and downwards from the paper surface, respectively. The numerals given on the free surface along the abscissa denote distances from the left side of the computation space of Models D, A and E, and the ordinate indicates depths. The numerals written along contours represent the relative amplitudes of the displacement. In the media, the Moho discontinuity is drawn with thin lines in the figure.

These snap shots are calculated when the incident plane Love waves reach the far side of the concave interface of the Moho discontinuity (see also Fig. 13). The figures clearly show that the phase and amplitude distributions are strongly disturbed by the irregularity (Model D). Namely, in the uniform wave guide (Model A), the positive displacements are distributed in the distance range 600–700 km and the depth range 175–230 km, while in the nonuniform wave guide (Model D) the displacements are negative in that domain. This domain in Model E has distributions similar to those for Model D.

Furthermore, in the uniform wave guide the displacement amplitudes are largest on the free surface and decrease gradually as depth increases, while in the nonuniform waveguide for Model D the regularity crumbles and irregular amplitude and phase distributions appear at the shallow parts (e.g., negative peak of -14 appears within the crust at a distance of 650 km) or deeper parts (positive peak of $+1.8$ appears in the mantle at a depth of 60–175 km, under the concave Moho discontinuity in the distance range 530–640 km).

Similarly, irregular amplitude and phase distributions appear for Model E. Namely, the displacement distribution has a negative peak of -19 in the crust at a distance of 650 km, and has a positive peak of 0.9 in the mantle at depths of 165–170 km.

As another notable feature of the displacement distributions for Model D, the above-mentioned displacement contour of peak $+1.8$ is found to be distributed obliquely at a distance of 550 km and at a depth of 100 km, and links with the displacement distribution with a positive maximum of 35 on the free surface at a distance of 700 km, under the concave Moho discontinuity at a depth of 170 km. The

Fig. 12. The amplitude distributions of displacement components inside the heterogeneous structure including a set of steps of the Moho discontinuity (Model D), the horizontal structure (Model A) and the concave structure with smoothly varying layer boundaries (Model E). The distributions are shown at a time of $T=140$ sec for the horizontal range from about 500 to 750 km and for the depth range from 0 to 254 km. The positive and negative components of the displacement are denoted by solid and dashed lines respectively. The numerals attached to the lines indicate relative amplitude.

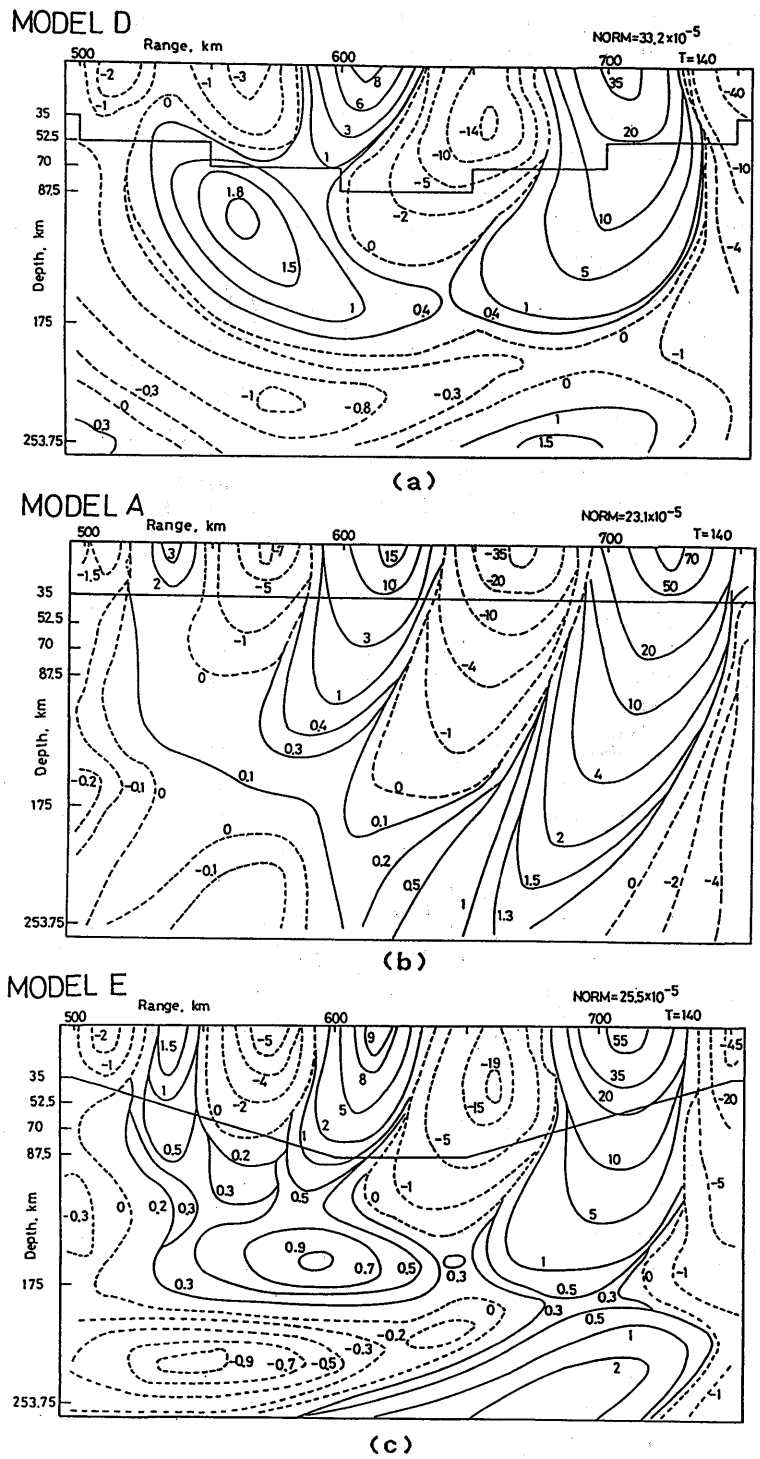
MODEL D
Range, km
NORM=33.2×10⁻⁵
T=140
Depth, km
(a)
MODEL A
Range, km
NORM=23.1×10⁻⁵
T=140
Depth, km
(b)
MODEL E
Range, km
NORM=25.5×10⁻⁵
T=140
Depth, km
(c)

Fig. 12.

linked contour forms a semicircular displacement distribution. Under this positive displacement contour, the semicircular negative displacement contour with a minimum of -1 and a larger radius is distributed just as if it enclosed both edges of the concave Moho discontinuity. The similar linked contour patterns close to those of Model D are also found with Model E. These features expose distinct phenonmena which cannot be observed in the uniform wave guide (Model A).

As discussed in Part 3, these features arise from the multiple scattering of Love waves. Overall, we notice from Fig. 12 that the characteristics of the displacement distibution for Model E are close to those of Model A in shallow parts, but are close of Model D in deeper parts. These characteristics suggest that the scattering in Model E primarily affects the wave field under the smoothly varying layer boundaries.

2.7 Spatio-Temporal Variations of Wave Field

A set of snap shots of the amplitude and phase distributions of the displacement across the concave structure of the Moho discontinuity (Model D) is shown in Figs. 13 and 14. For comparison, snap shots for the uniform wave guide (Model A) are also given in Figs. 15 and 16. The horizontal continuous solid line in the figure represents the Moho discontinuity. The space extends two-dimensionally to a distance of 1000 km along the abscissa and to a depth of 500 km along the ordinate.

At time $T=14$ s, the fronts of Love waves are just incident on the concave structure of the Moho discontinuity, while at time $T=140$ s the waves are passing over the far side of the interface. The energy distribution is such that the shade is distinguished every half square of the displacement amplitude (attenuation of 3 dB) and darker shades indicate larger amounts of energy. Areas of positive and negative displacements are black and gray, respectively.

As shown in the energy and phase distributions at $T=14$ s, the incident Love waves consist of several wave trains with large positive and negative amplitudes. The waves have the largest amplitude of positive displacement in the second wave train (marked by a vertical bar). Upon inspecting a set of snap shots at various times we can find following characteristics with respect to the propagation of Love waves in the hetrogeneous structure of the concave Moho discontinuity.

1) Until the incident Love waves with prominent amplitudes arrive at the deepest portions of the concave Moho discontinuity ($T=70$ s), the amplitude and phase distributions of Love waves across the interface (Figs. 13 and 14) are not so different as those of the uniform wave guide (Figs. 15 and 16).

2) The energy distribution, which extends to deeper parts and curves towards the left in the half-way after the time near $T=112$ s (Fig. 13) for the nonuniform wave guide, correspond well to those of semicircular phase distributions (Fig. 14). The tendency increases with time up to $T=140$ s.

3) The pattern of the amplitude distributions of the incident Love waves ($T=14$ s), for the uniform wave guide, does not vary notably even if the time elapses to 140 s (Fig. 15). On the contrary, the pattern of phase distributions varies slowly with time (Fig. 16).

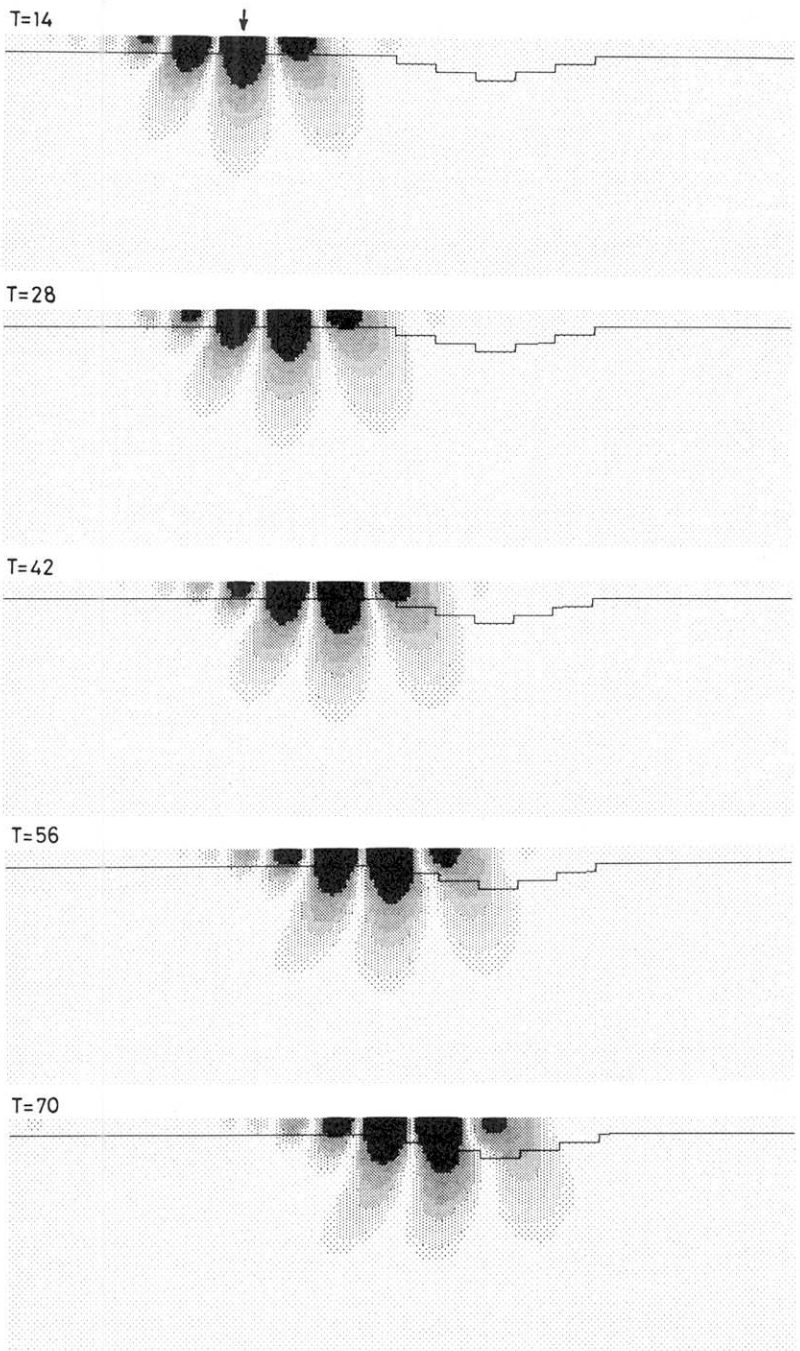

Fig. 13. The energy distributions of Love waves for the nonuniform wave guide (Model D) at various instants in time (T) from 14 to 140 s. The depth of shading fades every half square of displacement amplitude (-3 dB). A vertical bar indicates a location of a wave train with maximum energy.

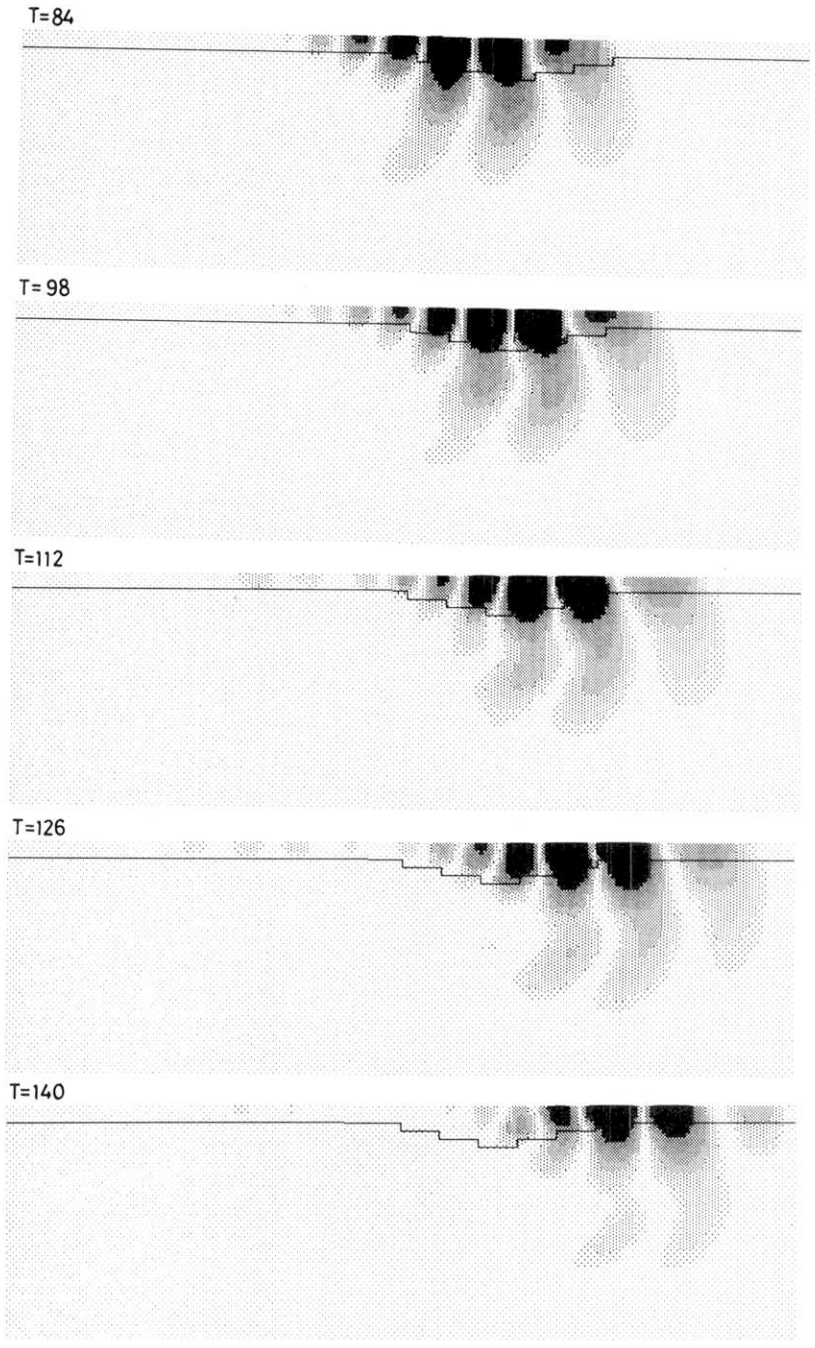

Fig. 13. continued.

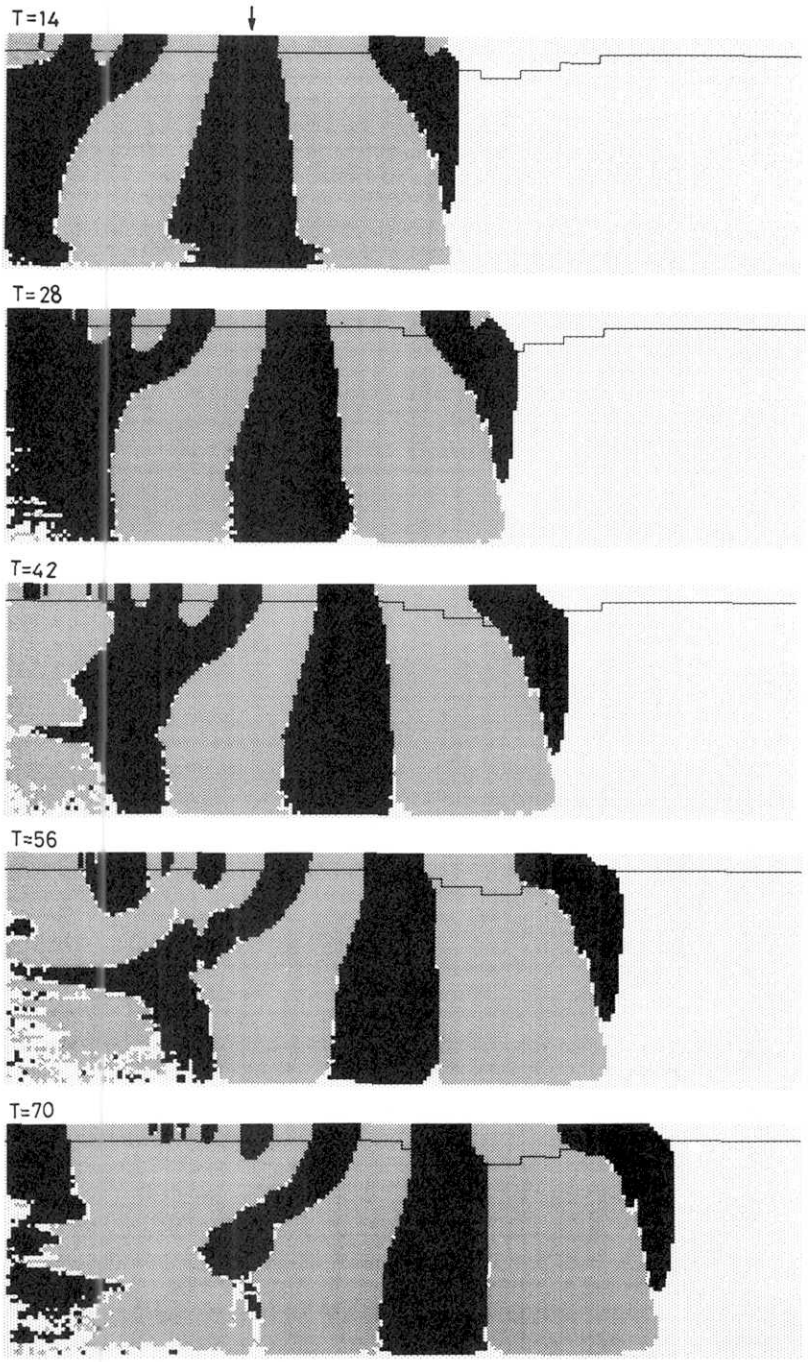

Fig. 14. The phase distributions of the displacement of Love waves for the nonuniform wave guide (Model D) at various instants in time (T) from 14 to 140 s. The black and shade areas designate regions of positive and negative components of the displacements, respectively. For the vertical bar see the caption in Fig. 12.

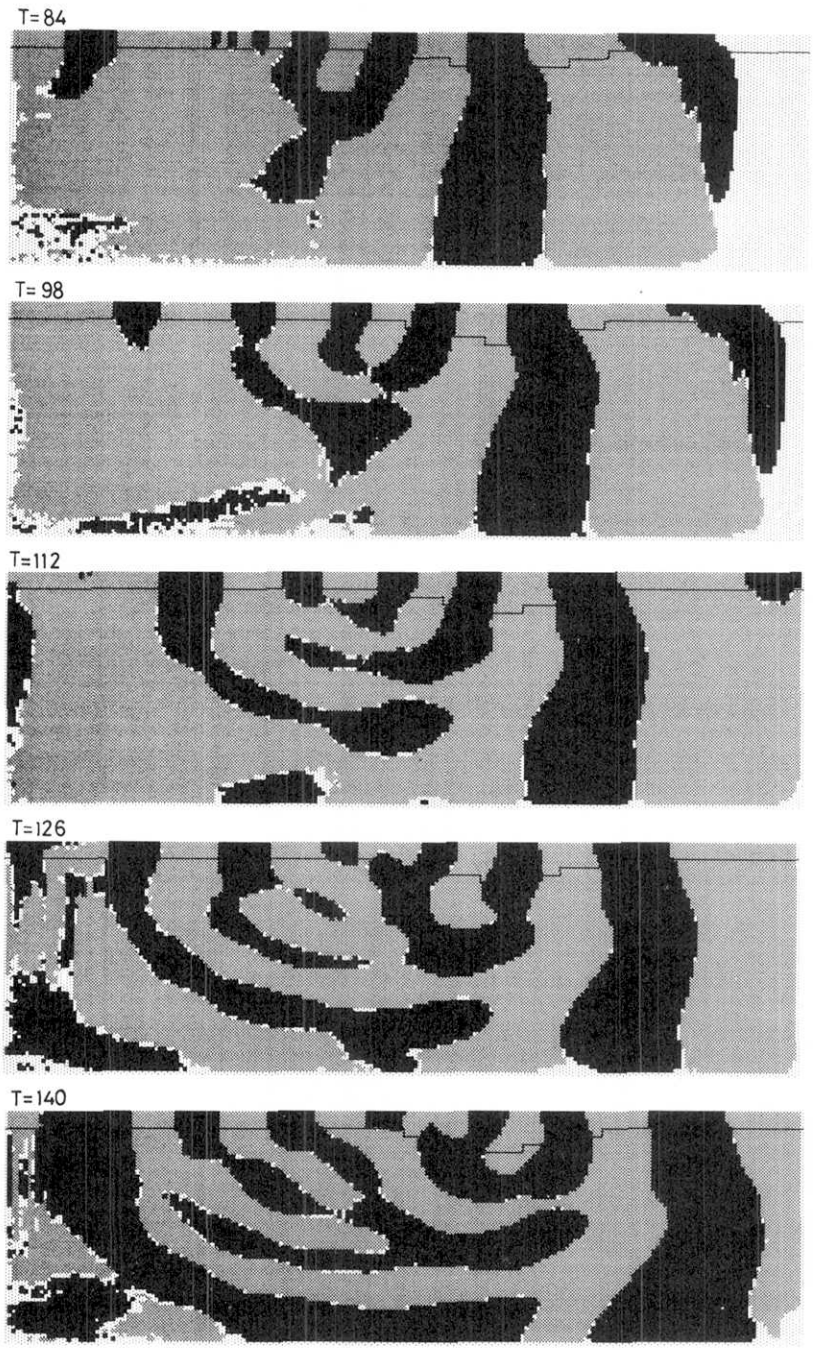

Fig. 14. continued.

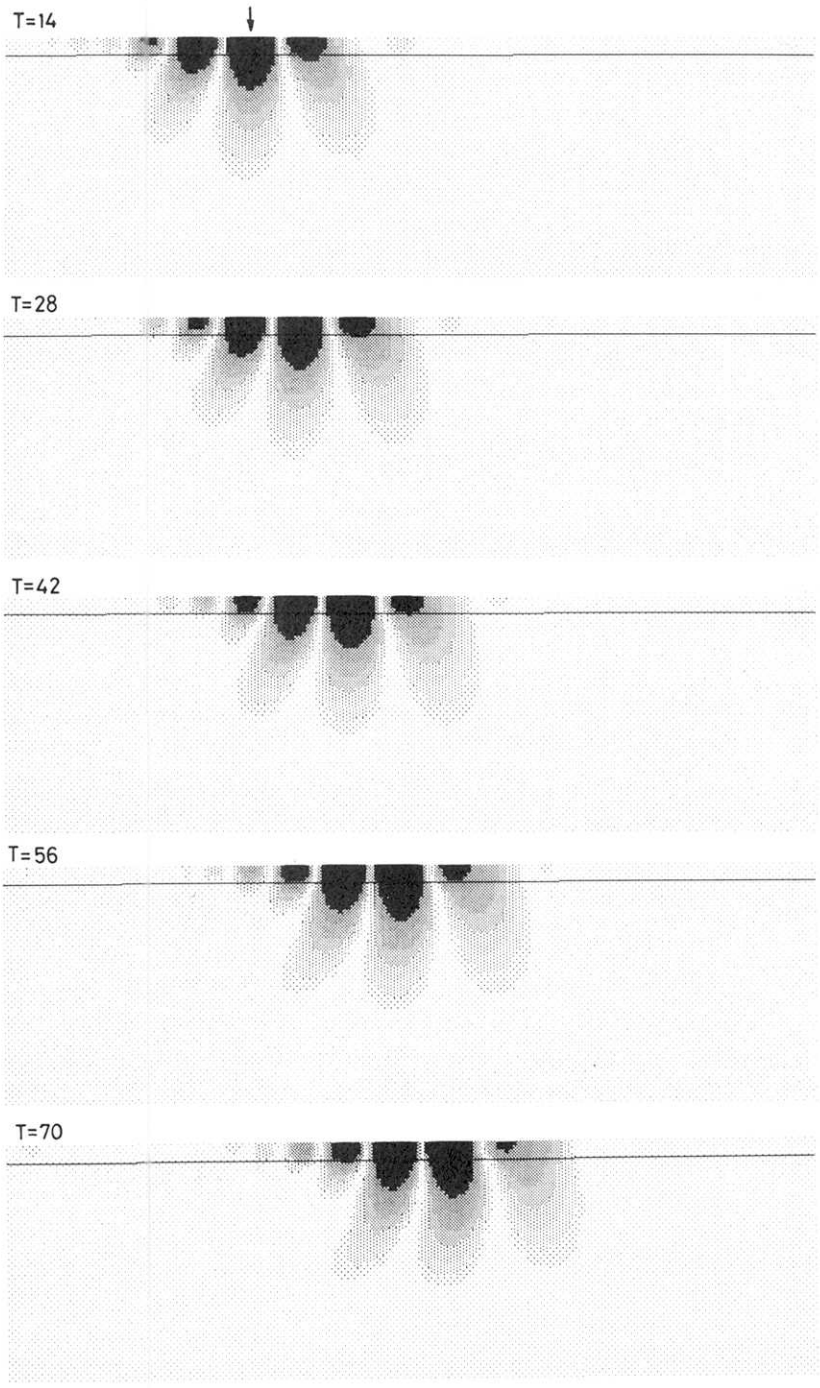

Fig. 15. The energy distributions of Love waves for the uniform wave guide (Model A) at various instants in time (T) from 14 to 140 s. For the shaded marks and vertical bar see the caption of Fig. 13.

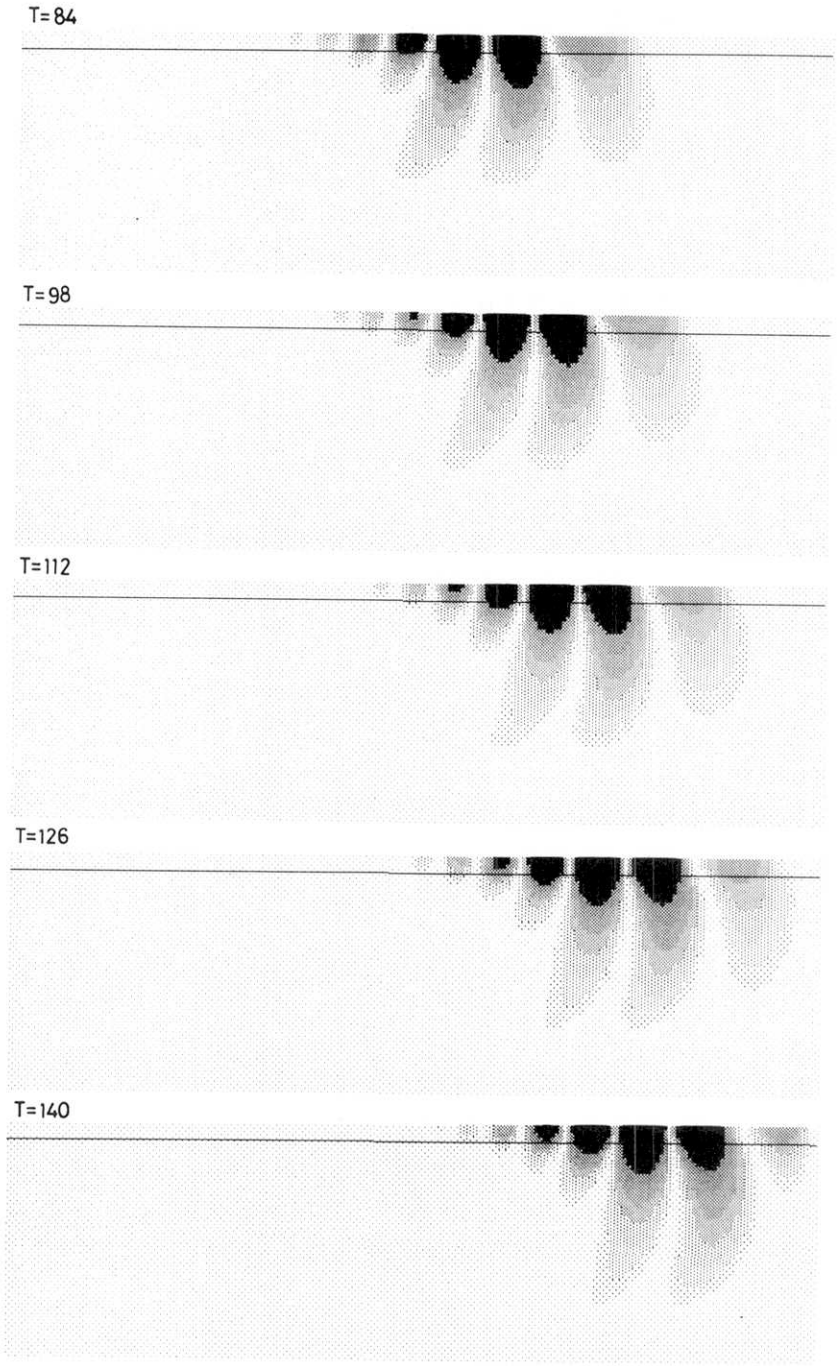

Fig. 15. continued.

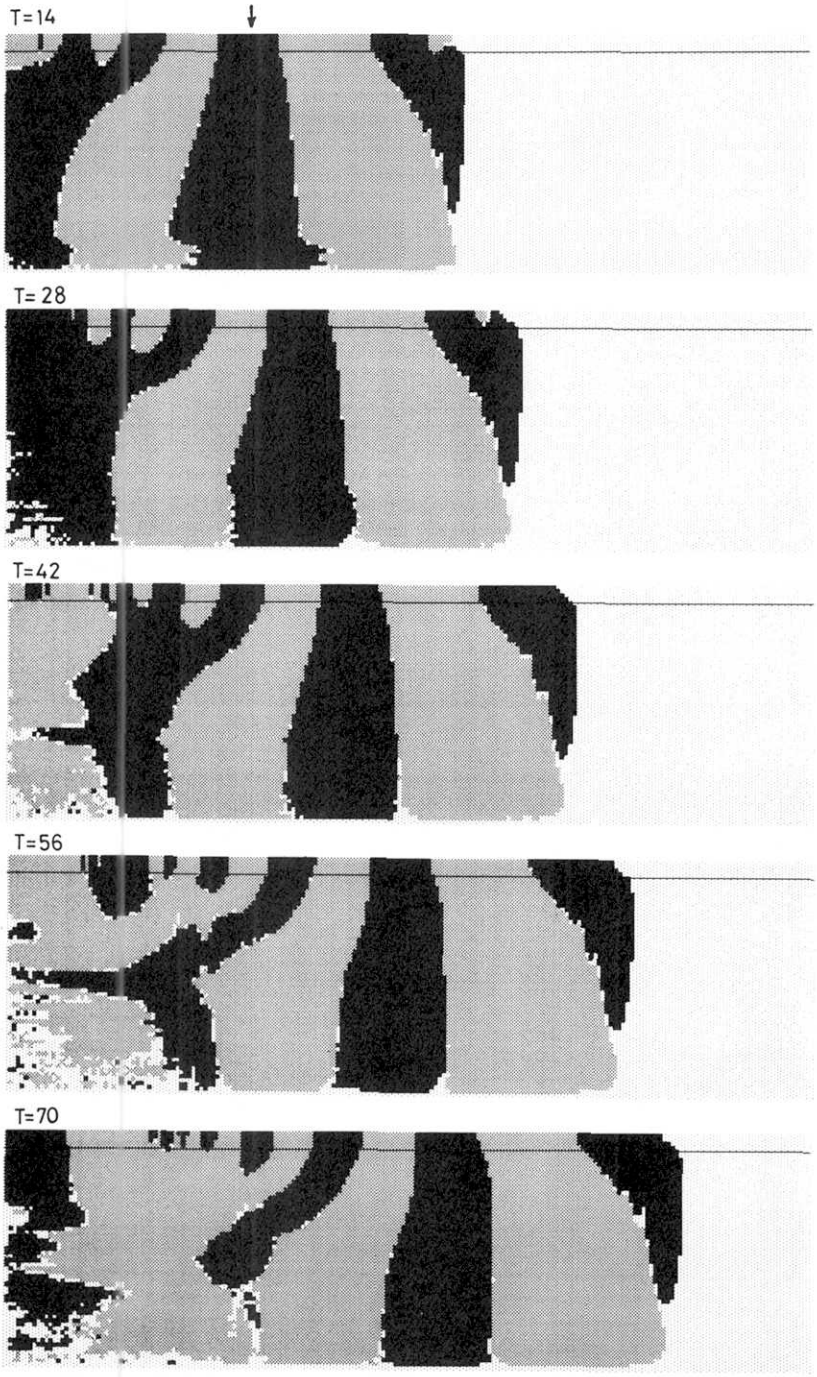

Fig. 16. The phase distributions of the displacement of Love waves for the uniform wave guide (Model A) at various instants in time (T) from 14 to 140 s. For the black and shaded marks see the caption of Fig. 14. For a vertical bar see the caption of Fig. 13.

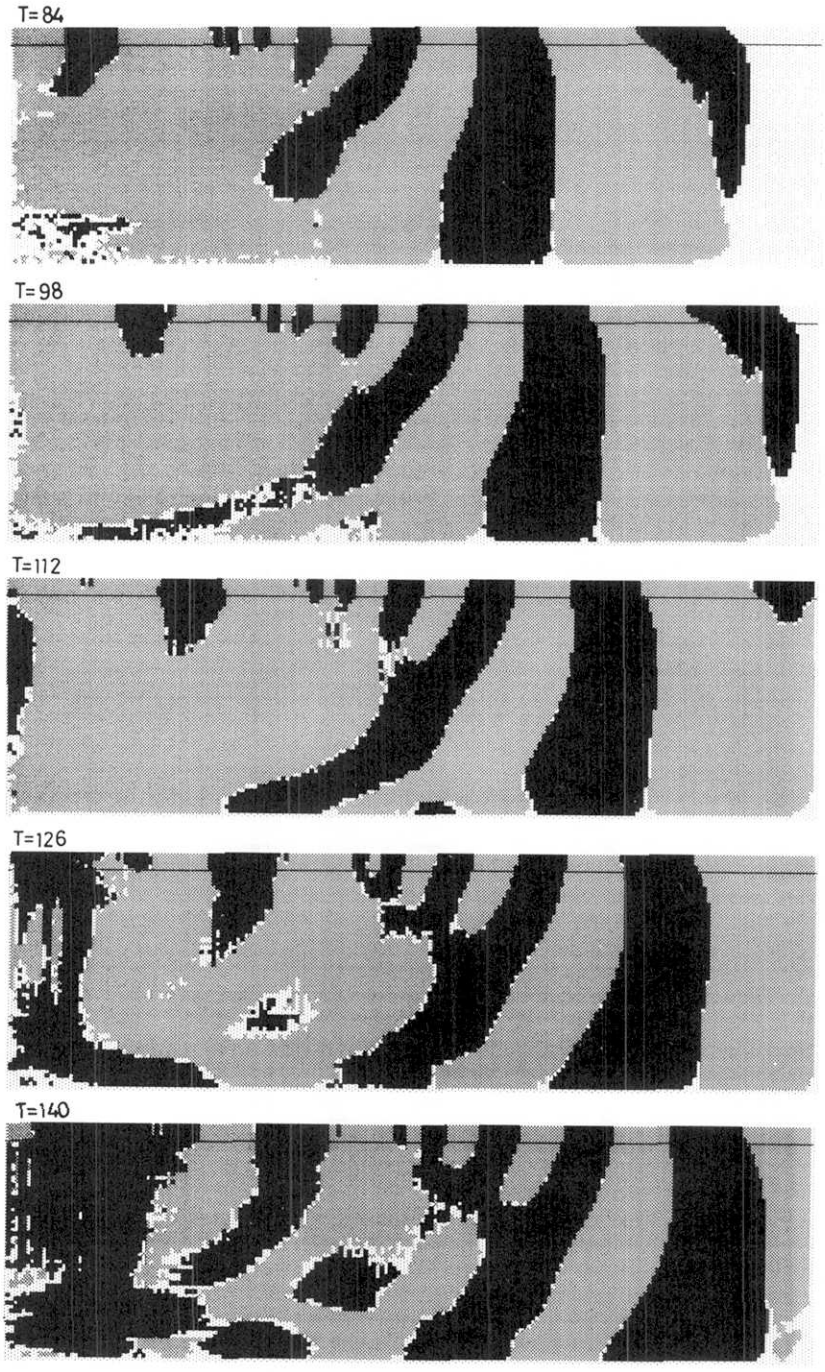

Fig. 16. continued.

4) At the time the waves travel over the concave Moho discontinuity ($T=$ 140 s), the high amplitude region is separated into two clusters at intermediate depths in the mantle (Fig. 13).

5) It can be commonly understood for both uniform and nonuniform wave guides that Love wave energy is concentrated in the crust (Figs. 13 and 15).

Characteristics 2) and 4) described above can be interpreted in that the incident plane Love waves are partly reflected and diffracted at steps of the vertical Moho discontinuity, and that the wave motion field is distorted by the scattering of Love waves due to interference between incident, reflected, transmitted and diffracted waves. In terms of visual snap shots, the characteristic 3) expresses that the phase spectra vary with distance propagated but the amplitude spectra do not.

2.8 Behavior of Love Waves in Nonuniform Wave Guides with Different Horizontal Lengths and Depth of Concave Structure

In this section, the dependence of the propagation of Love waves on the horizontal and vertical extents of the concave structure is investigated with respect to phase velocity dispersion and amplitude spectra.

2.8.1 Models and Time Series of Waves

In Fig. 17, Models F, G, H and I are shown together with Models D and E, which were previously examined. In these models, the horizontal length (W) and the vertical extent (H2) of the interface are varied while fixing the depth of the flat part at H1. H2 differs between Models F and G, and W differs between Models G, H and I.

The time series of waveforms computed for these models are shown in Fig. 18, in which those for the uniform wave guide (Model A in Fig. 1) are also plotted for comparison purposes. The symbols W (windward), M (midpoint) and L (leeward) beside site numbers mean both edges and midpoint of the interface.

We see from the figure that the perturbations in the phase and amplitude components due to the irregularities of the interface are strong for Model F, and for Models D and E. The perturbations increase towards the leeward, and the scattered waves appear in later seismograms. For Models G and H, small phase delays are observed at the windward side near the edge (W). But, on the whole, the perturbations are small compared to those of F. For Model I, the perturbations increase towards the propagating direction from the midpoint to the leeward. Through these seismograms for the various models, we can infer that the vertical extent of the interface has most effect on distortion of incident waves.

2.8.2 Characteristics of Phase Velocity Dispersion

The phase velocities calculated for Models F, G, H and I are shown in Fig. 19. The characteristics of phase velocities for Model F are surprisingly similar to those for Model D. For Models G and I, on the whole, the phase velocities for updip propagation are equal to or higher than those for downdip propagation. For Model H, phase velocities vary abruptly as period increases. This characteristic arises because the station pairs are very close to the edges of the step. Love waves on the

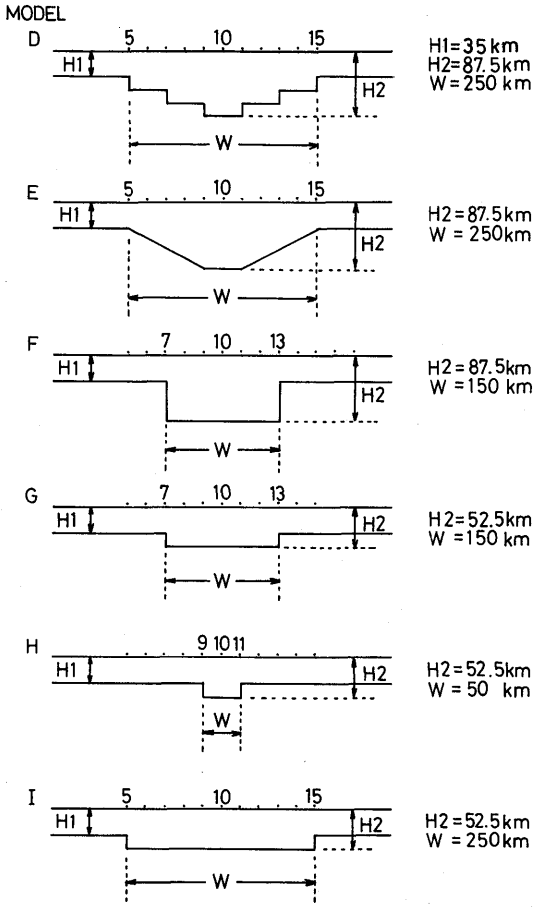

Fig. 17. Schematic diagrams of two-dimensional elastic models. The depths of the surface layer and the bottom of the concave structure are denoted by H1 and H2, and the horizontal length of the interface by W. Models D and E are the same as those given in Figs. 1 and 6(d), respectively.

stations are severely distorted by SH waves generated at the edges, which is investigated in Part 3. The average phase velocities along the interfaces of Models G and I increase from the lower limits at short periods to the upper limits at long periods as period increases. These characterist are common to those for Models D, E and F.

The numerical results obtained above for Models G and I suggest that if the vertical extent of the interface is not so large, the characteristics of phase velocity anisotropy approach those for media with sloping layers as analyzed by BOORE (1970) and LEVANDER (1985).

2.8.3 Characteristics of Amplitude Spectra

The characteristics of the amplifications for Models F, G, H and I were computed and are shown in Fig. 20. Comparing Fig. 20 with figs. 8 and 11, we see that the characteristics of the amplifications for Model F are similar to those for

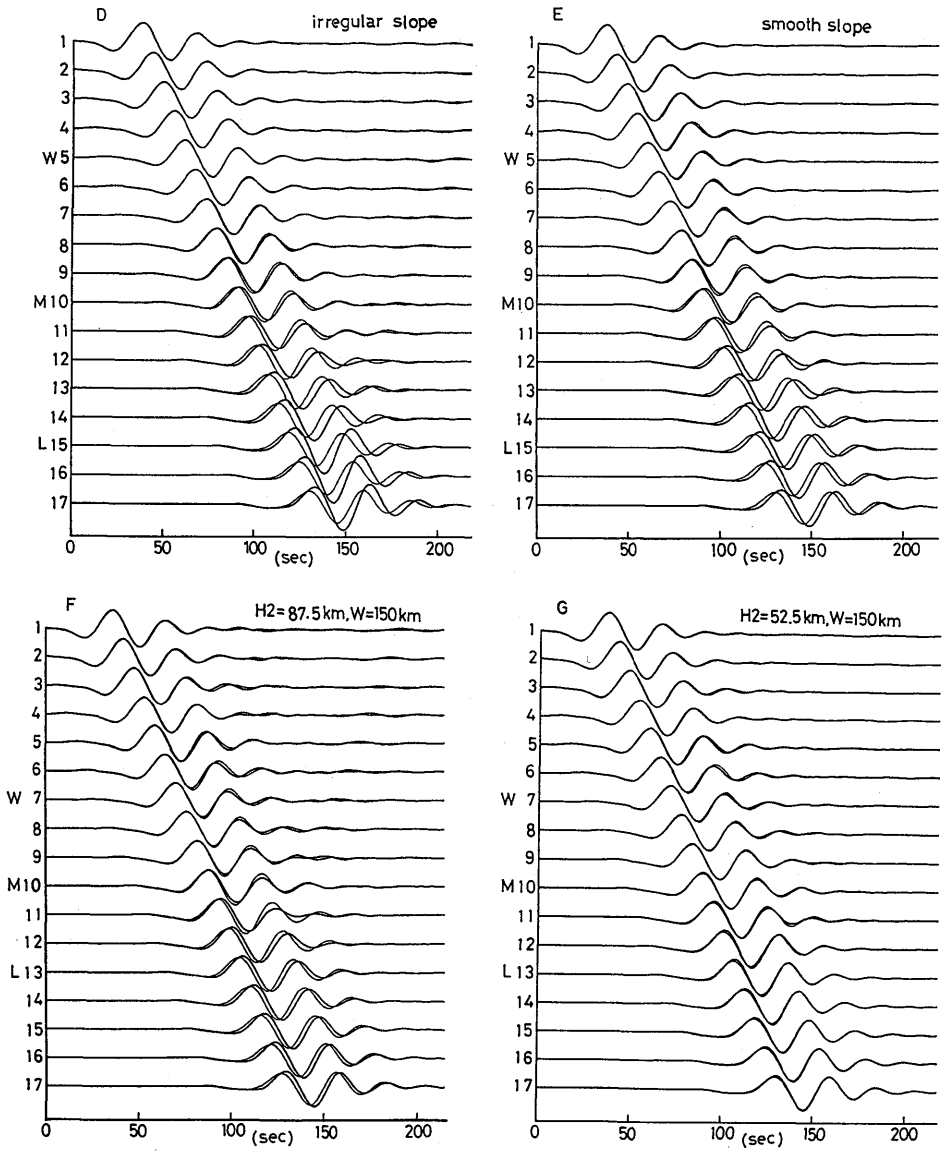

Fig. 18. Computed seismograms of Love waves for various sites along the surface for the models in Fig. 17. The model name is indicated by a capital alphabet at the upper left of the figure. The seismograms for Models D, E, F, G, H and I are plotted by thick lines, along with those for the uniform wave guide (Model A in Fig. 1) by thin lines. The symbols *W*, *M* and *L* attached to the site numbers on the ordinate mean, respectively, the locations of windward, midpoint and leeward over the interface.

Model E over the whole period range.

The amplifications for Models G and I show constant values of 0.9–1.1 at periods 23–48 s, and they become large as site number increases. At short periods near 20 s,

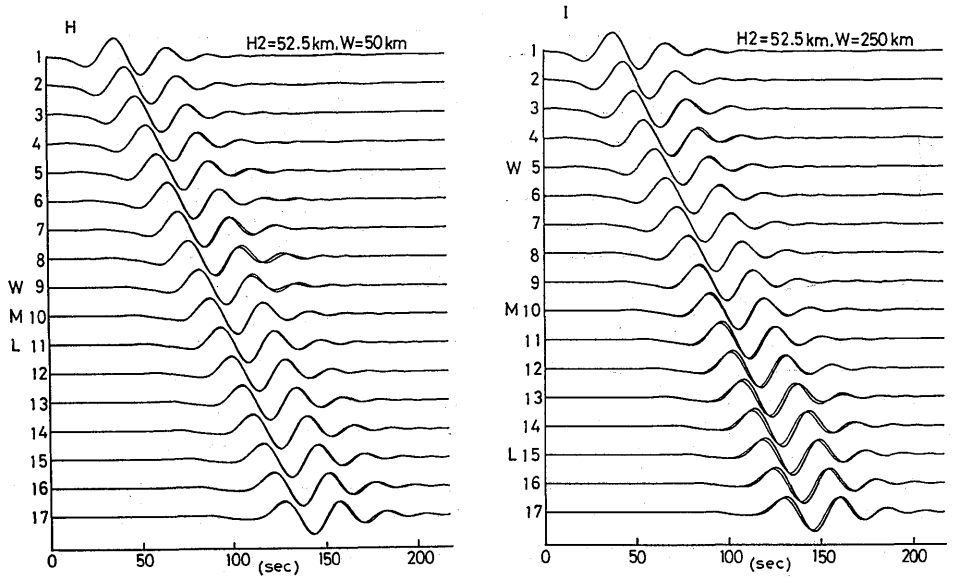

Fig. 18. continued.

the amplifications abruptly increase. The amplifications for Model H are not so different from those for Models G and I.

As is investigated in Part 4, amplification, which is equivalent to the transmission coefficients defined in Eqs. (1.19) and (4.5), depends on propagation mode, such as the downdip and updip propagations. Furthermore, just above the irregular layer boundaries, it suffers severely from body waves converted from Love waves. Therefore, the increase of amplification at short periods near 20 s for the simple Models F, G, H and I might be caused by the superimposition of SH waves generated at the windward edge of the interface. The energy of SH waves superimposed on the transmitted waves might propagate towards the leeward, because there are no irregularities up to the leeward edge of the interface. Thus, with respect to the characteristics of amplifications, Model E might be classified as a simple model like Models F, G, H and I.

2.8.4 Characteristics of Phase Velocity Anisotropy in the Media with Smoothly Varying Layer Boundaries

To study the dependence of characteristics of phase velocity anisotropy on station locations, the phase velocities were computed for Model E, as shown in Fig. 21. The station pairs are located symmetrically in downdip and updip propagations.

The figure shows that (1) the phase velocities for the two propagation modes become lower as the station pairs cover more largely the region of the middle parts of the interface, (2) the phase velocities for updip propagation tend to exceed the upper and lower limits of phase velocities in the media, while those for downdip propagation are always within the two limits, and (3) phase velocity anisotropy appears in all station pairs.

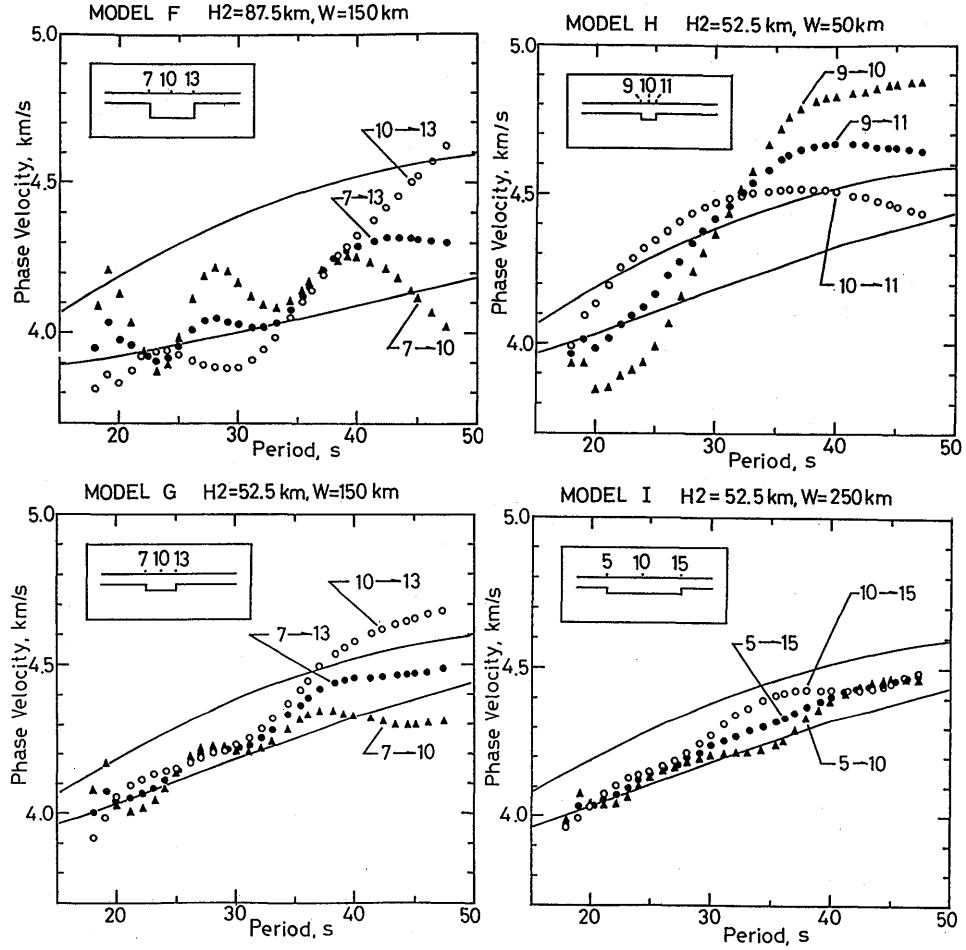

Fig. 19. Phase velocities over the region of nonuniform wave guides, calculated for Models F, G, H and I; the downdip (solid triangles) and updip (onen circles) propagations and the entire region (solid circles). Two solid curves (upper or lower limits) denote theoretical phase velocities, calculated for uniform wave guides with the crustal thickness of H1 (Fig. 17) or H2.

Feature (1) is interpreted as meaning the phase velocity decreases as the area of the crust increases under the station pairs. Feature (2) might arise, as is investigated in Parts 3 and 4, from the stronger effects of scattered waves on updip propagation than for downdip propagation. Feature (3) is considered as the general characteristics in the concave structure.

2.9 Concluding Remarks of Part 2

Using Fourier phase and amplitude spectra of Love waves across the mountain root structure, represented by a concave interface of the Moho discontinuity, the phase and amplitude characteristics on the free surface were investigated. The

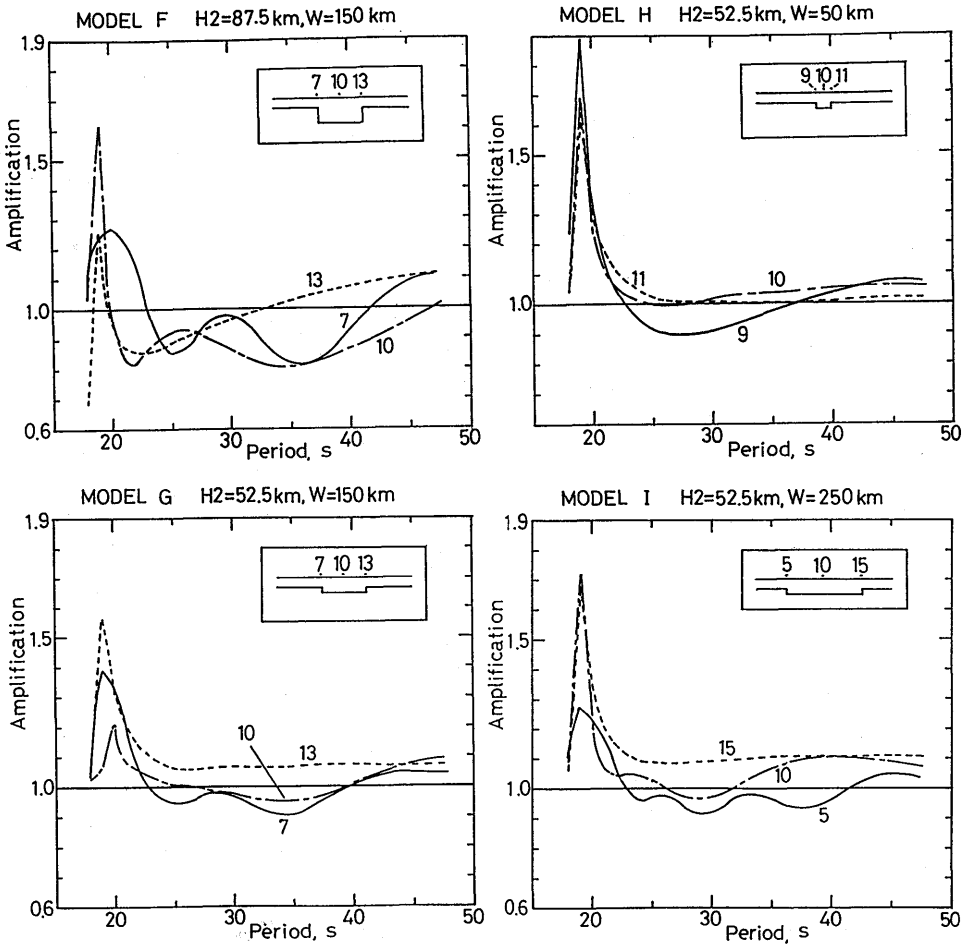

Fig. 20. Perturbations of amplitude spectra at sites 5, 10 and 15, calculated for Models F, G, H and I. Legend as for Fig. 8.

tomographic snap shots of the wave motion field were also employed for a visual inspection of the phase and energy distributions in the crust and mantle including the irregular interface. The principal interesting characteristics, obtained with respect to the mechanism of apparent anisotropy and anomaly of the phase velocity, are summarized as follows;

(1) The variation of phase spectral characteristics on the free surface is greatest at the end point (leeward), intermediate at the midpoint, and smallest at the starting point (windward) of the mountain root structure.

(2) Apparent anisotropy of average phase velocities appearing between down-dip and updip propagations is caused by overwhelming differences in phase spectra between the two wave paths.

(3) From an inspection of successive snap shots, which two-dimensionally

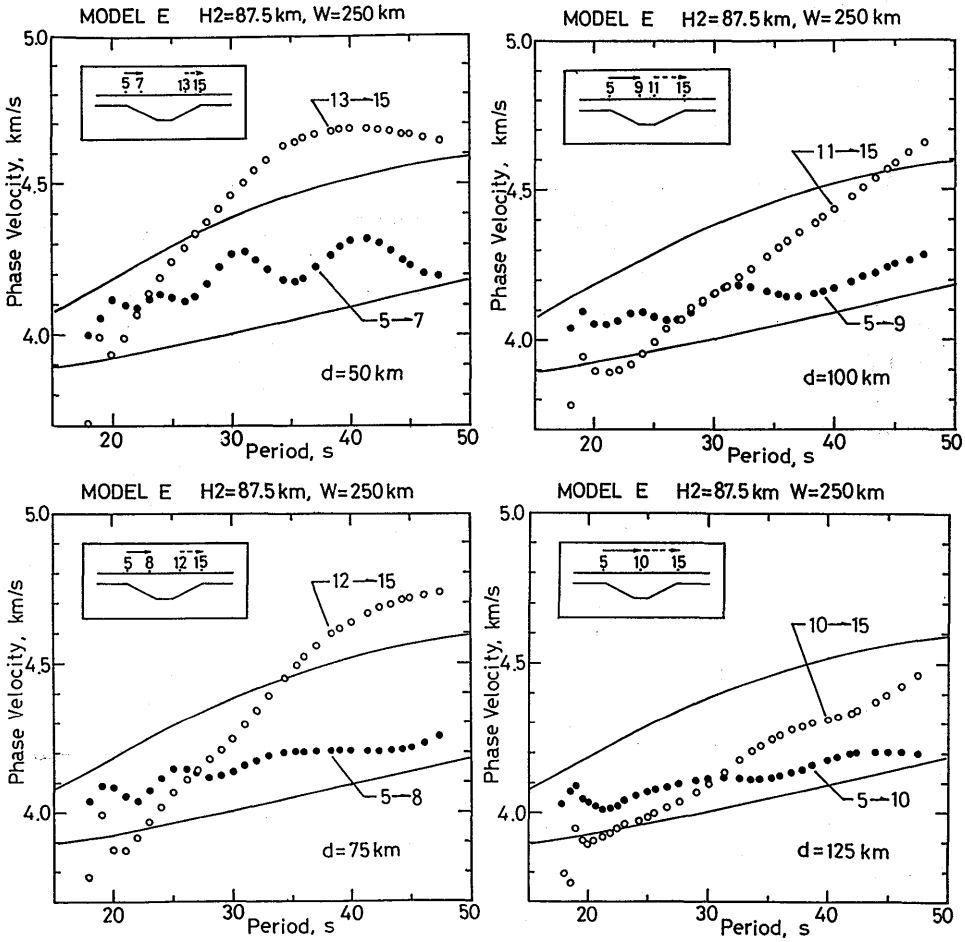

Fig. 21. Phase velocities at different locations of station pairs, calculated for Model E. The station pairs are symmetrically located in downdip and updip propagations.

depict variations of phase and energy distributions both inside and outside areas along the interface, the phase distortion is found to be strong in the domain under the irregular layer boundaries of the concave structure.

(4) Interference between the incident Love waves and the scattered waves strongly affects the amplitude of displacement, as well as its phase. It changes the locations of peak-amplitudes on the free surface and in deeper parts of the crust and the mantle, and splits the amplitude distribution which extends continuously from the surface to deeper parts into two clusters.

(5) In simple structures with few irregular layer boundaries, as represented by Models F, G, H and I, amplification (or the transmission coefficient) at the windward is high at short periods near 20 s. This characteristic also remains in those at the midpoint and leeward.

Part 3

Generation and Propagation of Scattered Waves in the Propagation of Love Waves across Irregular Structures of the Moho Discontinuity

3.1 Introduction

For wave propagation in nonuniform wave guides, scattering of elastic waves is important, and Love wave scattering has been investigated by MAL and HERRA (1965) analytically, and by ZAMA (1981) numerically using the finite element method. They investigated a simple model with a small step in a finite region over a half space. They studied amplitude and phase spectra of Love waves across the interface. Spatial distributions of amplitude and phase delays for free surface displacements in the downward or upward dented Moho discontinuity were investigated by AKI and LARNER (1970), for SH wave incident from below at various incidence angles. They showed that, for the incoming wave incidence along the surface, both amplitudes and phase delays become gradually larger to the leeward.

The diffraction of P, SV, and Rayleigh waves by topographical irregularities was studied by KAWASE (1988) and SANCHEZ-SESMA and CAMPILLO (1991), using the boundary method based on the boundary integral equation. From the numerical simulations, they found that in the medium of a semi-circular canyon diffracted waves called creeping waves appear inside the canyon. Using the discrete wave number boundary element method, KAWASE and AKI (1989) studied the response of a soft basin for vertically incident SH or SV waves of a period of 4 sec and found that surface waves generated at the edges of the basin are clearly propagating back and forth inside the basin. This result suggests that the effects of scattering are great at the edges of irregular structures.

In the studies described above, however, scattering properties, such as how scattered waves are successively generated at laterally heterogeneous layer boundaries and how the scattered waves propagate around complicated boundaries in the media, have not been investigated. Accordingly, the behavior of scattered waves near boundaries has not yet been solved, particularly in the time domain.

In this Chapter, the generation and the propagation of scattered Love waves across a symmetrical mountain root structure are investigated using tomographic snap shots of the wave field of scattered waves. For this purpose, the snap shots, which are calculated using the finite difference method, are employed in the analysis, and the behavior of the scattered waves is analyzed graphically.

The mountain root structure, as shown in Fig. 6(a), forms a concave structure of a Moho-discontinuity, which protrudes into the mantle in a finite region, with a slope angle of about 20°. The analogy between the scattering of long waves along the continental shelf with a concave bay (MOMOI, 1981) and the scattering of Love waves across the mountain root structure is also investigated.

3.2 Definitions of Scattered Waves

According to nomenclatures associated with the scattering of seismic waves, defined by AKI and RICHARD (1980), the entire seismogram v in heterogeneous media along the x–z coordinate at time t, consists of two parts, primary waves v^0 and scattered waves v^1:

$$v(t,x,z)=v^0(t,x,z)+v^1(t,x,z) \tag{3.1}$$

The primary waves would constitute the whole seismogram if the heterogeneities were absent. The scattered waves are generated by the interaction between primary waves and heterogeneities in the structure.

From Eq. (3.1) the scattered waves v^1 can be computed if the entire seismogram v and the primary waves v^0 are obtained. For the computation of snap shots of scattered waves, those of the entire seismograms (Figs. 13 and 14) and primary waves (Figs. 15 and 16), calculated respectively for the nonuniform and uniform wave guides, are employed in this chapter.

3.3 Generation of Scattered Waves

Figure 22(a) shows the schematic geometry of the nonuniform wave guide including a mountain root structure (the Model D in Fig. 1). The horizontal length and vertical maximum width of the interface are 250 km and 52.5 km at the center along the interface, respectively. The plane Love waves of the fundamental mode are assumed to be incident on the uniform wave guide and propagate towards the interface at the right.

In Fig. 22(b) the distributions of free-surface displacements, calculated at various times, are shown. The reflected waves appear near the dotted line. The incident plane waves, corresponding to the primary waves, are similar to the wave forms at 14 s (see also Fig. 28(b)).

To observe the process for generating scattered waves due to the mountain root structure, wave profiles (snap shots) of the particle displacement of scattered waves $v^1(t,x,z)$ for the following instants in times $T=(14, 28, 42, 56, 70, 84, 98, 112, 126, 140)$ s were calculated and are shown in Fig. 23. The times correspond to those given in Fig. 22.

The wave profiles (Fig. 23) consist of two kinds of displacement field; the phase distribution of positive (black) and negative (shade) components and the energy distribution (the square of the amplitude). The energy distribution is shown with the shade in units of 3 dB, where the intensity of the shade increases with the increase of amplitude.

The upper two figures in Fig. 23 show the phase (top) and energy (bottom) distributions of scattered waves at a time of 14 s ($T=14$). The numeral at the lower right in the energy distribution indicates the maximum amplitude, and the superscript indicates the sign of displacement. There is a vertical arrow at the location with the maximum amplitude.

As time increases ($T=28$), the scattered waves spread in all directions, and the

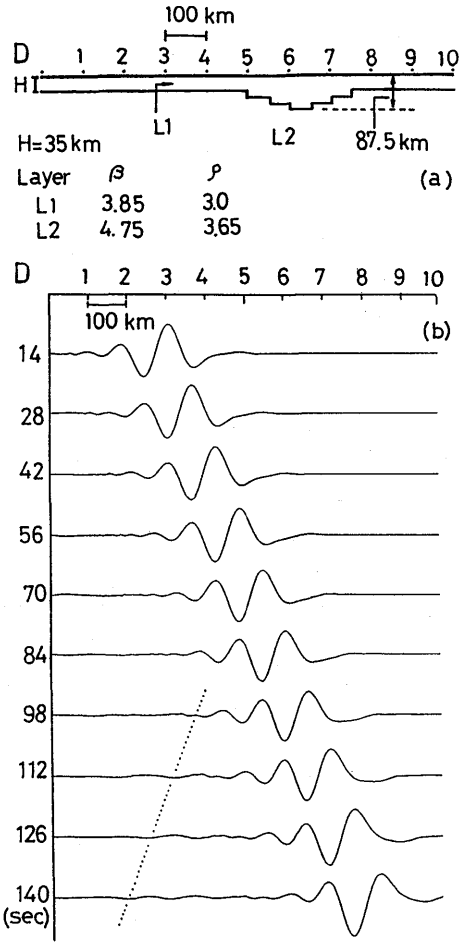

Fig. 22. (a) Two-dimensional geometries of the nonuniform wave guide with a mountain root structure (Model D). Legend as for Figs. 1 and 6(a). Plane Love waves propagate from left to right in the model. (b) The distributions of free-surface displacements of Love waves at various instants in time (T) written along the ordinate. The numbers along the abscisa correspond to those in (a). The reflected waves appear near a dotted line.

Fig. 23. The spatial distributions of the displacement component of the scattered waves at various instants in time (T) for Model D. The finite difference grid space has a horizontal length of 1000 km and a vertical depth of 500 km. Top: The phase distribution showing the positive (black) and negative (shaded) components of displacement. Bottom: The energy distribution showing the square of the amplitude of displacement. The color of the shaded parts fades with decreasing energy every half square of displacement amplitude (-3 dB). The numeral at the lower right corner denotes the maximum amplitude of displacement at time T. The positive ($+$) and negative ($-$) components of displacement are designated by the superscript on the numeral.

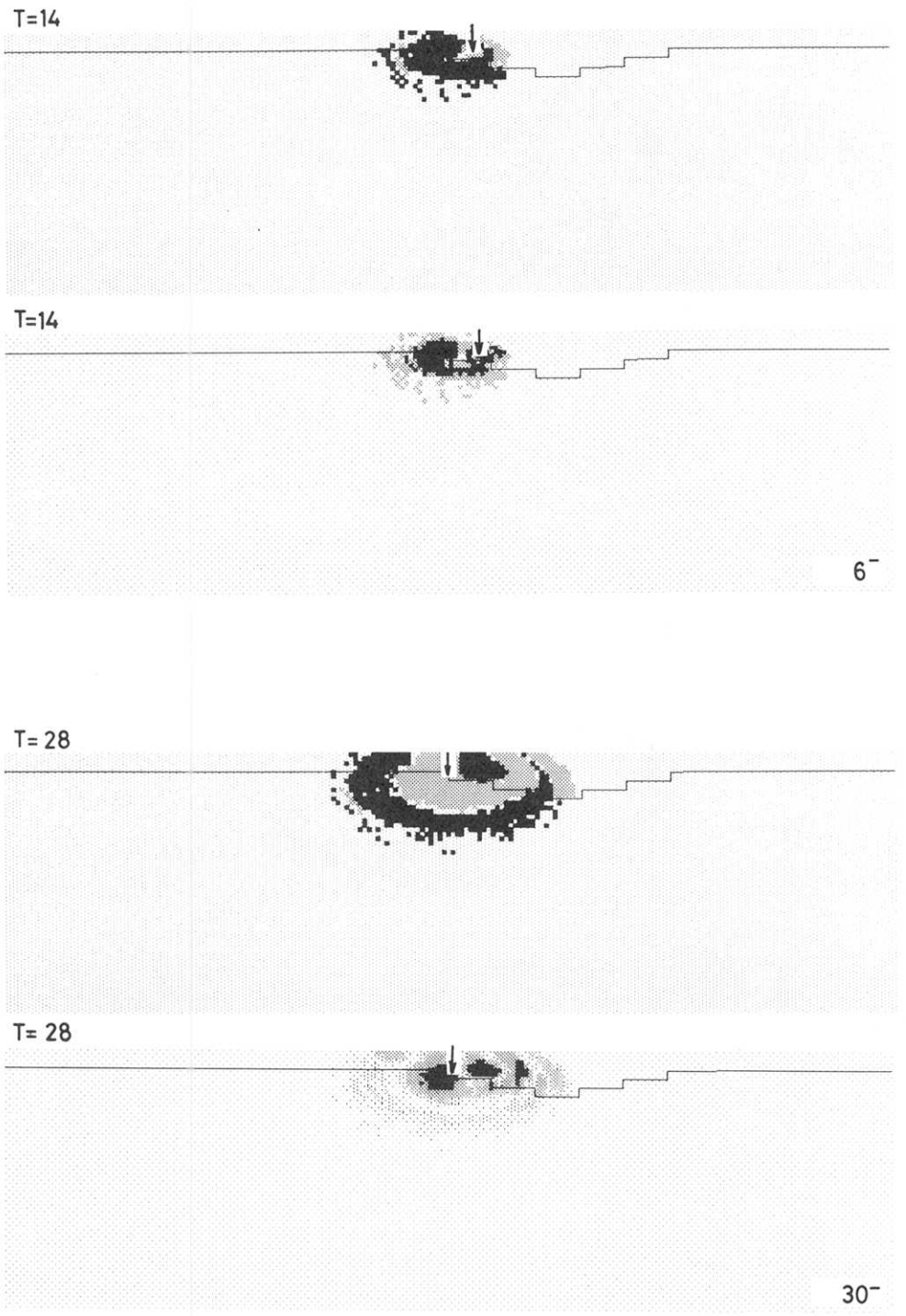

Fig. 23.

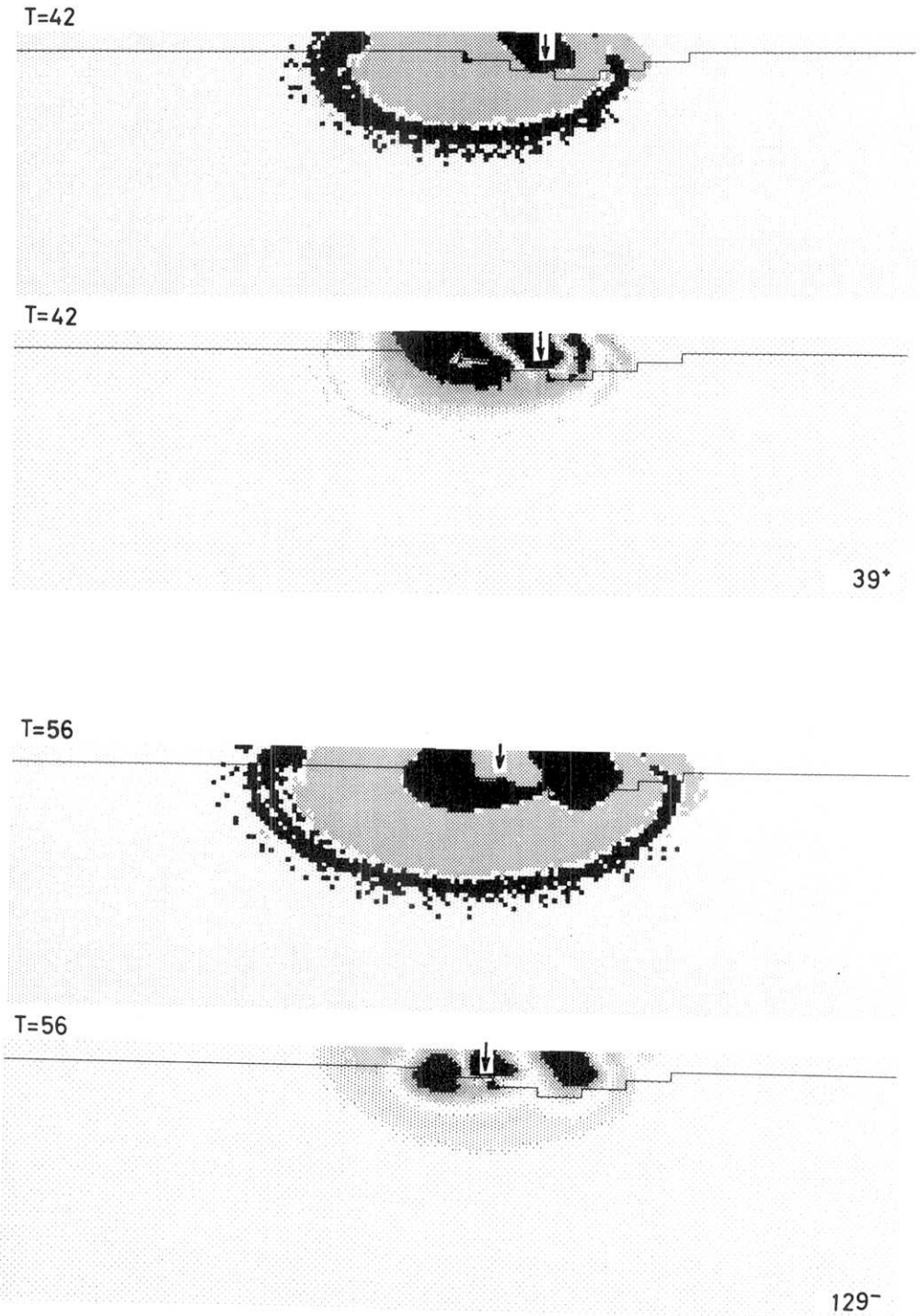

Fig. 23. continued.

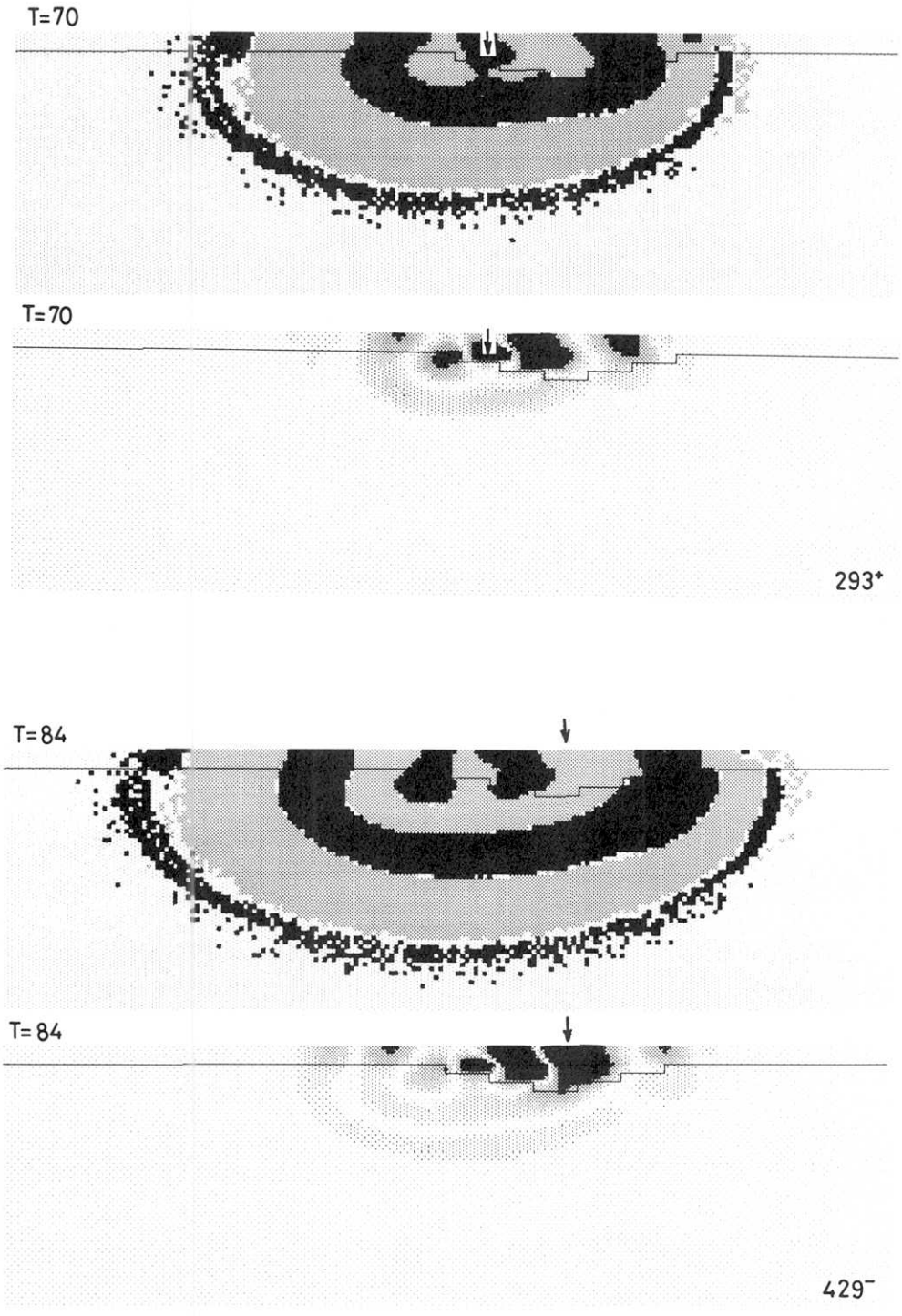

Fig. 23. continued.

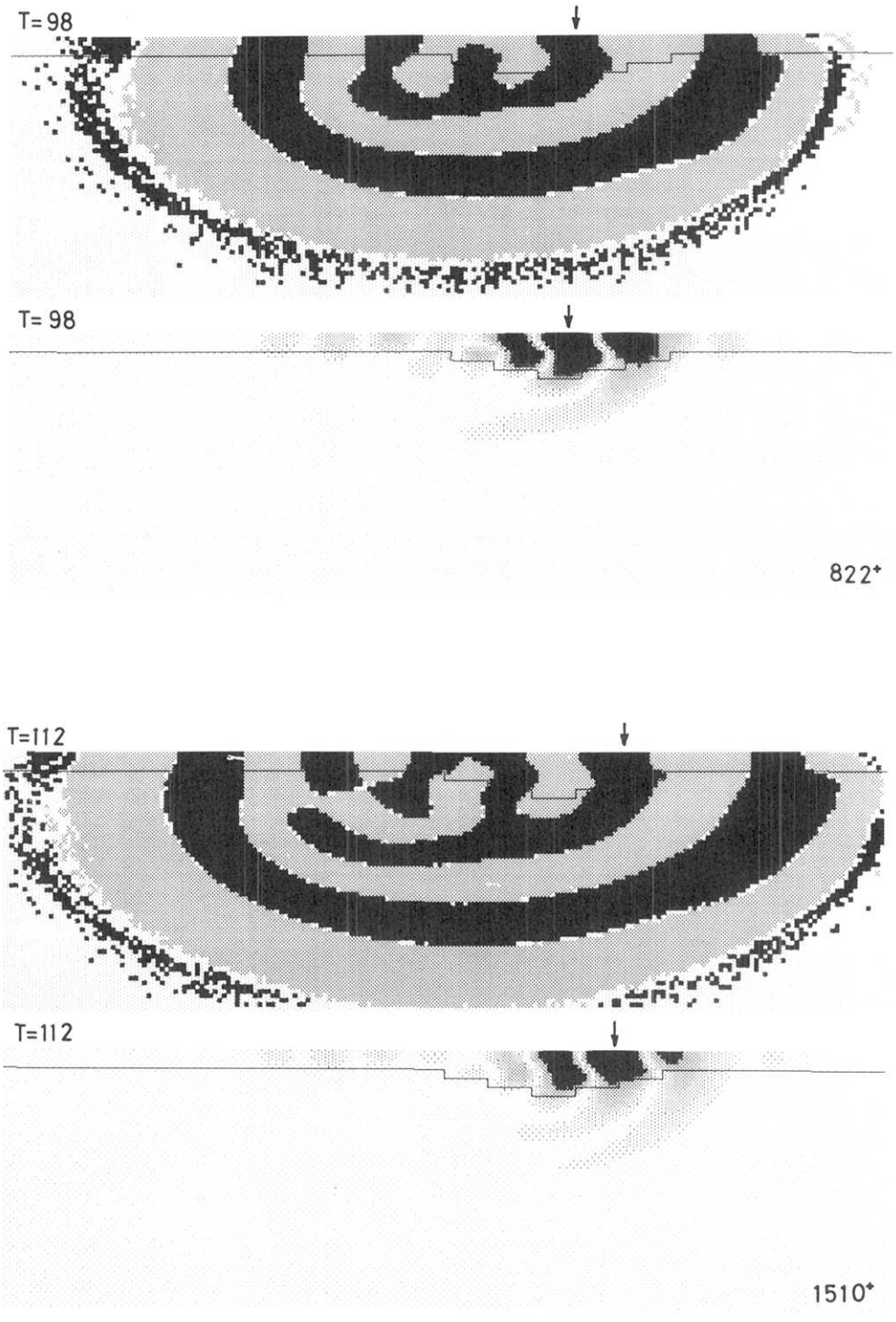

Fig. 23. continued.

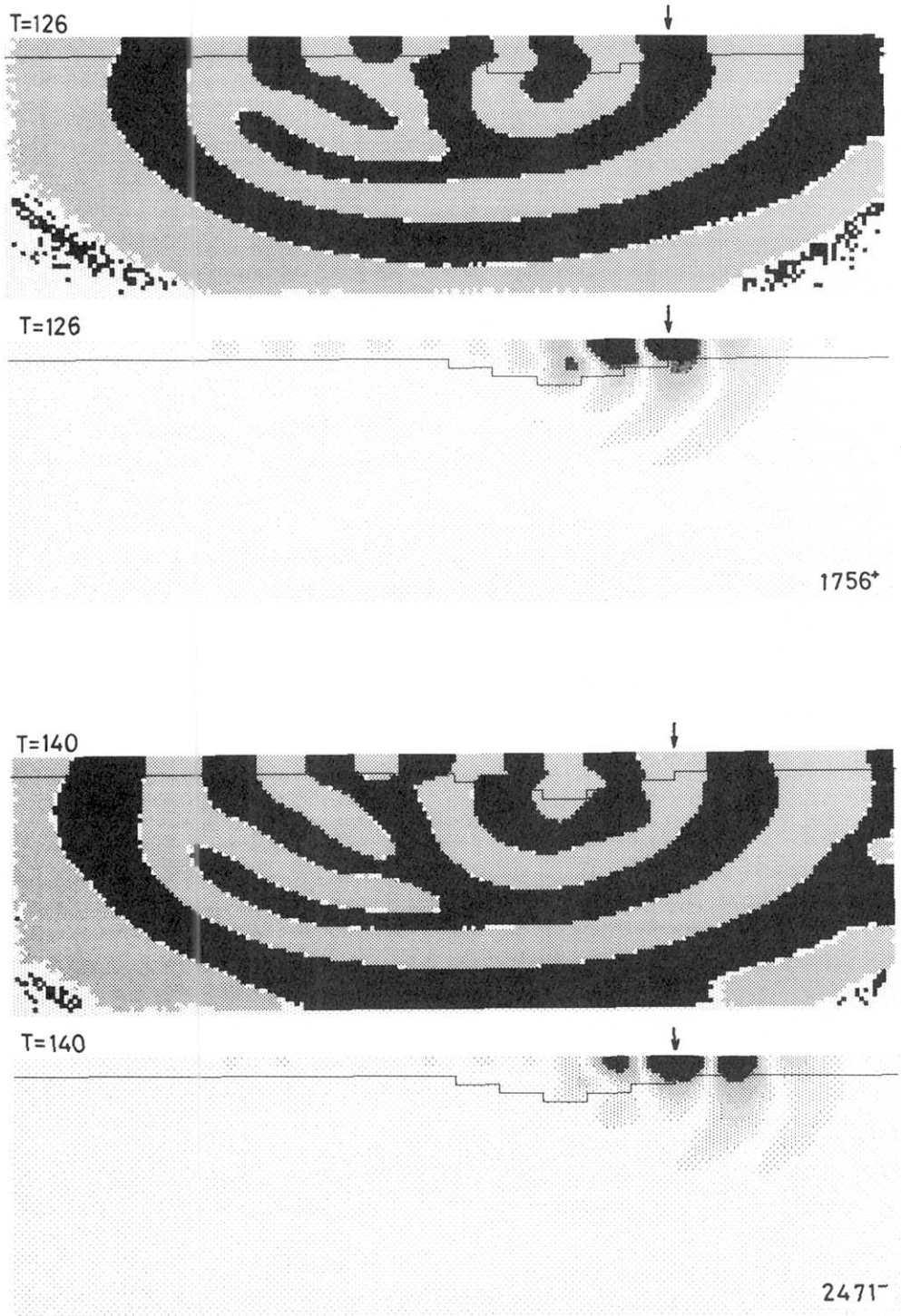

Fig. 23. continued.

wave source is apparently located at the windward first Moho-discontinuity step. The maximum amplitude of the displacement increases with increasing time, 39^+ to 129^- at $T=42$ and 56.

At $T=56$, interference between two clusters of positive phase components of the scattered waves is observed near the first and fourth Moho-discontinuity steps in the phase distribution. Thus, a new scattered wave with a positive component is generated at $T=70$, due to the interference described above. Here, it is noted that the wave source is apparently located at the second Moho-discontinuity step. The snap shots at $T=70$ and 84 show that the energy of the scattered waves is confined mostly to the crust.

At $T=98$, a group of the reflected waves appear in the backward wave trains in the energy distribution. The phase distribution at $T=112$ shows that the phases of the first and second scattered waves, consisting of a pair of positive and negative components, propagate concentrically in the substratum. But the phase of the third scattered waves is turbulent, due to successive interference between multiply-generated scattered waves.

The energy distributions at $T=126$ and 140 show that the reflected waves, shown to the left, gradually disappear from the wave field considered. This might be caused by attenuation of reflected waves due to the lapse of time and also from no new scattered waves being generated, because wave trains with a high level of energy pass the nonuniform wave guide. The fourth scattered wave, generated at the center of the interface, is observed in the phase distribution at $T=140$.

Summarizing the process of generating the scattered waves, examined above, it is understood that due to interference between the "minor scattered waves," which were locally generated at different locations along the concave interface, a "new scattered wave" is generated. In Fig. 24, to clarify the concept of interference between "minor scattered waves," the locations of scatter and the coupling of positive components of particle displacement of scattered waves are shown schematically by clusters of arrows ($S_1, S_2, \cdots, S_6$) and enclosed areas with dots, respectively.

The figure suggests that the second positive component of a new scattered wave arises from interference between "minor scattered waves" due to two scatterings of S_2 and S_3, while the third one is due to three scatterings of S_4, S_5 and S_6. The figure also indicates that the formations of negative components of the first and second scattered waves depend not on only the domains of negative components of the first and second scattered waves, but also on the spatial expansions of the second and third possitive components, respectively.

Thus, it is found visually that the generation of scattered waves is basically based on interference between "minor scattered waves" locally generated at different locations along the concave interface.

3.4 Dispersion of Scattered Waves

By graphically analyzing variations in a set of snap shots, we estimate wavelength, phase velocity and period of the scattered waves.

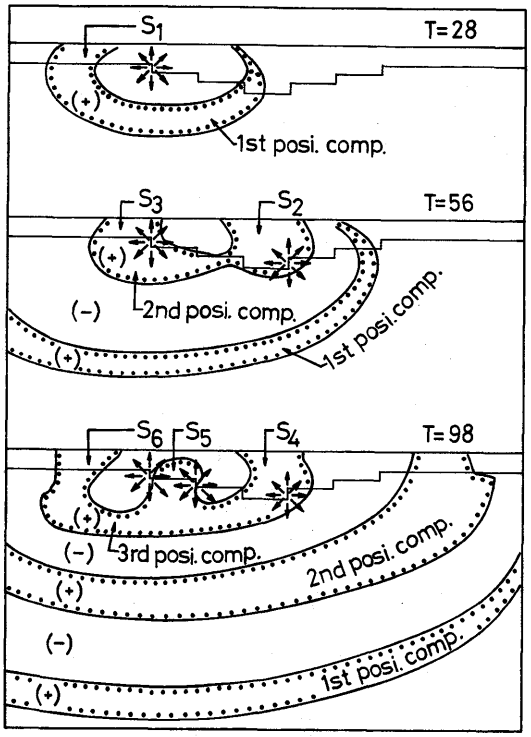

Fig. 24. Brief sketch showing interference between the scattered waves. The positive (+) components of particle displacement of the first (1st), second (2nd) and third (3rd) scattered waves are denoted by enclosed areas with dots, while the negative (−) components by white areas. Clusters with eight arrows ($S_1, S_2, \cdots, S_6$) indicate the locations where the scattering occurred. Note that the interference between the "minor scattered waves," generated at different locations along the interface, successively makes "new scattered waves." This schematic map is drawn based on the snap shots at different instances of times of $T=28$, 56 and 98, in Fig. 23.

The boundary between the positive (P) and negative (M) components of the displacement at $T=84$ is plotted schematically in Fig. 25(b), on the basis of the phase distributions of Fig. 23. The wavelength (λ) of the first scattered wave is shown by an arrow. The wavefront at $T=84$ is tentatively represented by the boundary between the positive and negative components of the first scattered wave. Following the same procedure as those mentioned above, the wave fronts at different times (T) are determined and traced in Fig. 25(a).

3.4.1 Wavelength, Phase Velocity and Period

The wavelength and propagated distance (d) at an interval of 14 s, whose values are read from the phase distributions in Fig. 23, are listed in Table 1. The wavelength of 197.8 km, phase velocity (c) of 4.668 km/s and period (q) of 42.37 s are estimated for the first scattered wave.

The boundary between positive and negative components of the displacement of scattered waves, at $T=112$, is displayed schematically in Fig. 26(b). The wavelength

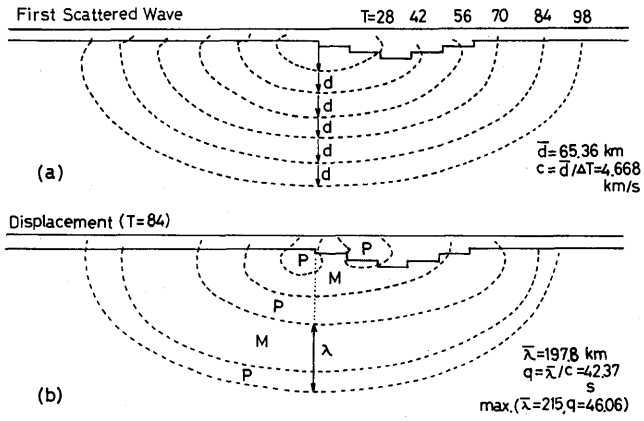

Fig. 25. (a) Schematic diagram showing wave fronts (dotted lines) of the first scattered wave at different times of T. The length (d) with an arrow gives the propagated distance during time interval (ΔT) of 14 s. The phase velocity (c) is calculated from $\bar{d}$ (average of d) and ΔT, and is written at the lower right. (b) Contour plot (dotted lines) of the spatial boundary between the positive (P) and negative (M) components of the displacement, obtained on the basis of phase distribution at $T=84$ in Fig. 23. The wavelength (λ) of the first scattered wave is estimated from the distance given by a bold line with two arrows, involving the positive and negative components of the scattered wave generated first. The period (q) of the first scattered wave is calculated from $\bar{\lambda}$ (average of λ) and the phase velocity c obtained above, and is also written at the lower right. The boundary between the positive and negative components of the first scattered wave at $T=84$ represents the wave front of the first scattered wave at that time in (a).

Table 1. Wavelength (λ) and propagated distance (d) of the first scattered wave. These values are estimated on the basis of the schematic diagram (Fig. 25), which shows the successive wave fronts of the first scattered wave.

First Scattered Wave

Travel Time T (s)	Propagated Distance d (km)	Wavelength λ (km)	Wavelength max. (km)
28	60.2	—	—
42	68.8	—	—
56	60.2	197.8	215.0
70	68.8	197.8	215.0
84	68.8	197.8	215.0
98	—	197.8	215.0
Average	65.36	197.8	215.0

of the second scattered wave is shown by an arrow in the figure. The wave fronts of the second scattered wave are traced at different times in Fig. 26(a).

Following the same procedure as that taken in the first scattered wave, the

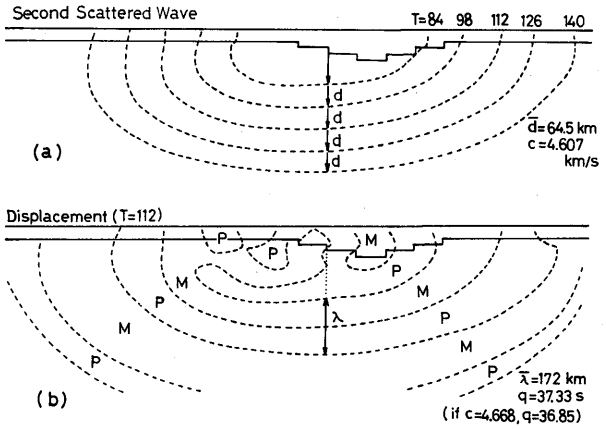

Fig. 26. (a) Schematic diagram of wave fronts (dotted lines) of the second scattered wave at different times of T. For the symbols d, $\bar{d}$, and c see the caption of Fig. 25. (b) Contour plot (dotted lines) of the spatial boundary between the positive (P) and negative (M) components of the displacements, obtained on the basis of the phase distribution at $T=112$ in Fig. 23. For the symbols λ, $\bar{\lambda}$, and q, see the caption of Fig. 25. The second scattered wave signifies the secondary scattered wave generated.

average wavelength and the distance propagated at an interval of 14 s, of the second scattered wave, are estimated as 172.0 km and 64.5 km, respectively (Table 2). The phase velocity is determined to be 4.607 km/s and the period about 37 s. We notice that the wavelength of the second scattered wave is shorter than that of the first ones.

The phase velocities of the scattered waves, obtained above, are shown in Fig. 27, along with the dispersion curves of the fundamental and first higher modes of Love waves calculated for uniform wave guides with crustal thicknesses of $H=35$ and 87.5 km. We notice from the figure that the phase velocities of both first (f) and second

Table 2. Wavelength (λ) and propagated distance (d) of the second scattered wave. These values are estimated on the basis of the schematic diagram (Fig. 26), which shows the successive wave fronts of the second scattered wave.

Second Scattered Wave

Travel Time T (s)	Propagated Distance d (km)	Wavelength λ (km)
84	68.8	172.0
98	60.2	172.0
112	68.8	172.0
126	60.2	172.0
140	—	172.0
Average	64.5	172.0

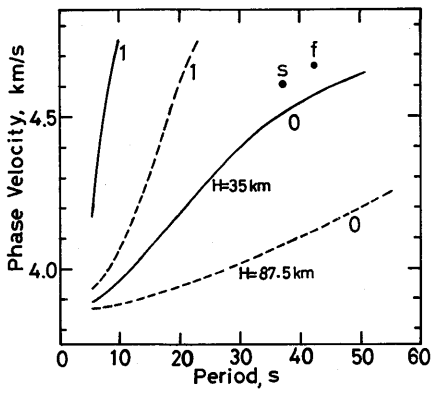

Fig. 27. Phase velocities (solid circles) of the first (f) and second (s) scattered waves. The velocities are determined from the graphical analysis of the snap shots of the scattered waves shown in Figs. 25 and 26. The phase velocity dispersion curves of the fundamental (0) and first higher (1) modes of Love waves, calculated for the uniform wave guides with the crustal thicknesses (H) of 35 (solid lines) and 87.5 (dashed lines) km, are also shown in the figure. The crustal thickness of $H=35$ km corresponds to the shallowest boundary of the concave interface of the Moho discontinuity and that of $H=87.5$ km to the deepest one.

(s) scattered waves are higher, but not so different from, than those of the fundamental mode for the uniform wave guide with a shallow crust of $H=35$ km. This characteristic suggests that the scattered waves possess essentially the dispersive property of incident waves.

The scattered waves might be interpreted as coupled waves of body waves with surface waves, because the dispersed phase velocities were obtained by analyzing scattered waves propagated downwards bound for the bottom of the mantle (Figs. 25 and 26). Conclusively, the phase velocity dispersion of the scattered waves leads to the interpretation that the scattered waves are generated by resonance between the uniform wave guide and the nonuniform wave guide with irregular structures of the Moho discontinuity.

From Fig. 27 we also find that the scattered waves are not contaminated by the first higher modes of Love waves in a period range from 20 to 50 s. At periods shorter than 20 s, the property of the first higher modes for thicker crustal structures might be superimposed on the scattered waves.

3.4.2 Spectra of Scattered Waves

Figure 28(a) shows Fourier spectra of scattered waves calculated on the free surface at different times (T), solid marks pointing the location of peak amplitude. The spectra of the primary waves at $T=70$ are denoted by dashed lines with designations of Pr70, which also represents the spectra of the primary waves at other times (Fig. 28(c)). Two arrows attached to letters f and s indicate the characteristic wavelengths of the first and second scattered waves, previously determined through a graphical analysis of the snap shots.

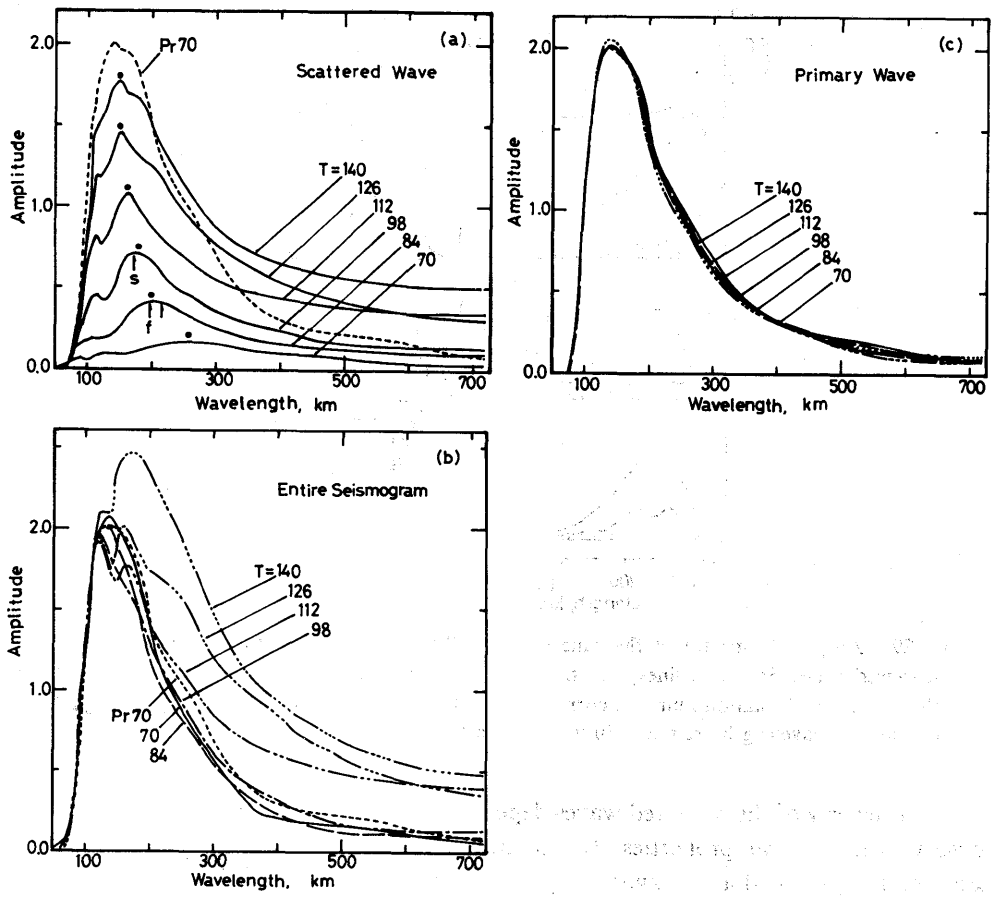

Fig. 28. Amplitude spectra of the free-surface displacements of (a) the scattered waves, (b) the entire seismograms, and (c) the primary waves at various instants in time (T). The spectra of the primary waves at $T=70$ are given by dashed lines with the symbol Pr70 in (a) and (b). In (a), the solid circles indicate the locations of the spectral peaks and the arrows point the wavelengths of the first (f) and second (s) scattered waves, estimated from the graphical analysis. The arrow without the symbol (f) along the spectra at $T=84$ gives the maximum wavelength estimated from the graphical analysis.

The characteristic wavelengths are slightly longer than the predominent wavelength of the primary waves (the incident) waves which show the normal dispersion (Fig. 27). This characteristic might be reasonable because we analyzed scattered waves generated at the early stage of scattering. Up to $T=140$, the wavelengths of scattered waves approach those of primary waves with increasing time (Fig. 28(a)). This tendency also appears in the entire seismograms (Fig. 28(b)). These results suggest that scattered waves mostly show properties similar to those of incident waves (see also Fig. 29), thereby, the entire seismograms, which consist of the primary waves and the scattered waves, also show properties similar to those of the incident waves.

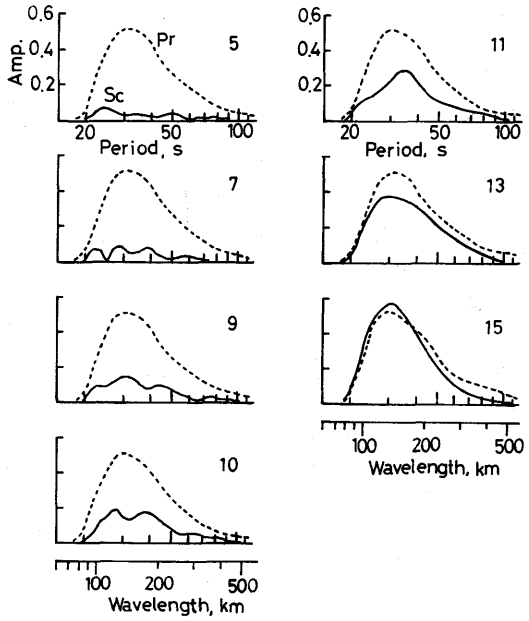

Fig. 29. Amplitude spectra of the time series of the primary waves Pr (dotted lines) and scattered waves Sc (solid lines), on the free surface at several stations. The numerals in the figure denote station numbers corresponding to those in Fig. 6(a). In the abscisa, both period and wavelength are scaled in units of sec and km, respectively.

The energy of the scattered waves depends on the location over the interface. To observe the spectral properties, the scattered waves for different locations were Fourier analyzed and are shown in Fig. 29. The numerals attached to the spectra in the figure denote the site number on the free surface over the interface (Fig. 6(a)). The spectra of scattered waves (Sc) show that (1) the predominent wavelength of about 140 km is close to that of the primary waves (Pr) and this might be interpreted as the resonance wavelength of the interface, and (2) the amplitude is lowest at starting site 5, intermediate at central site 10, and highest at ending site 15. Feature (2) suggests that the energy of the scattered waves generated along the interface is trapped and propagated in the crust towards the propagating direction of the incident waves. Therefore, the energy is maximum at the ending site of the interface.

The time series of the scattered waves (Sc) and the primary waves (Pr) are traced in Fig. 30(a) and those of the entire seismograms (En) and the primary waves (Pr) in Fig. 30(b). The growth of the scattered waves with increasing location number, which was found in the spectra, is clearly observed in the time series of the scattered waves, with a phase lag of about $\pi/2$ against the primary waves. But, the phase lag of the entire seismograms is decreasing compared to that of the scattered waves.

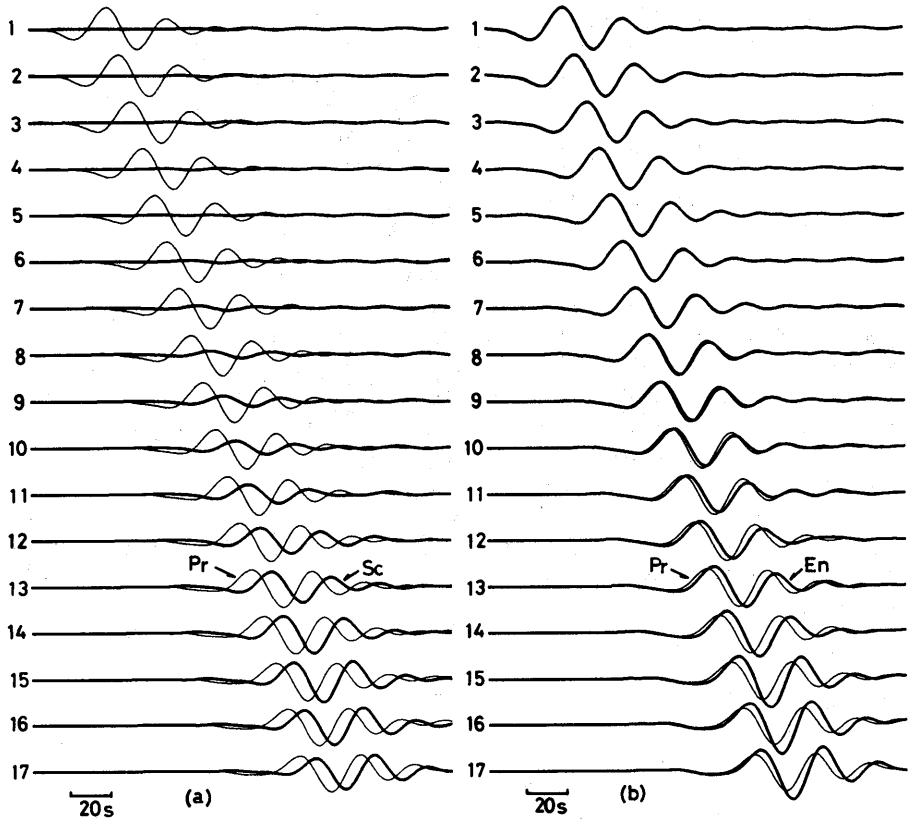

Fig. 30. Time series of (a) scattered waves Sc (bold lines) and primary waves Pr (light lines) and (b) the entire seismograms En (bold lines) and primary waves Pr (light lines). The numerals attached to the wave forms denote station numbers corresponding to those in Fig. 6(a).

3.5 Analogy between Love Waves and Long Waves

It is known that there is an analogy between edge waves along a continental shelf and Love waves in an elastic medium with a low-velocity surface layer (SEZAWA and KANAI, 1939). The scattering of long waves was investigated by MOMOI (1981) using a model of a semi-circular bay which flanks a continental shelf and an open sea of a greater depth.

According to MOMOI (1981), there are two resonances; one is the resonance caused by a coupling between the bay and the shelf (BS-resonance), while the other is related only to the continental shelf (S-resonance). The bay and the shelf in the long-wave propagation correspond, respectively, to the concave Moho-discontinuity and the crust in the Love wave propagation (Fig. 31).

For a small scale of B ($B=b/\omega \leqq 1.0$) (b, ω: width of the shelf and radius of the semi-circular bay), the scattered energy E takes its maximum at

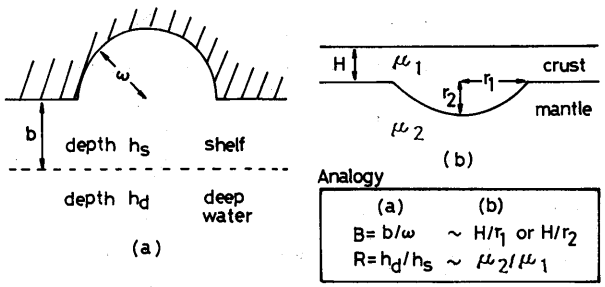

Fig. 31. (a) The model of the semi-circular bay on a continental shelf and open sea with a greater depth, used by MOMOI (1981). The hatched region denotes the coast in the case of edge waves or the free surface in the case of Love waves. (b) Schematic diagram of present model, in which the steps of the Moho discontinuity are approximated by a concave curve. The analogy between model parameters in edge wave and Love wave propagations is written in the squared area below model (b). The definitions of B and R (MOMOI, 1981) are $B=b/\omega$ (b, ω: width of the shelf and radius of the semi-circular bay) and $R=h_d/h_s$ (h_d, h_s: water depths of the deep water and shelf) in (a). The B and R are interpreted in (b) as follows: $B \approx H/r_1$ or H/r_2 (H, r_1 or r_2: crustal thickness and radius of the concave Moho discontinuity) and $R \approx \mu_2/\mu_1$ (μ_2, μ_1: rigidities in the mantle and the crust).

$$kb \approx \pi/2, \tag{3.2}$$

due to S-resonance, and at

$$k(b+\omega) \approx (2n+1)\pi/2, \tag{3.3}$$

due to BS-resonance, in which n and k denote, respectively, an integer and the wave number, and the ratio R ($=h_d/h_s$) (h_d, h_s: water depths of the deep sea and shelf) is arbitrarily fixed.

In the present problem, the ratio R can be roughly interpreted as the ratio of rigidities in the mantle (μ_2) and crust (μ_1). The ratio B ($=H/r_1$, or H/r_2) (H: thickness of the crust; r_1 or $_2$: the radius of the concave Moho-discontinuity) is less than 1.0 ($H/r_1=0.28$; $H/r_2=0.67$) when H, r_1, and r_2 take values of 35, 125, 52.5 km, respectively.

Substituting H into b in Eq. (3.2), the resonance wavelength of 140 km is obtained, while substituting H and r_1 into b and ω in Eq. (3.3), respectively, those of 640, 210 and 128 km are obtained from the first ($n=0$), second ($n=1$), and third ($n=2$) modes, respectively. The latter three wavelengths become slightly smaller when r_2 is substituted into ω in Eq. (3.3).

The concave Moho-discontinuity considered here is regarded approximately as the "Mountain Root Structure." Thereby, we can expect two resonances: one is the "crust-resonance" (C-resonance) while the other is the "crust and mountain resonance" (CM-resonance). The predominant wavelength of 140 km, observed in the amplitude spectra of the scattered waves (Figs. 28 and 29), might be attributed to the C-resonance.

This result suggests that the wavelength of the S-resonce defined by MOMOI (1981) corresponds to the predominent wavelength of the incoming long waves propagated in the continental shelf under the several conditions of B and R adopted above.

The resonance wavelength of 128 km due to the CM-resonance would be incorporated in that of the C-resonance, because they are very close to each other. The wavelengths of 215 and 197 km, determined by the graphical analysis of the snap shots (Tables 1 and 2), might be attributed to that of 210 km due to CM-resonance. If $r_1=r_2$, the wavelength due to CM-resonance would be observed more clearly, approaching a constant value.

3.6 Concluding Remarks of Part 3

The scattered waves, generated due to the lateral heterogeneity of the Moho-discontinuity, were investigated with respect to their generation and propagation, through a graphical analysis of snap shots of the wave field.

The interface connects with the uniform wave guide with a crustal thickness of 35 km and covers an area of maximum horizontal and vertical lengths of 250 km and 52.5 km. It consists of six steps of Moho-discontinuity, which protrudes into the mantle and is regarded as the mountain root structure.

The important results obtained are summarized as follows.

1) The scattered waves spread in all directions, with sources apparently located at the steps of the Moho-discontinuity.

2) The interference between the scattered waves, generated at different steps along the concave interface of the Moho discontinuity, leads to the generation of new scattered waves.

3) The phases of scattered waves vary concentrically in the substratum.

4) The energy of scattered waves is partitioned mostly into the transmitted waves, reflected waves to some extent, and body waves protruding into the half space to a slight degree.

5) Three types of scattered waves with specific wavelengths are coupled in the early stage, but they are distinguished with increasing time.

6) The energy of the reflected waves is mostly confined in the crust while that of the transmitted waves extends to both the crust and the mantle.

7) The amplitude of the displacement of the scattered waves on the free surface is comparable to that of the primary waves when Love waves are travelling over the interface.

8) The predominant wavelengths of the scattered waves, determined by the graphical analysis of the snap shots and Fourier spectra of the scattered waves, agree well with the resonance wavelengths inferred from the scattering theory of long waves of MOMOI (1981).

9) The amplitude spectra of the scattered waves on the free surface are maximum at a dominant wavelength of 140 km. The wavelength is consistent with the characteristic wavelength of the primary waves, and it also agrees with that obtained

from the crust-resonance (C-resonance), corresponding to the continental shelf-resonance (S-resonance).

10) The wavelengths of 215 km or 197 km of the scattered waves which were generated at the early stage of the scattering, determined from the snap shots, are very close to that of 210 km obtained from the crust and mountain resonance (CM-resonance), corresponding to the bay and shelf resonance (BS-resonance).

Part 4

Multiple Reflection, Transmission and Diffraction of Love Waves across Irregular Structures of the Moho Discontinuity

4.1 Introduction

In Part 3, the generating mechanism and dispersive properties of scattered waves due to Love wave propagation in irregular structures are discussed. It is understood from the study that Love waves show anomalous phase velocities if the scattered waves extracted in Fig. 23 would be superimposed on the incident Love waves.

However, it is as yet unresolved how much of the energy of the scattered waves is partitioned into transmitted waves, reflected waves and body waves (shear waves). To solve the problem it is useful to estimate the location-dependent transmission and reflection coefficients of Love waves across the interface. In this problem we apply the theory of ALSOP (1966) and develop a theoretical approach to the welded boundaries.

In this chapter, the terms "scattered waves" and "diffracted waves" are frequently used. The scattered waves are defined in Part 3. To distinguish the diffracted waves from scattered waves, we define the diffracted waves as creeping waves that propagate along the irregular surface or nonhorizontal layer boundaries, as used by KAWASE (1988).

4.2 Method

According to ALSOP (1966), the reflection and transmission coefficients of Love waves incident on a vertical interface are determined as follows.

If we assume the form of the eigenfunction in medium l in the Cartesian coordinate (Fig. 32) as

$$\Phi_p^l = A_p^l \phi_p^l \exp\{i(+k_p^l x - \omega t)\} y \tag{4.1}$$

where the ϕ_p^l are functions of z determined by the shear velocity and density distributions within the medium l. k_p^l is the appropriate wave number of the pth mode in medium l, A_p^l is an arbitrary constant, ω is the angular frequency of the incident wave, y is an unit vector in the y direction, and t is the time determined from an arbitrary origin. The sign of k_p^l determines the direction of propagation. In the following, the fundamental mode Love waves are assumed to be incident upon the media (see Fig. 32), as was also assumed in the numerical simulations carried out in Parts 1, 2 and 3.

The boundary condition of the continuity of displacement across the welded boundary between the two layered quarter-spaces is written as

$$\phi_1^1 + \sum_{i=1}^{n} a_i \phi_i^1 = \sum_{j=1}^{m} b_j \phi_j^2 \tag{4.2}$$

where the a_i are the reflection coefficients and the b_j are transmission coefficients. In this formulation the body wave contribution is ignored.

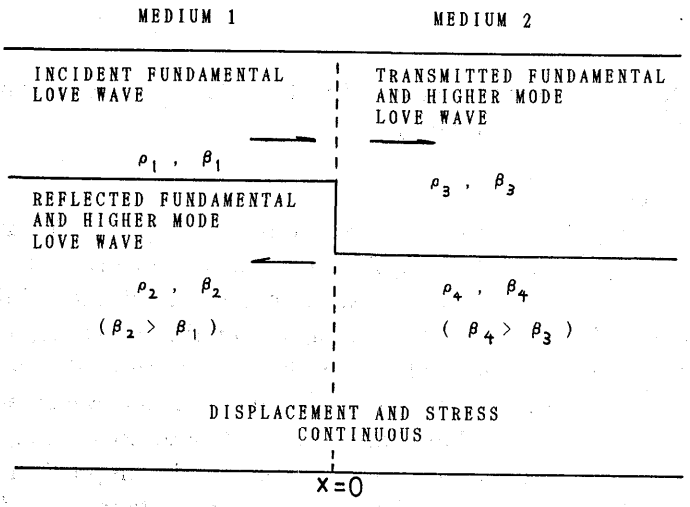

Fig. 32. Schematic diagram illustrating the problem of Love waves propagating across a Moho discontinuity step. Densities and S-wave velocities with suffixes from 1 to 4 are denoted by ρ and β. In the present problem the vertical step exists along the z-axis (dashed line) and the elastic parameters for upper or lower two quarter-spaces have the same values for Medium 1 and Medium 2.

The boundary condition of the continuity of stresses at the welded boundary between the quarter spaces is given by

$$\mu_1 k_i^1 \phi_1^1 - \mu_1 \sum_{i=1}^{n} a_i k_i^1 \phi_i^1 = \mu_2 \sum_{j=1}^{m} b_j k_j^2 \phi_j^2 \tag{4.3}$$

where μ_1 and μ_2, respectively, represent the rigidities on the left and right sides of the discontinuity, which are functions of z. Multiplying both sides of Eq. (4.3) by μ_2 and by virtue of the orthogonality relation of the eigenfunctions (HERREA, 1964), which is defined as

$$k_i \int_0^\infty \mu_i(z)\phi_i(z)\phi_j(z)dz = \delta_{ij} \tag{4.4}$$

the b_j's is expressed in terms of the a_i's as follows.

$$b_j = P_{ij} - \sum_{i=1}^{n} a_i P_{ij} \tag{4.5}$$

where the coupling coefficient P_{ij} is defined as

$$P_{ij} = k_i^1 \int_0^\infty \mu_1(z)\phi_j^2(z)\phi_i^1(z)dz\,. \tag{4.6}$$

The reflection coefficients obtained by a variational method using Eq. (4.2), are given by

$$\sum_{r=1}^{n} a_r\left(S_{ir}+\sum_{j=1}^{m}(P_{rj}T_{ij}+P_{ij}T_{rj})+\sum_{j=1}^{m}\sum_{s=1}^{m}P_{ij}P_{rs}V_{js}\right)$$

$$=-\left(S_{1i}+\sum_{j=1}^{m}(P_{ij}T_{1j}+P_{1j}T_{ij})-\sum_{j=1}^{m}\sum_{s=1}^{m}P_{ij}P_{1s}V_{js}\right) \qquad (4.7)$$

with i equal to $1, \cdots, n$. S_{ij}, T_{ij} and V_{ij} are defined as

$$S_{ij}=\int_0^\infty \phi_i^1\phi_j^1 dz$$

$$T_{ij}=\int_0^\infty \phi_j^1\phi_j^2 dz \qquad (4.7)'$$

$$V_{ij}=\int_0^\infty \phi_i^2\phi_j^2 dz$$

using Eqs. (4.5) and (4.7). We compute transmission and reflection coefficients for periods longer than 20 s, where the fundamental mode of Love waves dominates and the first higher mode is negligible. Because for those periods, mode conversion from the fundamental to first higher modes is impossible due to large differences in phase velocities between the two modes (see Fig. 27).

4.3 Moho Discontinuity Step

In Part 1, the transmission coefficients for a vertical interface of the Moho discontinuity (Model C) were calculated using synthetic seismograms, which include all of the scattered waves. Figure 33 shows transmission coefficients computed from Eq. (4.5). We notice from the figure that in the case of downdip propagation the difference between them is small. Namely, the transmission coefficients (solid circles) obtained from synthetic seismograms and those from solutions (solid lines) of Eq. (4.5) are almost equal to 1.0. On the contrary, in updip propagation the difference is remarkable.

The above difference is physically interpreted such that the conversion of Love waves into body waves is more significant at a step of the Moho discontinuity in updip propagation than in downdip propagation, because shear waves are, as is investigated later in this chapter, radiated in a great deal in updip propagation, especially at longer periods (see Fig. 40).

The concave interface of the mountain root structure consists of three pairs of vertical steps with different crustal thicknesses. For each step of the interface, the transmission and reflection coefficients are computed using Eqs. (4.5) and (4.7), assuming that the medium has one vertial discontinuity, and are shown in Fig. 34. The transmission coefficients designated as u1 and d1 in the figure correspond to those in Fig. 33, in which the crustal thickness of the thinner side (H1) is 35 km and that of the thicker side (H2) 52.5 km. The notations of d1, d2, d3 and u1, u2, u3 mean that the symbols of d and u correspond respectively to downdip and updip propagations, the second symbols of 1, 2, 3 designate the modes of different steps.

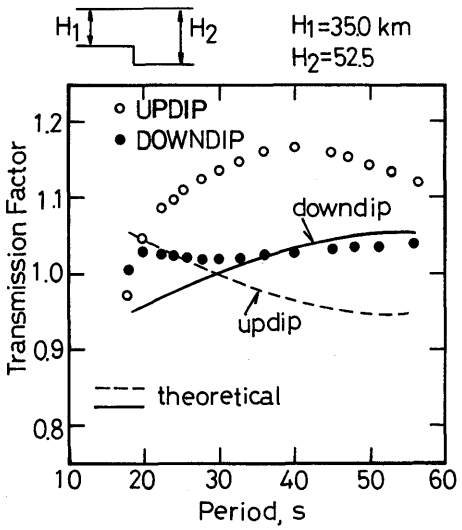

Fig. 33. Transmission coefficients calculated for the medium with the Moho discontinuity step given at the top of the figure. H1 and H2 denote crustal thickness, the ratio of H1 to H2 (α=H1/H2) being 0.67. Open and solid circles indicate the transmission coefficients for updip and downdip propagations, calculated using synthetic seismograms. Solid and dashed lines respectively give the transmission coefficients for downdip and updip propagations, determined from the theory of ALSOP (1966).

From the figure we can see that the reflection coefficients for downdip propagation are positive and decrease from about 0.1 at 20 s to 0.0 at 50 s, while those for updip propagation are negative and vary from about -0.1 at 20 s to -0.02 at 50 s. These trends are not so different for any depth ratio of the thinner to thicker crustal thicknesses (α=H1/H2; α=0.67 (=35/52.5); 0.75 (=52.5/70); 0.8 (=70/87.5)). The period dependence of the transmission coefficients is the inverse of that of the reflection coefficients.

Transmission coefficients vary by several percent in a period range from 20 to 50 s, although period dependence is reversed between for downdip and updip propagations.

The concave interface of the Moho discontinuity, as shown in Fig. 6(a), has crustal thicknesses of 35.0 and 87.5 km at the edges and the central part of the interface, respectively. To estimate the probable upper limits of the reflection and transmission coefficients for the concave interface, we assume a medium in which the maximium irregular variation of the Moho discontinuity is represented by one step, the crustal thickness having two extreme values mentioned above (α=0.4). Using Eqs. (4.7) and (4.5), the reflection and transmission coefficients are calculated for this wave guide, and are shown in Fig. 35. On the whole, the reflection coefficients have at least twice the amplitudes at respective periods, compared to those for the previous cases of (d1, u1), (d2, u2) and (d3, u3). It is noted that the general patterns of reflection coefficients for H1=35 and H2=87.5 km are similar to the previous cases,

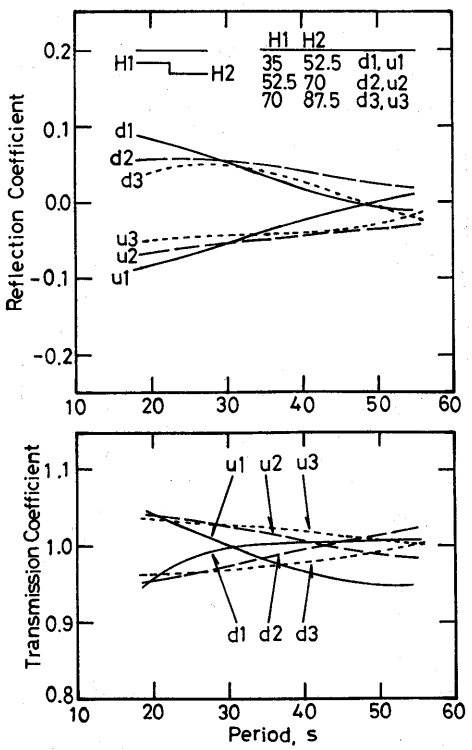

Fig. 34. Reflection and transmission coefficients calculated for the medium with the Moho discontinuity step shown at the upper left of the figure. The reflection and transmission coefficients for downdip propagation for three combinations of crustal thicknesses of H1 and H2 are designated as d1, d2 and d3. Similarly, the reflection and transmission coefficients for the updip propagation are designated as u1, u2 and u3. The ratios of H1 to H2 (α=H1/H2) are 0.67 (H1=35.0 km; H2=52.5 km), 0.75 (H1=52.5; H2=70.0) and 0.80 (H1=70; H2=87.5). The reflection and transmission coefficients are computed from Eqs. (4.7) and (4.5) in the text.

especially to those for H1=35 and H2=52.5 km.

The transmission coefficients for α=0.4, whose characteristics are similar to those for α=0.67, 0.75 and 0.8, indicate maximum variations of about ten percent from 1.0 in the period range 20–50 s. These variations are about twice those for other cases. Thus, we can see from Figs. 34 and 35 that the larger the impedence contrast between the two layered quarter spaces is, the greater are the period dependences of both the transmission and reflection coefficients.

The transmission and reflection coefficients for different H1 and H2 obtained above were estimated for media with relatively long horizontal distances. These estimations are physically very important if we recollect the results found in Parts 1 and 2. In Part 1, the average phase velocities over the concave interface are explained by synthetic layer patameters using the "weighting coefficients" defined in Eqs. (1.21), (1.22), (1.23) and (1.24), in which the coefficients were obtained by dividing the

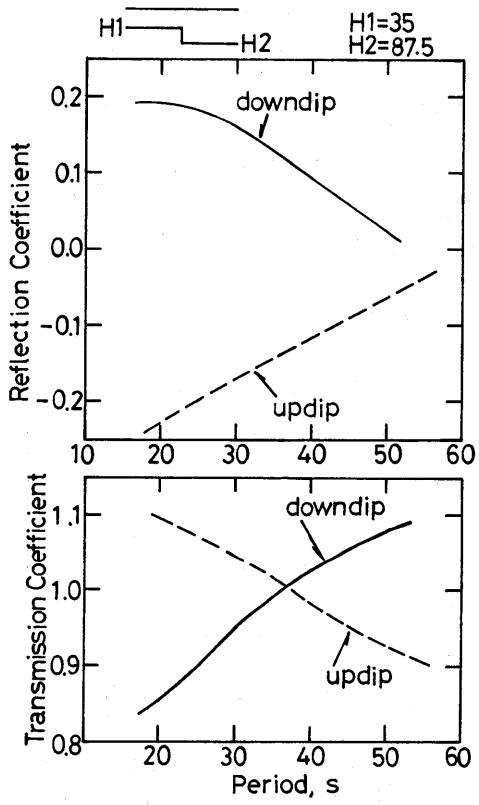

Fig. 35. Reflection and transmission coefficients calculated for the medium with the Moho discontinuity step shown at the top of the figure. The ratio of the crustal thickness of H1 to H2 (α=H1/H2) is 0.4. The reflection and transmission coefficients are computed from Eqs. (4.7) and (4.5) in the text.

entire region of the concave interface into several horizontally layered subregions (Figs. 7(a), (b), (d), (e)). In Part 2, the phase velocities for the narror ranges in downdip and updip propagations decreased in proportion to the area including the crust (Fig. 21). These results suggest that in irregular structures waves propagate gradually varying normal mode solutions for horizontal layers with relatively short lengths. The transmission and reflection coefficients computed for different H1 and H2, given in Figs. 34 and 35, are employed in the next section.

4.4 Multiple Reflection

In Fig. 36, the transmission coefficients just above the concave interface, obtained in Part 1, are shown along with the several transmission coefficients for the medium with a vertical discontinuity, obtained on the basis of Eqs. (4.2), (4.3) and (4.4). It is obvious from the figure that all the transmission coefficients at sites 5, 10 and 15, corresponding to windward, midpoint and leeward sides above the interface, are drastically different from those for the media of α=0.67, 0.75 and 0.8. These

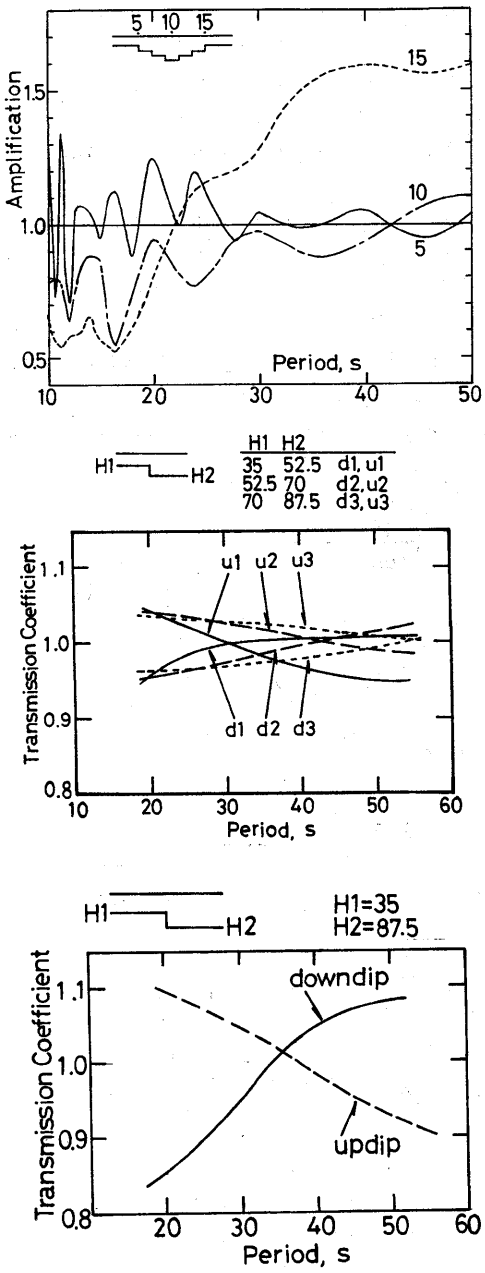

Fig. 36. Comparison of transmission coefficients. Top: Transmission coefficients at the sites 5, 10 and 15 above the concave interface, obtained from synthetic seismograms. The figure is reproduced from Fig. 8. Middle: Transmission coefficients for updip (u1, u2, u3) and downdip (d1, d2, d3) propagations, calculated for the medium with the Moho discontinuity step of $\alpha=0.67$, 0.75 and 0.80. Bottom: Transmission coefficients calculated for the medium with the Moho discontinuity step of $\alpha=0.4$. The figure is taken from Fig. 35.

characteristics are natural, taking into consideration the fact that Love waves inside the concave structure receive interference from the scattered waves generated at the irregular layer boundaries and also from the diffracted waves propagated along the concave interface. Thereby, transmission coefficients above the interface might be interpreted by none of them for the media with a single vertical discontinuity, if the scattering is very strong.

However, we can see a very interesting characteristic in that the transmission coefficients at site 10 form, on the whole, a very similar trend to those for downdip propagation for the medium with a step of $\alpha=0.4$. This phenomenon might be interpreted from Fig. 37 as follows. The left side of the concave structure (a) is approximated by the model (b) with a sloping layer, because reflection from the right side of the interface is weak in the period range 20–50 s (the reflection coefficients for the cases of u1, u2 and u3 are less than 0.1 (Fig. 34)) and the vertical extent of each

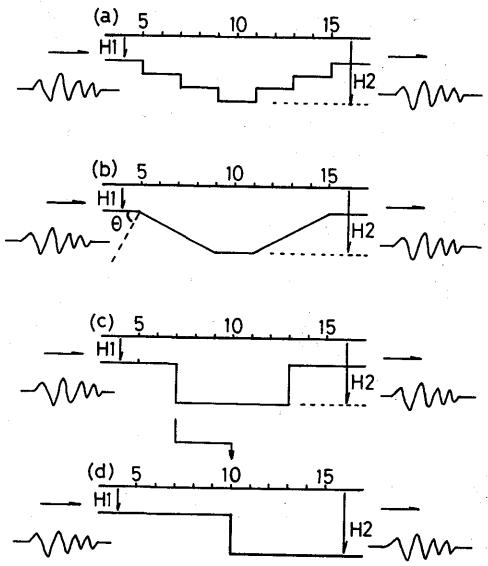

Fig. 37. Illustration of medium model. model (a) The concave interface with several steps of the Moho discontinuity. model (b) A simplified model in which the sloping steps at the left side of the model (a) are replaced by an oblique line. model (c) A simplified model in which the sloping line in model (b) is replaced by a vertical line. model (d) The model with a step which corresponds to the one near the region of site 5 in model (c). H1 and H2 are the shallowest and deepest crustal thicknesses of the concave interface. The angle of incidence ($\theta=62°$) of plane Love waves corresponds to the dip angle of the Moho discontinuity ($\theta_3=28°$) in Fig. 6(d). In so far as the direction of Love wave propagation is from left to right, the transmission coefficients at site 10 in model (a) are approximately equivalent to those at site 10 in model (d).

step forming the slope of the interface is very small compared to the wavelengths of the incident waves. Model (b), furthermore, will be simplified to model (c), because for downdip propagation, the transmission coefficients of Love waves whose angle of incidence (θ) at sloping boundaries in model (b) is 62° are almost equal to those of model (c). This transformation from models (b) to (c) is easily understood from the study of GREGERSEN and ALSOP (1974). They showed that for downdip propagation the transmission coefficients are almost constant in the range of incidence 0°–80°. ITS and YANOVSKAYA (1983) and ITS (1989) reported the same results for media with inclined contacts and they also showed small variations of reflection coefficients for downdip propagation. In model (c), the transmission coefficients at the midpoint (the site 10) of the concave interface are almost identical to that at the windward edge (the site 5), because the effects of the phase delay on the transmission coefficients due to the propagation distance are small. Namely, model (c) is transformed into model (d).

Thus, as far as the propagation mode is confined to downdip propagation, as it is treated here for a concave structure, the transmission coefficients at site 10 obtained from synthetic seismograms (Fig. 36) are approximately explained by those for downdip propagation with medium $\alpha=0.4$ (Fig. 35). The above discussions are not applicable to the transmission coefficients for updip propagation because the coefficients depend greatly on the angle of incidence (GREGERSON and ALSOP, 1974) for that propagation mode.

However, to accurately estimate the transmission coefficients for a concave structure we have to take into consideration the effects of interference between transmitted and reflected waves inside the concave interface. Namely, the problem of multiple reflections of Love waves in the medium with many irregular boundaries must be studied.

At this point, we determine the transmission coefficients at typical sites of sites 5, 10 and 15 above the interface, taking the multiple reflections of Love waves into consideration. In the following, A_0 is an arbitrary constant and k_0 is the wave number in medium number 0 (see Fig. 38). Assuming the incident wave at the windward edge, on the free surface, in the following form similar to Eq. (4.1),

$$v_0(t)=A_0\exp[ik_0x-iwt] \tag{4.8}$$

then, the transmitted waves at the site 5 will be expressed as

$$v_5(t)=v^{\mathrm{I}}(t)+v^{\mathrm{II}}(t)+v^{\mathrm{III}}(t)+v^{\mathrm{IV}}(t)+v^{\mathrm{V}}(t)+v^{\mathrm{VI}}(t) \tag{4.9}$$

where

$$\begin{aligned}
v^{\mathrm{I}}(t) &= A_0b_{01}\exp[ik_1x-i\omega t]\,,\\
v^{\mathrm{II}}(t) &= A_0b_{01}a_{12}a_{10}\exp[ik_1x+ik_12H-i\omega t]\,,\\
v^{\mathrm{III}}(t) &= v_b^{\mathrm{III}}(t)\\
&= A_0b_{01}b_{12}a_{23}b_{21}a_{10}\exp[ik_1x+ik_12H+ik_22H-i\omega t]\,,\\
v^{\mathrm{IV}}(t) &= v_c^{\mathrm{IV}}(t)\\
&= A_0b_{01}b_{12}b_{23}a_{34}b_{32}b_{21}a_{10}\exp[ik_1x+ik_12H+ik_22H+ik_32H-i\omega t]\,,
\end{aligned}$$

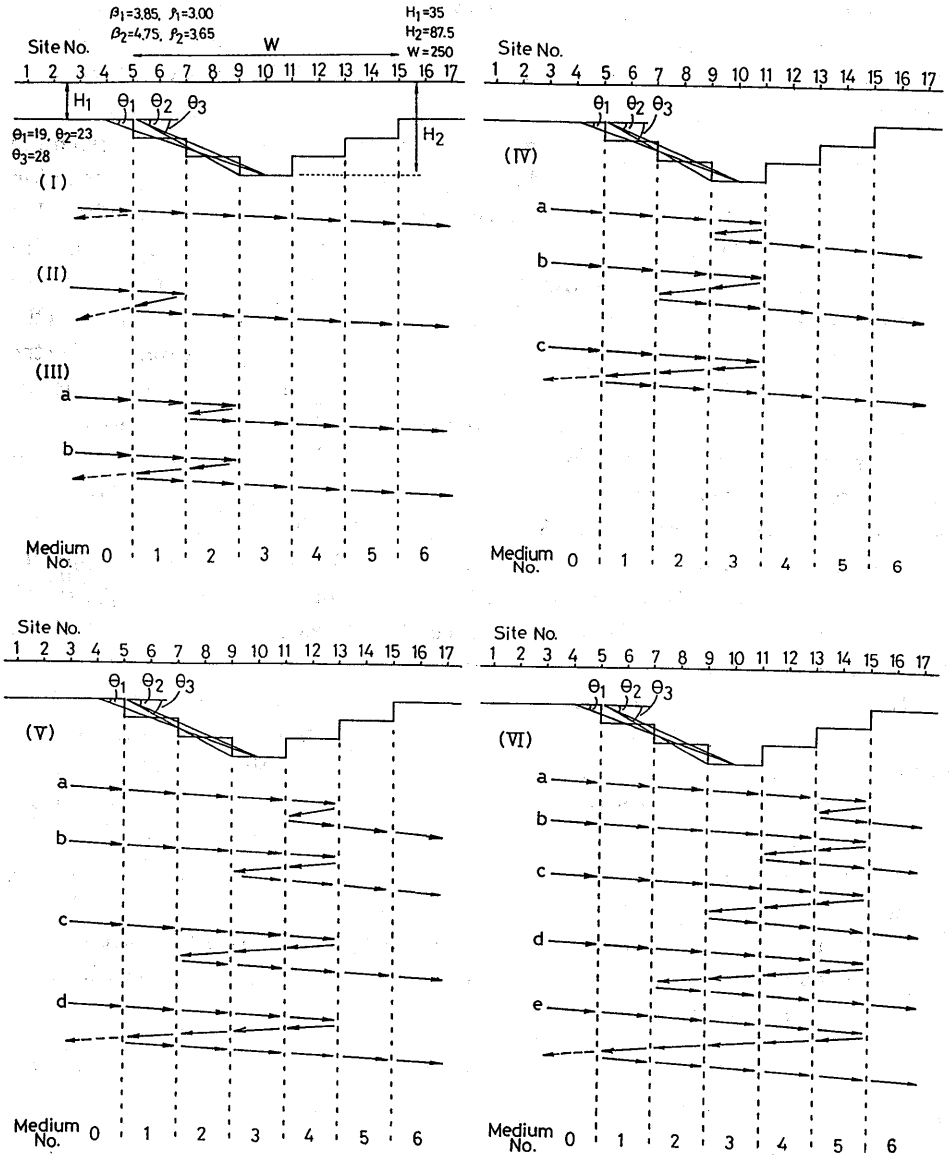

Fig. 38. Illustration of propagations of transmitted and reflected waves (solid or dashed lines with arrows) in which multiple reflections are taken into consideration inside the concave interface. In this figure multiple reflections of more than three reflections are neglected. Numerals on the free surface are site numbers, while those at the bottom are medium numbers. The dashed lines are plotted vertically at the locations of the Moho discontinuity step. The crustal thickness (H1, H2) and the horizontal length (W) of the concave interface are given in km. Shear velocities and densities are denoted by (β_1, β_2) and (ρ_1 and ρ_2) in units of km/s and g/cm^3, respectively. Suffixes 1 and 2 correspond to the crust and the mantle. The slope angle of the concave interface is given by θ_1, θ_2 or θ_3 in degree.

$$
\begin{aligned}
v^{\mathrm{V}}(t) &= v_d^{\mathrm{V}}(t) \\
&= A_0 b_{01} b_{12} b_{23} b_{34} a_{45} b_{43} b_{32} b_{21} a_{10} \exp[ik_1 x + ik_1 2H + ik_2 2H + ik_3 2H \\
&\quad + ik_4 2H - i\omega t], \\
v^{\mathrm{VI}}(t) &= v_e^{\mathrm{VI}}(t) \\
&= A_0 b_{01} b_{12} b_{23} b_{34} b_{45} a_{56} b_{54} b_{43} b_{32} b_{21} a_{10} \exp[ik_1 x + ik_1 2H + ik_2 2H + ik_3 2H \\
&\quad + ik_4 2H + ik_5 2H - i\omega t]. \qquad (4.10)
\end{aligned}
$$

The superscripts of I, II, $\cdots$ and VI correspond to the propagation modes described in Fig. 38. The symbol b_{01} is interpreted as the transmission coefficient of Love waves propagating from media 0 to 1, which are denoted at the bottom of Fig. 38. The symbols a_{12} is interpreted as the reflection coefficient from media 1 to 2. H is the distance between successive steps.

The transmitted waves at the site 10 will be expressed as

$$
v_{10}(t) = v^{\mathrm{I}}(t) + v^{\mathrm{II}}(t) + v^{\mathrm{III}}(t) + v^{\mathrm{IV}}(t) + v^{\mathrm{V}}(t) + v^{\mathrm{VI}}(t) \qquad (4.11)
$$

where

$$
\begin{aligned}
v^{\mathrm{I}}(t) &= A_0 b_{01} b_{12} b_{23} \exp[ik_1 H + ik_2 H + ik_3 (x - 2H) - i\omega t], \\
v^{\mathrm{II}}(t) &= A_0 b_{01} a_{12} a_{10} b_{12} b_{23} \exp[ik_1 3H + ik_2 H + ik_3 (x - 2H) - i\omega t], \\
v^{\mathrm{III}}(t) &= v_a^{\mathrm{III}}(t) + v_b^{\mathrm{III}}(t), \\
v_a^{\mathrm{III}}(t) &= A_0 b_{01} b_{12} a_{23} a_{21} b_{23} \exp[ik_1 H + ik_2 3H + ik_3 (x - 2H) - i\omega t], \\
v_b^{\mathrm{III}}(t) &= A_0 b_{01} b_{12} a_{23} b_{21} a_{10} b_{12} b_{23} \exp[ik_1 3H + ik_2 3H + ik_3 (x - 2H) - i\omega t], \\
v^{\mathrm{IV}}(t) &= v_a^{\mathrm{IV}}(t) + v_b^{\mathrm{IV}}(t) + v_c^{\mathrm{IV}}(\mathrm{t}), \\
v_a^{\mathrm{IV}}(t) &= A_0 b_{01} b_{12} b_{23} a_{34} a_{32} \exp[ik_1 H + ik_2 H + ik_3 2H + ik_3 (x - 2H) - i\omega t], \\
v_b^{\mathrm{IV}}(t) &= A_0 b_{01} b_{12} b_{23} a_{34} b_{32} a_{21} b_{23} \exp[ik_1 H + ik_2 3H + ik_3 2H + ik_3 (x - 2H) - i\omega t], \\
v_c^{\mathrm{IV}}(t) &= A_0 b_{01} b_{12} b_{23} a_{34} b_{32} b_{21} a_{10} b_{12} b_{23} \exp[ik_1 3H + ik_2 3H + ik_3 2H \\
&\quad + ik_3 (x - 2H) - i\omega t], \\
v^{\mathrm{V}}(t) &= v_b^{\mathrm{V}}(t) + v_c^{\mathrm{V}}(t) + v_d^{\mathrm{V}}(t), \\
v_b^{\mathrm{V}}(t) &= A_0 b_{01} b_{12} b_{23} b_{34} a_{45} b_{43} a_{32} \exp[ik_1 H + ik_2 H + ik_3 2H + ik_4 2H \\
&\quad + ik_3 (x - 2H) - i\omega t], \\
v_c^{\mathrm{V}}(t) &= A_0 b_{01} b_{12} b_{23} b_{34} a_{45} b_{43} b_{32} a_{21} b_{23} \exp[ik_1 H + ik_2 3H + ik_3 2H + ik_4 2H \\
&\quad + ik_3 (x - 2H) - i\omega t], \\
v_d^{\mathrm{V}}(t) &= A_0 b_{01} b_{12} b_{23} b_{34} a_{45} b_{43} b_{32} b_{21} a_{10} b_{12} b_{23} \exp[ik_1 3H + ik_2 3H + ik_3 2H + ik_4 2H \\
&\quad + ik_3 (x - 2H) - i\omega t], \\
v^{\mathrm{VI}}(t) &= v_c^{\mathrm{VI}}(t) + v_d^{\mathrm{VI}}(t) + v_e^{\mathrm{VI}}(t), \\
v_c^{\mathrm{VI}}(t) &= A_0 b_{01} b_{12} b_{23} b_{34} b_{45} a_{56} b_{54} b_{43} a_{32} \exp[ik_1 H + ik_2 H + ik_3 2\mathrm{H} + \mathrm{ik}_4 2H + ik_5 2H \\
&\quad + ik_3 (x - 2H) - i\omega t], \\
v_d^{\mathrm{VI}}(t) &= A_0 b_{01} b_{12} b_{23} b_{34} b_{45} a_{56} b_{54} b_{43} b_{32} a_{21} b_{23} \exp[ik_1 H + ik_2 3H + ik_3 2H + ik_4 2H \\
&\quad + ik_5 2H + ik_3 (x - 2H) - i\omega t], \\
v_e^{\mathrm{VI}}(t) &= A_0 b_{01} b_{12} b_{23} b_{34} b_{45} a_{56} b_{54} b_{43} b_{32} b_{21} a_{10} b_{12} b_{23} \exp[ik_1 3H + ik_2 3H + ik_3 2H + ik_4 2H \\
&\quad + ik_5 2H + ik_3 (x - 2H) - i\omega t], \qquad (4.12)
\end{aligned}
$$

where the subscripts *a*, *b*, *c*, *d* and *e* correspond to the propagation modes described in Fig. 38.

The transmitted waves at site 15 is obtained in a similar way.

The ratios of the amplitudes calculated from Eqs. (4.9), (4.11) and etc. to that of Eq. (4.8) give the transmission coefficients at sites 5, 10 and 15, respectively. The transmission coefficients thus obtained, which include the effects of multiple reflections inside the concave interface, are shown in Fig. 39(a), (b), (c). In the calculation the contribution of three or more reflections is ignored.

At site 5, the figure shows that the characteristics of the transmission coefficients calculated from Eq. (4.9) are in accord with those obtained from synthetic seismograms at periods longer than 30 s, while the latter has high values with several oscillations at periods from 20 to 30 s, compared to the former. The high values at short periods are considered to arise from the superimposition of SH waves generated at the windward edge (Fig. 40), as is studied later in this chapter.

At site 10, the transmission coefficients with the effects of multiple reflections, calculated from Eq. (4.11), possess a similar trend to that obtained from synthetic seismograms. The theory of multiple reflections introduced here seems to be applicable in this location.

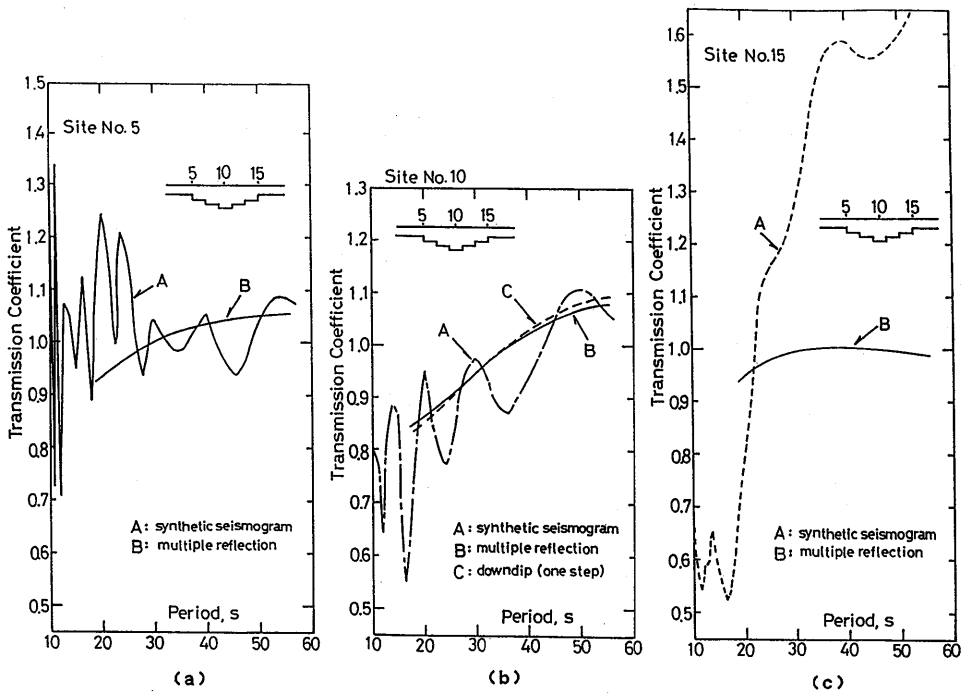

Fig. 39. (a), (b), (c): Transmission coefficients at sites 5, 10 and 15 above the concave interface for Model D. The lines attached to symbol A give the transmission coefficients obtained from synthetic seismograms. Solid lines attached to symbol B are transmission coefficients, which are calculated taking into consideration multiple reflections inside the concave interface, based on equations given in section 4.4 of the text.

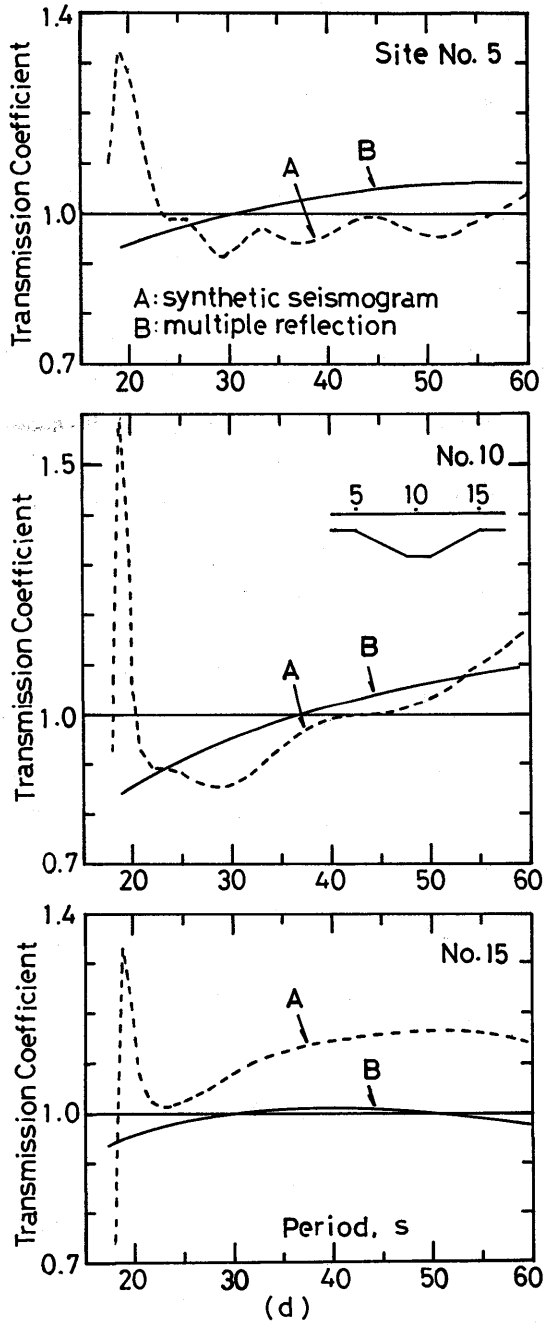

Fig. 39. (d): Transmission coefficients at sites 5, 10 and 15 above the concave interface for Model E. The coefficients obtained from synthetic seismograms are shown by dotted lines and those from the theory of the multiple reflection by solid lines (the values are the same as those given in (a), (b) and (c)).

At site 15, the transmission coefficients with the effects of multiple reflections are drastically different from those obtained from synthetic seismograms. The high amplitudes obtained from synthetic seismograms are caused by factors that at this location, the energy of the scattered waves is concentrated, as previously found in Fig. 29 in Part 3, and that the energy of SH waves tends to radiate much more at long periods, as will be shown in Fig. 40.

On the whole, the transmission coefficients with the effects of multiple reflections can explain those obtained from synthetic seismograms at long periods from 30 to 50 s at site 5, in a whole period range from 20 to 50 s at site 10. However, transmission coefficients with the effects of multiple reflections cannot explain those obtained from synthetic seismograms at short periods from 20 to 30 s at site 5 and in a whole period range from 20 to 50 s at site 15.

These results suggest that interference of body waves converted from Love waves is strong at site 5 at short periods from 20 to 30 s, is weak at site 10 over the entire period range from 20 to 50 s and very strong at site 15 in the entire range, especially at longer periods.

The transmission coefficients computed for the concave structure with smoothly varying layer boundaries (Model E) are shown in Fig. 39(d). The figure shows that, compared to the results for Model D, the characteristics of transmission coefficients obtained from synthetic sesimograms agree very well with those obtained analytically taking into consideration multiple reflections inside the concave structure. Although the transmission coefficients obtained from synthetic seismograms at sites, 5, 10 and 15 are larger than the analytical solutions near 20 s, these large values are considered to arise from interference from short period body waves generated at locations near sites 5 and 10 in downdip propagation (see Fig. 40). The transmission coefficients at site 15, which are slightly larger than the analytical solutions in the entire period range, are also explained by the superimpositions of body waves of long period components generated at locations near sites 10 and 15 in updip propagation (see Fig. 40). These results suggest that transmission coefficients of Love waves over the concave structure whose slopes vary smoothly are, except a few short periods, explained well by the linear theory of multiple reflections.

4.5 Energy of Converted Body Waves

In Fig. 40, the energy of body waves converted from Love waves is shown for the medium with a step of $\alpha=0.67$, 0.75 or 0.80 and also with a step of $\alpha=0.4$. The energy of body waves (B.E.) in percentage is estimated from the following equation (ALSOP, 1966)

$$\text{B.E.}=[1.0-\{(a_1)^2+(b_1)^2\}]\times 100 \tag{4.13}$$

where the energy of an incident mode is assumed to be $\omega/2$. The square of a_1 or b_1 multiplied by $\omega/2$ corresponds to the energy of reflected or transmitted Love waves. The figure demonstrates that the percentage of body waves is high at short periods for downdip propagation while it is high at long periods for updip propagation. We find

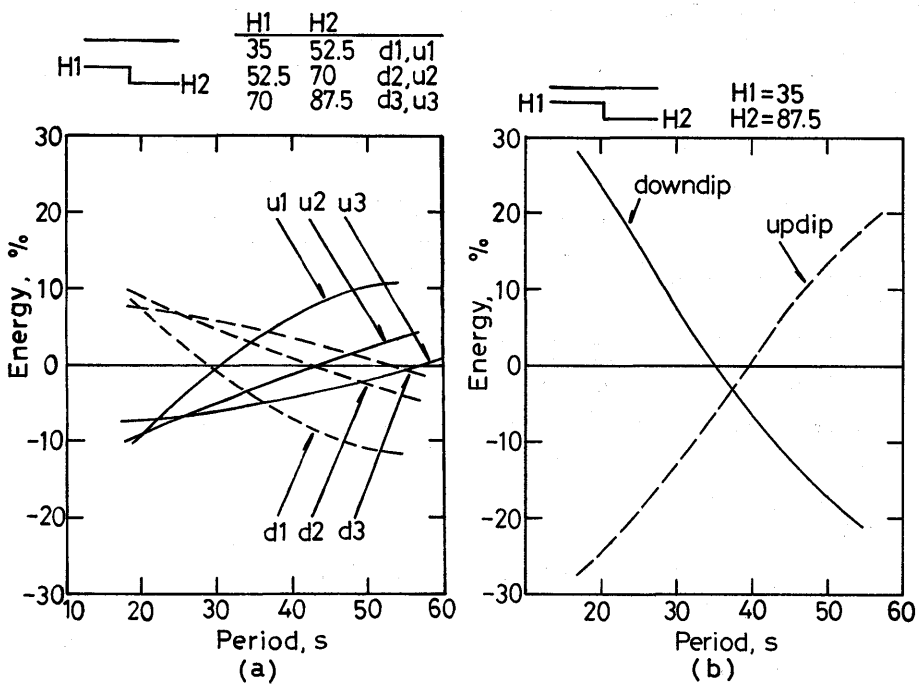

Fig. 40. Body wave energy in percentage for downdip and updip propagations in the media with a step. The energy is computed for (a) $\alpha=0.67$ (d1, u1), 0.75 (d2, u2), 0.80 (d3, u3) and (b) $\alpha=0.4$.

that the period range with a lot of energy of body waves harmonizes well with that indicating anomolously large transmission coefficients obtained from synthetic seismograms. Namely, for a concave structure whose slopes consist of several steps (Model D), the large transmission coefficients with several oscillations at periods from 20 to 30 s at site 5 (Fig. 39) can be explained well in terms of the interference of body waves generating in downdip propagation (Fig. 40). Similarly, the anomaly of large transmision coefficients with increasing period from 20 to 50 s at site 15 (Fig. 39) can be explained well in terms of the increasing energy of body waves with increasing period generated in the updip propagation (Fig. 40). On the other hand, for a concave structure whose slopes consist of oblique lines (Model E), transmission coefficients can be explained well by the theory of multiple reflections, except a few short periods.

The influence of multiple reflections of Love waves and diffracted waves upon transmission coefficients, inside a concave interface, which is discussed in Sections 4.4 and 4.5, are conscisely summarized in Table 3.

At this point, we consider the physical meaning of the energy of body waves. According to ITS and YANOVSKAYA (1983) and ITS (1989), the energy of body waves unacounted for in Eq. (4.2) equals the work done by the stress discontinuity $[p]$ at the $x=0$ interface to produce the displacement discontinuity $[V]$. The

Table 3. Relationship between the transmission coefficients of Love waves above the concave interface of the Moho discontinuity and the effects of multiple reflection of Love waves and diffraction of body waves. The period considered here ranges from about 20 to 50 seconds. Models D and E are shown schematically under the table.

TRANSMISSION COEFFICIENTS ABOVE THE CONCAVE STRUCTURE

LOCATION	WINDWARD	MIDPOINT	LEEWARD
SITE No.	5	10	15
(MODEL D)			
INTERPRETATION BY MULTIPLE REFLECTION	APPLICABLE AT LONG PERIODs	APPLICABLE	NOT APPLICABLE
INTERFERENCE BY DIFFRACTED WAVES	STRONG AT SHORT PERIODS	WEAK	STRONG AT LONG PERIODS
(MODEL E)			
INTERPRETATION BY MULTIPLE REFLECTION	ALMOST APPLICABLE	APPLICABLE	APPLICABLE
INTERFERENCE BY DIFFRACTED WAVES	SLIGHTLY LARGE AT SHORT PERIODS	WEAK	WEAK

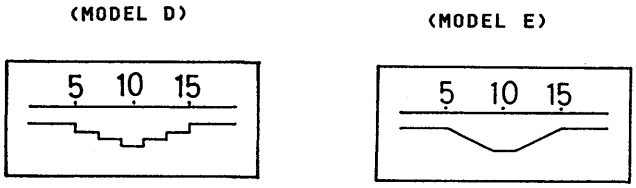

displacement and the stress discontinuities are equal respectively to

$$[V]=V^2_{\text{body}}-V^1_{\text{body}}=\phi^1_1+\sum_{i=1}^{n}a_i\phi^1_i-\sum_{j=1}^{m}b_j\phi^2_j$$
$$[p]=p^2_{\text{body}}-p^1_{\text{body}}=p^1_1+\sum_{i=1}^{n}a_ip^1_i-\sum_{j=1}^{m}b_jp^2_j \tag{4.14}$$

where V_{body} is body wave displacement and p_{body} body wave stress. The work that should be done during a cycle of oscillation to generate these displacements and stress at the portion of the interface formed by a semi-infinite strip of unit width is given by the integral

$$W=(\pi/2i)\int_0^{\infty}([p]^*[V]-[V]^*[p])dz \tag{4.15}$$

where $[V]^*$ and $[p]^*$ are complex conjugtes of $[V]$ and $[p]$, respectively. This work is equal to the difference in the surface wave energy flux (during a cycle of oscillation) to the left (E^1) and right (E^2) of the interface. Namely,

$$E^1 - E^2 = W \tag{4.16}$$

These equations mean that for the positive sign of W, the energy of body waves is greater in medium 2 than for medium 1, while for the negative sign of W, the situation is reversed. Thus, the energy of body waves with a positive sign (Fig. 40) is superimposed on the transmitted waves.

4.6 Coupling between the Fundamental Modes of Love Waves

In Fig. 41, the eigenfunctions of the displacement and stress components computed for several fixed wave numbers (k) or wavelengths (λ) are shown against media with crustal thicknesses of 35 and 87.5 km. The thicknesses are the shallowest and deepest of the concave interface. From the figure we can infer approximately maximum perturbations of the eigenfunctions inside the concave interface.

It should be noted that tangential stress (y_2) is maximum at the Moho discontinuity. Accordingly, the depth with maximum stress changes directly if the depth of the Moho discontinuity changes, while the eigenfunctions of the displacement component (y_1) change more moderately from the surface to deeper parts. These characteristics suggest that the depth of the irregular structure has stronger influences upon the stress component than upon the displacement component.

The figure indicates that the eigenperiod (phase velocity) shifts by about 6.5 (6.0), 9.0 (8.3), 9.3 (8.7) and 8.6% (8.1%) near periods of 20, 30, 40 and 50 s. This means that the eigenfunctions of the displacement and stress components near a period of 40 s (wave number is 0.034758 1/km and wavelength 181 km) are perturbed most significantly. In other words, Love waves at the period are most sensitive to the irregular structure of the concave interface. Considering these shits of the eigenperiods and the dispersion characteristics of the scattered waves clarified in Part 3, it can be concluded that, in the region of the concave interface, the coupling of the fundamental modes of Love waves within a shift of about 9% in the eigenvalues is repeated continuously, suffering both from interference by multiple reflections of Love waves and by body waves generated at irregular layer boundaries.

In Fig. 42, the vertical sections of the underground structures of some regions of Northern America, the Eurasian continent and the southern hemisphere, reproduced from TAKEUCHI (1973), are shown. We find that the irregular concave boundaries of the Moho discontinuity are dominated in many regions under the continental structures. The physical insights quantitatively yielded in Part 4 suggest that Love waves propagating across those concave interfaces, existing in many parts of the great circle path, would suffer interference from both multiple reflections of Love waves and the diffraction of body waves. The intensity of the influences of the two kinds of interference upon the transmission of Love waves depends not only on the site position over the interface but also the period range of the waves.

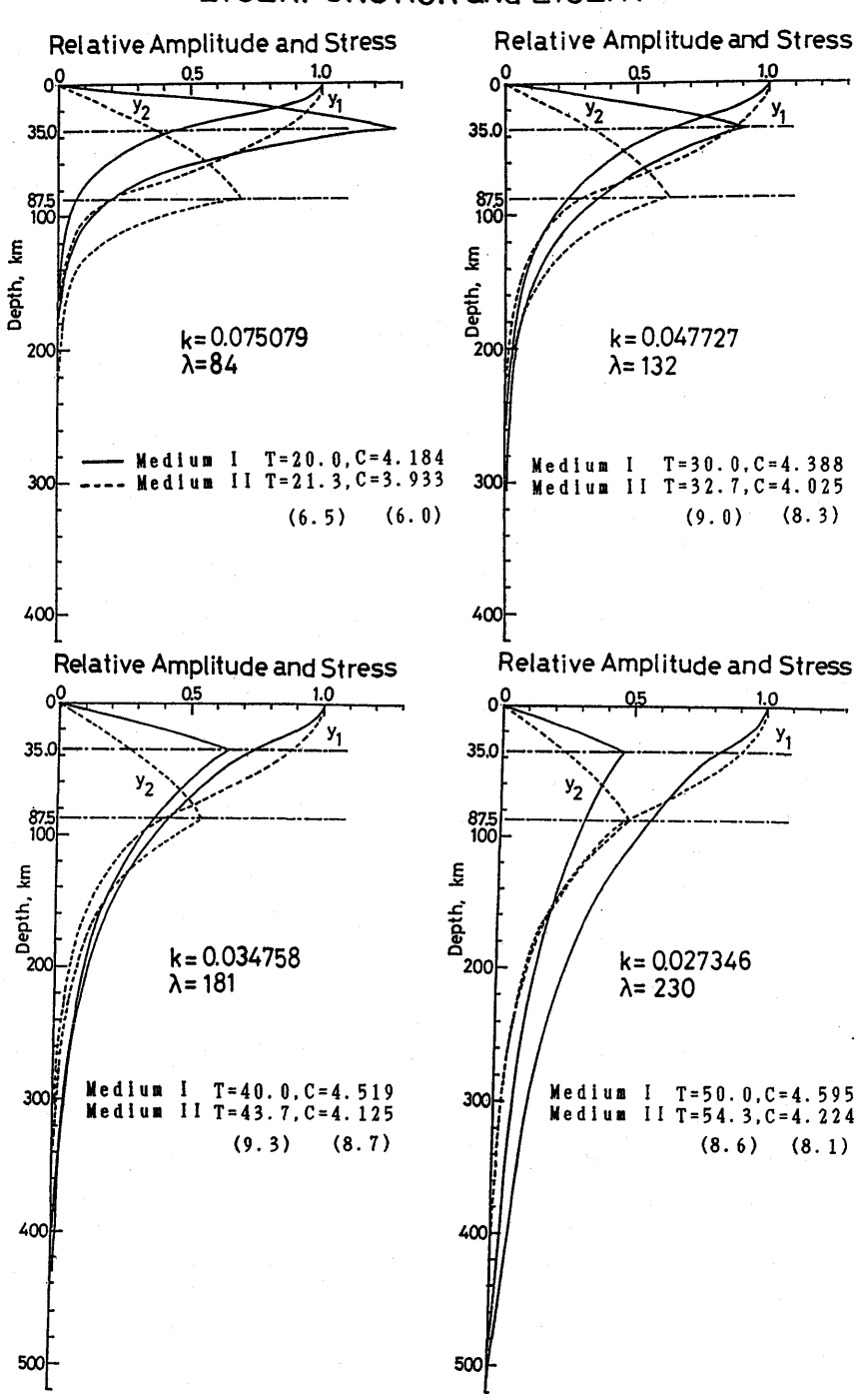
EIGENFUNCTION and EIGENVALUE
Relative Amplitude and Stress
Depth, km
k=0.075079
λ=84
Medium I T=20.0,C=4.184
Medium II T=21.3,C=3.933
(6.5) (6.0)
Relative Amplitude and Stress
k=0.047727
λ=132
Medium I T=30.0,C=4.388
Medium II T=32.7,C=4.025
(9.0) (8.3)
Relative Amplitude and Stress
k=0.034758
λ=181
Medium I T=40.0,C=4.519
Medium II T=43.7,C=4.125
(9.3) (8.7)
Relative Amplitude and Stress
k=0.027346
λ=230
Medium I T=50.0,C=4.595
Medium II T=54.3,C=4.224
(8.6) (8.1)

Fig. 41.

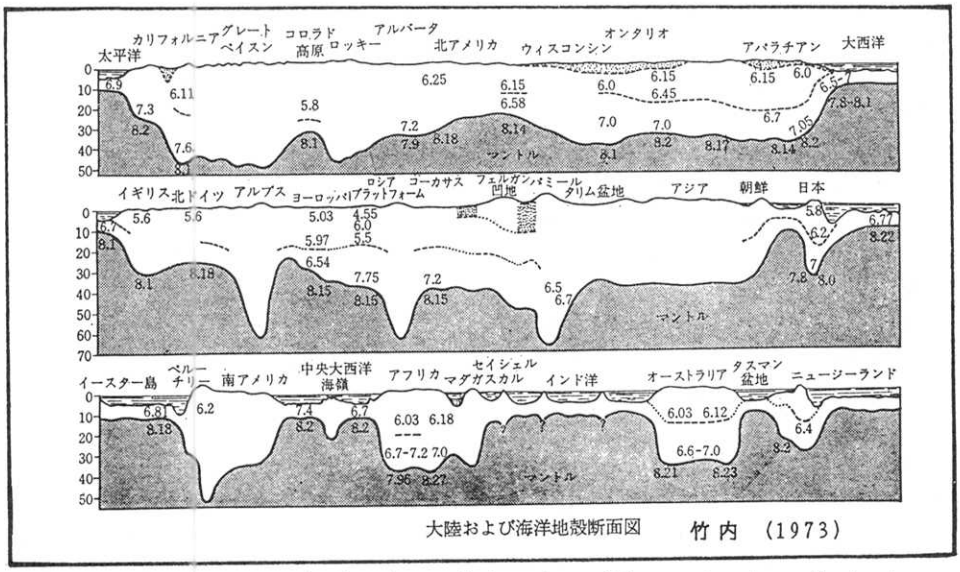

Fig. 42. Schematic map showing the vertical sections of the crust and mantle structures, reproduced from TAKEUCHI (1973). Shown at the top, middle and bottom of the figure are the vertical sections of some parts of the region of Northern America, Eurasian continent and southern hemisphere. Note that the concave interface such as the mountain root structures in which the Moho discontinuity protrudes into the mantle are dominated in many regions under continental underground structures. Numerals in the figure indicate P-wave velocities. The layer boundaries within the crust are denoted by dotted or dashed lines.

4.7 Concluding Remarks of Part 4

The propagation of Love waves in the concave interface with slope angles of 20°–30°, at a period range from 20 to 50 s, has been investigated through transmission and reflection coefficients. The following physical insights are yielded:

For a concave structure whose slopes consist of several steps (Model D);

1) At the midpoint (the site 10) of the concave interface, the transmission coefficients can be explained by introducing the concept of multiple reflections of Love waves over the entire period range. At this location the interference of the diffracted waves is weak.

2) At the windward edge (the site 5) of the concave interface, the transmission

Fig. 41. Eigenfunctions of relative amplitude (y_1) and stress (y_2) components for two medium models with crustal thicknesses of 35.0 (Medium I) and 87.5 km (Medium II). The eigenfunctions for Medium I are plotted by solid lines and those for Medium II by dotted lines. The Moho discontinuities at depth of 35.0 and 87.5 km are marked by dash-dot lines. The wave number (k), wavelength (λ), period (T) and phase velocity (C) are given in units of 1/km, km, s, and km/s, respectively. The relative variations of T and C between the two media are indicated by numerals in parentheses in a unit of percent.

coefficients at long periods can be explained by multiple reflections except at short periods. The interference of body waves is strong at short periods.

3) At the leeward edge (the site 15) of the concave interface, transmission coefficients cannot be entirely explained by multiple reflections because the interference of the diffracted waves is very strong over the entire period range.

For a concave structure whose slopes consist of oblique lines (Model E);

4) The transmission coefficients over the interface can be explained well by the theory of multiple reflections, except at a few short periods.

For both Models D and E;

5) The transmission coefficients at the site 10 are almost equivalent to those for downdip propagation in the medium model with a step, the model consisting of two crustal thicknesses corresponding to the thinnest and thickest of the concave interface.

6) From the distributions of eigenfunctions of the displacement and stress components with depth, the propagation of Love waves in the region of the concave interface can be interpreted such that the coupling of the fundamental modes of Love waves with the shift of several percent in the eigenvalues, such as the period and phase velocity, is continuously repeated (the shift is less than 9%).

7) The interference of body waves is weak for Model E except at a few short periods, but it is strong for Model D at longer periods at the leeward edge.

Part 5

Characteristics of the Propagation of Love Waves in 3-D Irregular Structures of the Moho Discontinuity—Effects of Narrow-Width Heterogeneous Boundaries in the Transverse Direction—

5.1 Introduction

In two-dimensional (2-D) problems associated with Love wave propagation, it is assumed that the background medium is homogeneous in the transverse direction. This case belongs to a general problem of long-period surface wave propagation over the great circle. However, if the mountain root structure with a narrow width in the transverse direction lies on the great circle, it is important to know the effects of the heterogeneous boundary in the transverse direction.

SNIEDER (1986) analyzed the scattering of surface waves in three-dimensional (3-D) media using the Born approximation, based on the far-field Green function. He showed that if the inhomogeneity in the transverse direction is smooth, only the heterogeneity on the source-receiver line influences scattered waves. Modeling 3-D circular cylinders in the crust, BOSTOK (1991) studied the behaviour of scattered far-field amplitudes with azimuth. POLLITZ (1994) used a 3-D scatterer of a circular disk in the crust and examined far-field radiation patterns due to different fault sources.

The present study deals with a special case in 3-D media that the irregular boundary of Moho discontinuity, forming the continental mountain root structure, is strongly dominated in the transverse direction. The characteristics of phase velocities and transmission coefficients of Love waves just over the mountain root, which might be influenced by the coupling of SH and P–SV waves, are investigated using the finite difference method.

5.2 Method

For 3-D media, the basic equation for the displacements u, v, w in the x, y, z directions, respectively, is

$$\begin{aligned}
\rho u_{tt} &= [(\lambda+2\mu)u_x+\lambda v_y+\lambda w_z]_x+[\mu u_y+\mu v_x]_y+[\mu u_z+\mu w_x]_z, \\
\rho v_{tt} &= [(\lambda+2\mu)v_y+\lambda w_z+\lambda u_x]_y+[\mu v_z+\mu w_y]_z+[\mu v_x+\mu u_y]_x, \\
\rho w_{tt} &= [(\lambda+2\mu)w_z+\lambda u_x+\lambda v_y]_z+[\mu w_x+\mu u_z]_x+[\mu w_y+\mu v_z]_y,
\end{aligned} \tag{5.1}$$

Here, ρ denotes density and λ and μ are the Lame' constants. Layer parameters used in Part 1 are lso used in the calcultion. Subscripts denote partial derivatives. A general discussion of the finite difference method for 3-D problems is provided by FRANKEL and VIDALE (1992). The line source condition used is the same as that described in Part 1, in which the fundamental mode Love waves are given as initial values (SUN and MCMECHAN, 1987) along the great circle path including the sites 5, 10 and 15.

To clarify the effects of heterogeneous boundaries in the transverse direction on

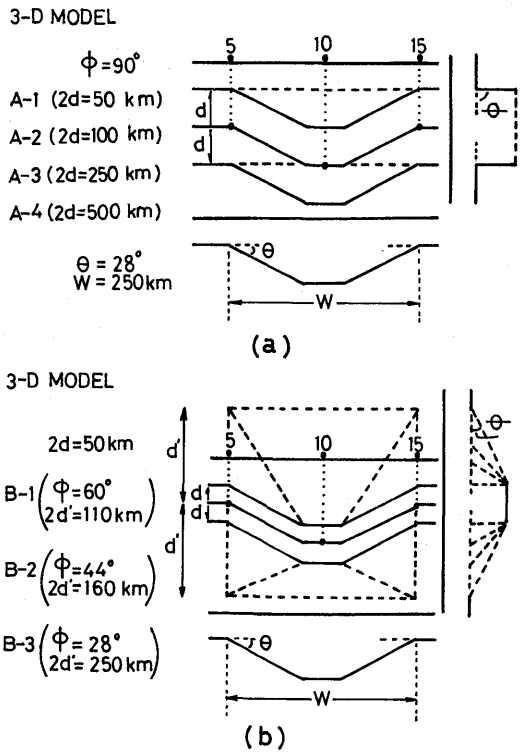

Fig. 43. (a) 3-D Models (A–1, A–2, A–3 and A–4) with vertical heterogeneous boundaries ($\phi=90°$) in the transverse direction. The distance between the great circle path along sites 5, 10 and 15 and the heterogeneous boundary is denoted by d. θ and W at the bottom are the slope angle of the Moho discontinuity and the horizontal length of the mountain root structure. (b) 3-D Models (B–1, B–2 and B–3) with tilted heterogeneous boundaries in the transverse direction. The angle of the tilt is denoted by ϕ. The extension of the bottom in the transverse direction is denoted by d. d' is the maximum extension of the heterogeneous boundary of the Moho discontinuity in the transverse direction. For θ and W, see the caption in (a).

the propagation of Love waves, three kinds of 3-D models of the Moho discontinuity were constructed and are shown in Fig. 43. Using 3-D Model A the effects of spatial distance between the heterogeneous boundary and the great circle path are examined. From 3-D Model B, the effects of the sloping heterogeneous boundary are investigated, with the bottom-area of Moho discontinuity fixed. Through 3-D Model C, the effects of oblique incidence of the waves are studied.

5.3 Results and Discussion

Employing the same method as described in Part 1, we calculated the phase velocity and the transmission coefficient (amplification) over a symmetrical mountain root structure with a steeper slope angle of bout 30°. We analyzed the accuracy of 3-D simulations (Fig. 44). The phase velocities obtained from the nomal mode

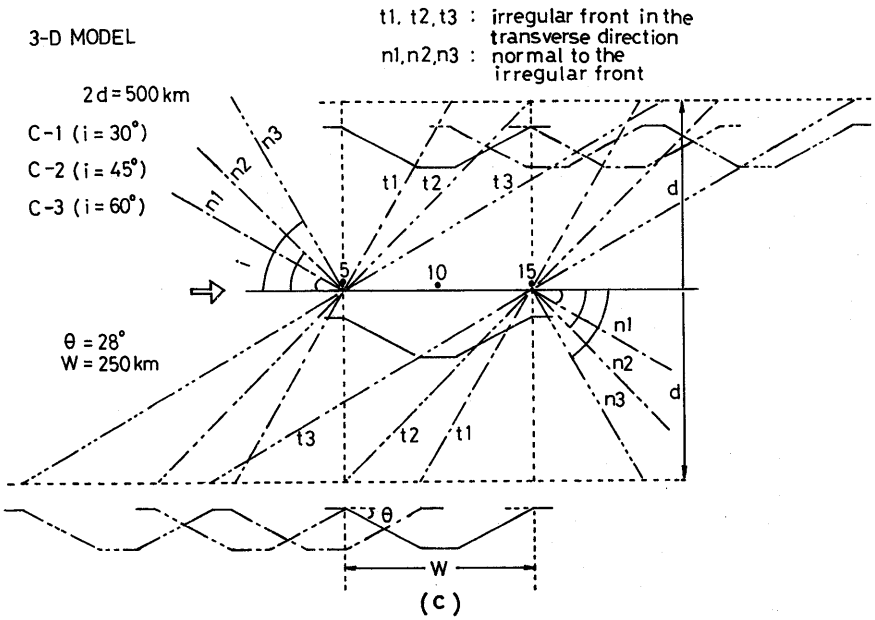

Fig. 43. (c) 3-D Models (C–1, C–2 and C–3) for the oblique incidence of the waves. The irregular fronts in the transverse direction, lying on sites 5 and 15, are denoted by t1, t2 and t3. n1, n2 and n3 are normal to the irregular fronts. The direction of incidence of the waves is indicated by an open arrow and the angle of incidence by i. For θ and W, see the caption in (a).

solution and the amplitude spectrum of the incident waves given as initial values are used for the comparison with the simulated values. The phase velocity and the amplitude spectrum are determined mostly within errors of 1.0% and 2.0%, except a few short periods. This accuracy is almost compatible with that for 2-D simulations.

In Part 1, downdip propagation is defined as wave's trvelling from the thin to thick crust with respect to propagation mode. Updip propagation is defined as the inverse case. Furthermore, we define windward and leeward, respectively, as wave's incoming and outgoing directions.

5.3.1 Characteristics of Phase Velocity Dispersion

Characteristics of the phase velocity dispersion were investigated in detail for 3-D media with the heterogeneous boundaries in the transverse direction.

5.3.1.1 Effects of Spatial Distance between the Heterogeneous boundary in the Transverse Direction and the Great Circle Path

Let d be the distance between the vertical heterogeneous boundary in the transverse direction and the great circle path (Fig. 43(a)) and L_{max} (=250 km) the maximum wavelength of the incident Love waves. Hereafter, we compare the phase velocity characteristics for 3-D media with those for 2-D media in Part 1 (given anew in Fig. 45). Characteristics of phase velocities obtained for 3-D Models (A–1, A–2, A–3 and A–4) are shown in Fig. 46.

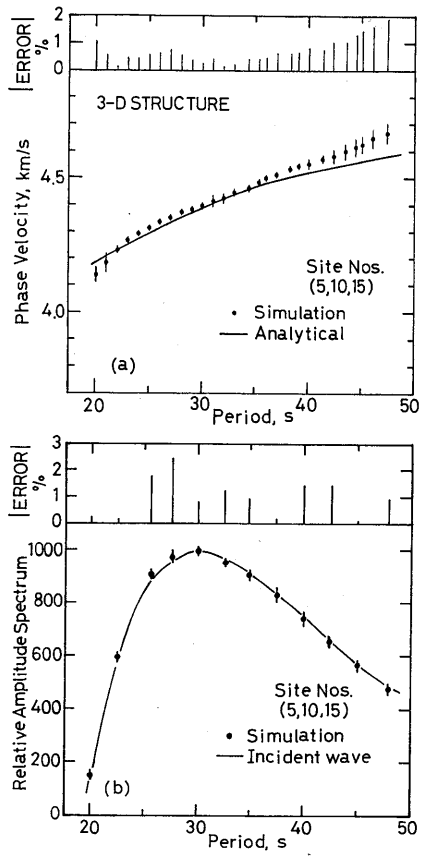

Fig. 44. (a) Phase velocities calculated for a 3-D horizontal structure using the simulated waves at sites 5, 10 and 15 (solid circles). Vertical bars indicate standard errors. Absolute errors are shown at the upper part in percent. A solid line denotes the phase velocities obtained from the normal mode solution for a horizontal structure (shear wave velocities in the crust and the mantle are 3.85 and 4.75 km/s, and the density 3.0 and 3.65 g/cm^3, respectively. (b) Amplitude spectra of simulated waves at sites 5, 10 and 15 (solid circles). Vertical bars indicate standard errors. A solid line denotes the amplitude spectrum of the incident waves given as the initial values. Absolute errors are shown at the upper part in percent.

(a) The case for $d < L_{max}/2$ (3-D Models A–1, A–2)

Over the entire period range, the phase velocity characteristics for 3-D media differ from those for 2-D media. Namely, the phase velocities for the former models are much higher than those for the latter model.

(b) The case for $d = L_{max}/2$ (3-D Model A–3)

The phase velocity characteristics for 3-D media are similar to those for 2-D media.

(c) The case for $d = L_{max}$ (3-D Model A–4)

The dispersion characteristics for 3-D media are equivalent to those for 2-D

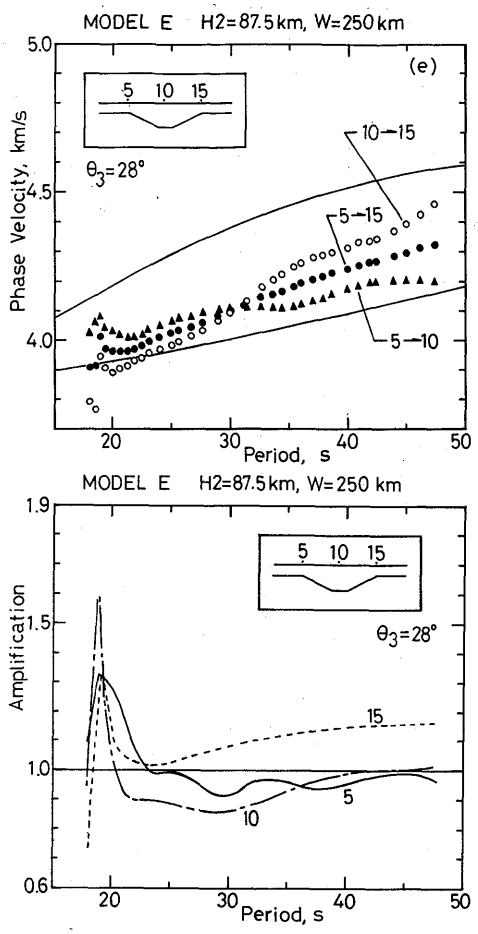

Fig. 45. Characteristics of phase velocities and transmission coefficients (amplifications) for 2-D Model E, respectively given in the top and bottom in the figure. θ_3 indicates the slope angle of the Moho discontinuity in the radial direction in the symmetrical mountain root structure. Upper and lower solid curves in the top figure are theoretical phase velocities calculated for horizontal structures with the thinnest (=35 km) and thickest (H2=87.5 km) crusts, respectively.

media for downdip (sites from 5 to 10), updip (sites from 10 to 15) propagations and entire region (sites from 5 to 15).

The physical indication of these results is that the heterogeneous boundary of Moho discontinuity in the transverse direction does not influence phase velocity characteristics, if the distance between the heterogeneous boundary in the transverse direction and the great circle path is longer than half the maximum wavelength of the incident waves.

5.3.1.2 Effects of Slope Angle of the Heterogeneous Boundary in the Transverse Direction

Let ϕ be the slope angle of the Moho discontinuity in the transverse direction

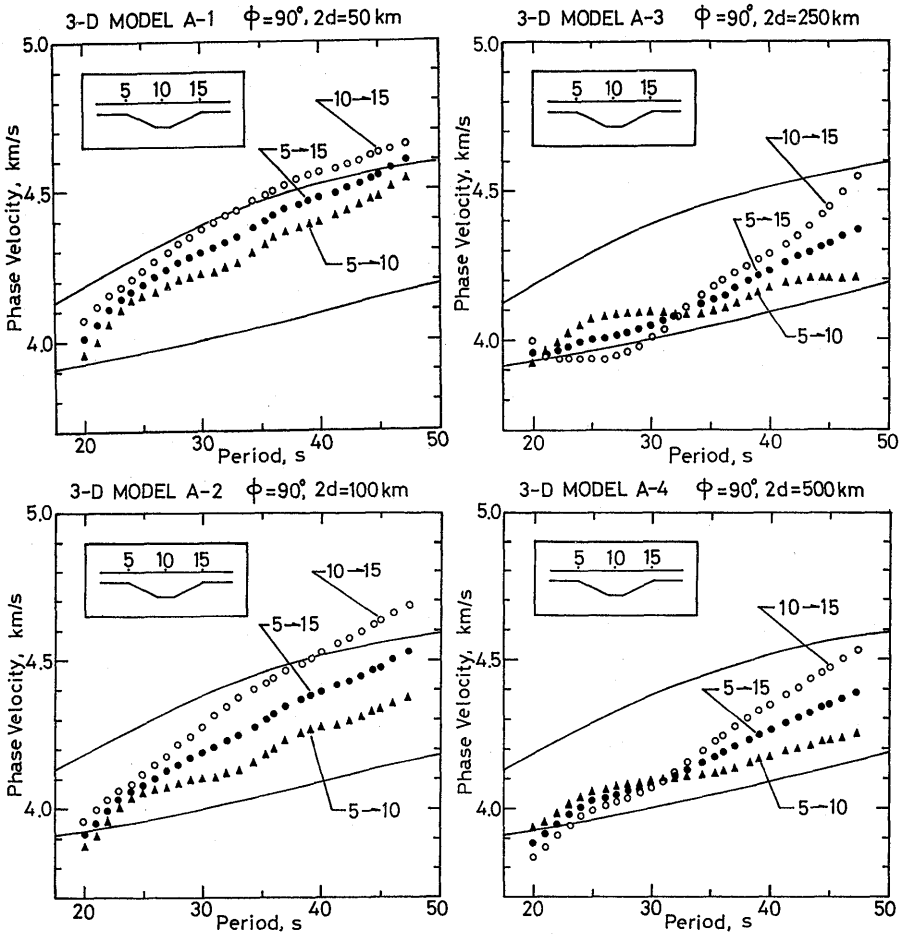

Fig. 46. Phase velocities for 3-D Models A–1, A–2, A–3 and A–4. For two solid curves see the caption in Fig. 45.

measured from the ground surface (Fig. 43(b)). Characteristics of phase velocities obtained from 3-D Models (B–1, B–2 and B–3) are shown in Fig. 47.

(a) The case for $\phi=60°$ and 45° (3-D Models B–1 and B–2)

It has a tendency for the entire period range that phase velocities increase with an increasing slope angle for downdip and updip propagations, as well as for the entire region. Phase velocities are always higher for updip propgation than for downdip propagation. The phase velocity characteristics in this case differ from those for 2-D media, largely at periods shorter than 30 sec.

(b) The case for $\phi=28°$ (3-D Model B–3)

This case corresponds to the symmetrical mountain root structure in both radial and transverse directions, with the central axis located at the site 10. Namely, the horizontal and vertical scales of the heterogeneity are the same in both directions ($2d'=W=250$ km). In this case, the phase velocity characteristics for downdip and

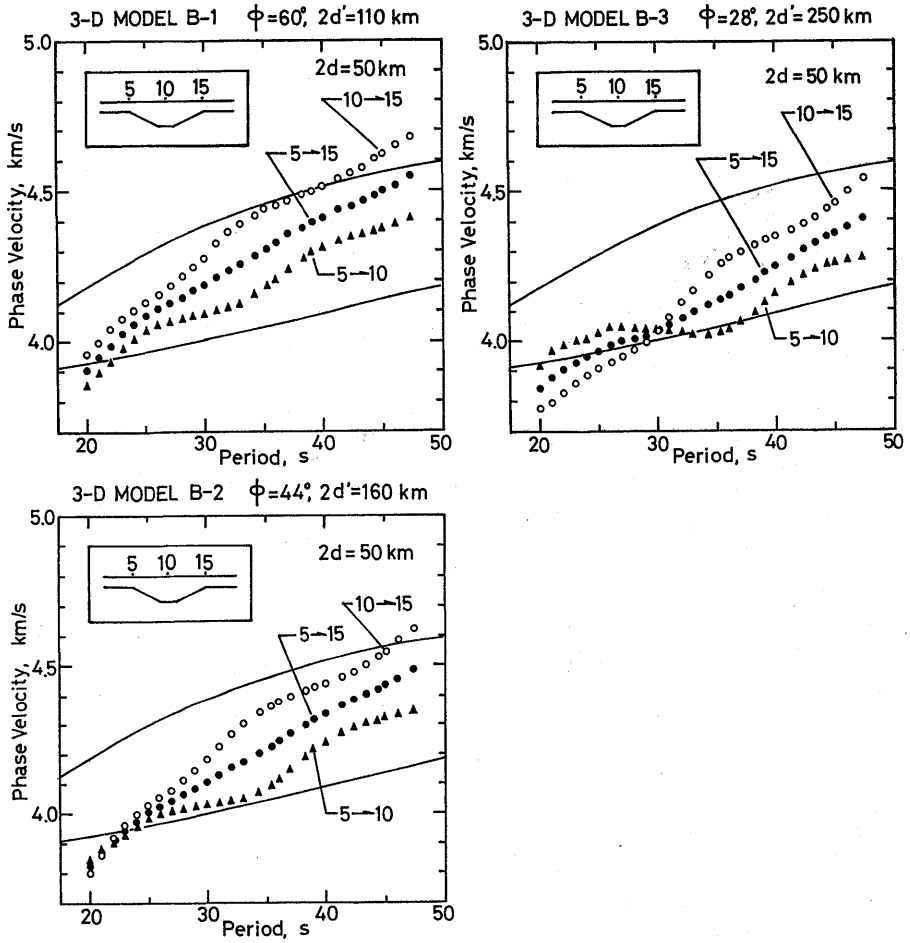

Fig. 47. Phase velocities for 3-D Models B–1, B–2 and B–3. For two solid curves see the caption in Fig. 45.

updip propagations, as well as for the entire region, are similar to those for 2-D media.

The physical indication of these results is that the scattering of Love waves due to lateral heterogeneity in the transverse direction is especially strong at short periods of less than 30 sec. This scattering decreases with the decrease of slope angle of the heterogeneous boundary in the transverse direction. The results suggest that, if the slope angle is less than 30°, the phase velocity characteristics for 3-D media are almost equivalent to those for 2-D media.

5.3.1.3 Effects of the Oblique Incidence of Love Waves in a Heterogeneous Structure in the Transverse Direction

To investigate the effects of the oblique incidence of the waves, we use three 3-D Models C–1, C–2 and C–3 (Fig. 43(c)). These models are constructed by shifting two irregular fronts in the transverse direction at sites 5 and 15 in 3-D Model A–4 towards

the right side. As can be understood from Section 5.3.1.1, the heterogeneous boundary in the transverse direction for 3-D Model A–4 is negligible for the characteristics of phase velocities over the mountain root structure along the great circle path.

Let i be the angle of incidence of the waves. Phase velocities calculated for three-dimensional models are shown in Fig. 48.

(a) The case for $i=30°$ (3-D Model C–1)

The phase velocity characteristics obtained, as a whole, are similar to those for 2-D media. For downdip propagation the phase velocities are slightly lower than those for 2-D media at a period of 35 sec. For updip propagation they are slightly higher than those for 2-D media at periods longer than 35 sec.

(b) The case for $i=45°$ and 60° (3-D Models C–2 and C–3)

The phase velocity characteristics gradually vary at short periods of less than 30

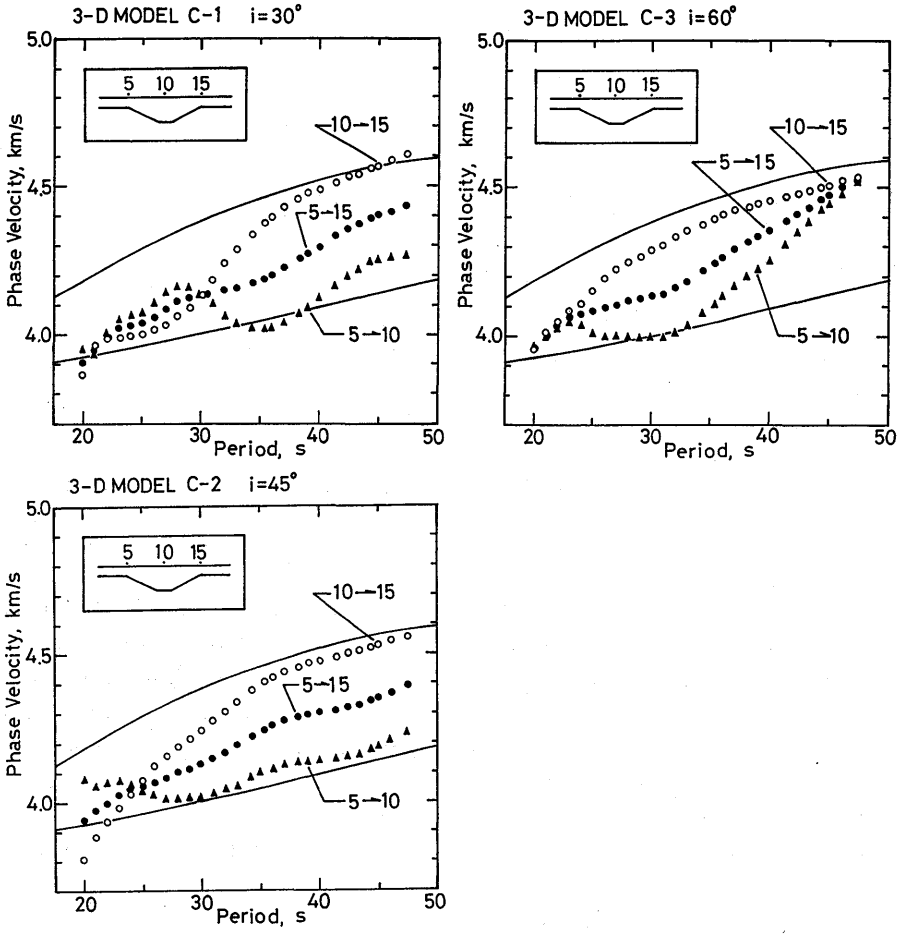

Fig. 48. Phase velocities for 3-D Models C–1, C–2 and C–3. For two solid curves see the caption in Fig. 45.

sec as the angle of incidence increases. For $i=60°$, it is notable that the phase velocities for downdip propagation increase abruptly and approach those for updip propagation at longer periods.

These results physically imply that the effects of oblique incidence greatly influence the phase velocity characteristics for downdip propagation in proportion to the increased angle of incidence, because scattering near the windward edge (at site 5) due to increasing heterogeneity in the transverse direction severely affects the phase components of the waves.

5.3.2 Characteristics of Transmission Coefficients

Following the thread of Section 5.3.1, we discuss in detail the transmission coefficients for three kinds of 3-D Models.

5.3.2.1 Effects of Spatial Distance between the Heterogeneous Boundary in the Transverse Direction and the Great Circle Path

The transmission coefficients obtained for 3-D Models (A–1, A–2, A–3 and A–4) are shown in Fig. 49. Here, we compare the characteristics of transmission coefficients for 3-D media with those for 2-D media (Fig. 45). As defined in Part 1, the coefficients are determined from the ratios of amplitude apectra for 3-D Models mentioned above and those for a 3-D horizontal structure without the mountain root.

At the windward edge (site 5), the transmission coefficients do not vary with variations of d. While at the midpoint (site 10), they decrease by as much as about 0.1 with the increase of d. At the leeward edge (site 15), the transmission coefficients become very large, about 1.4, at periods shorter than 40 sec, which are greater than those for 2-D media, as much as from 0.7 to 0.8. However, when d exceeds half of the maximum wavelength of the incident waves, they approach those for 2-D media.

These results suggest that in the case that d is less than half the wavelength of the incident waves, the short-period diffracted waves travelling round the heterogeneous boundary in the transverse direction strongly influence the amplitude components at the leeward edge.

5.3.2.2 Effects of Slope Angle of the Heterogeneous Boundary in the Transverse Direction

Characteristics of the transmission coefficients obtained for 3-D Models (B–1, B–2 and B–3) with sloping heterogeneous boundaries in the transverse direction are shown in Fig. 50.

At the windward edge (site 5), the characteristics of the transmission coefficients do not show any dependence upon the slope angle and they resemble those for 2-D media. At the midpoint (site 10), the characteristics approach those for 2-D media with the decrease of the slope angle. At the leeward edge (site 15), for the case of the slope angles $i=44°$ and $60°$, the transmission coefficients are very large, about 1.4–1.5 at periods from 20 to 30 sec. With the decrease of the angle, the coefficients approach those for 2-D media.

These results indicate that if the slope angle of the heterogeneous boundary in the transverse direction is less than about $30°$, then the transmission coefficients approach those for 2-D media. In the case with a high slope angle, the amplitude components

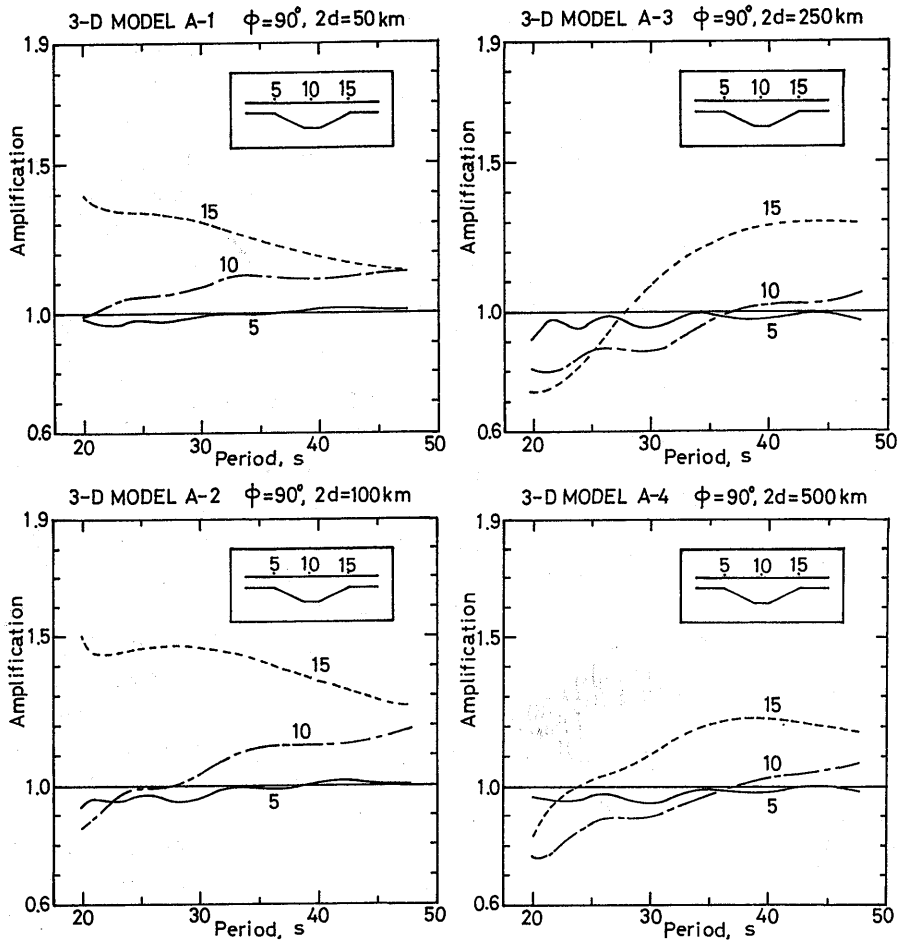

Fig. 49. Transmission coefficients (amplifications) for 3-D Models A–1, A–2, A–3 and A–4.

at the leeward edge, as well as for Models A–1 and A–2, are greatly influenced by the diffracted waves travelling round the heterogeneous boundary in the transverse direction.

5.3.2.3 Effects of the Oblique Incidence of Love Waves in a Heterogeneous Structure in the Transverse Direction

Characteristics of the transmission coefficients obtained for 3-D Models (C–1, C–2 and C–3) for the oblique incidence of the waves are shown in Fig. 51. In this case, the coefficients do not depend on the angle of incidence at any site and are close to 2-D media, except near 20 sec. This results agree well with the analytical and observational studies of oblique incidence for a vertical interface by GREGERSEN and ALSOP (1974).

The physical insight for the these results is that the dependence of the angle of incidence upon amplitude components is very weak, suggesting that the amplitudes of

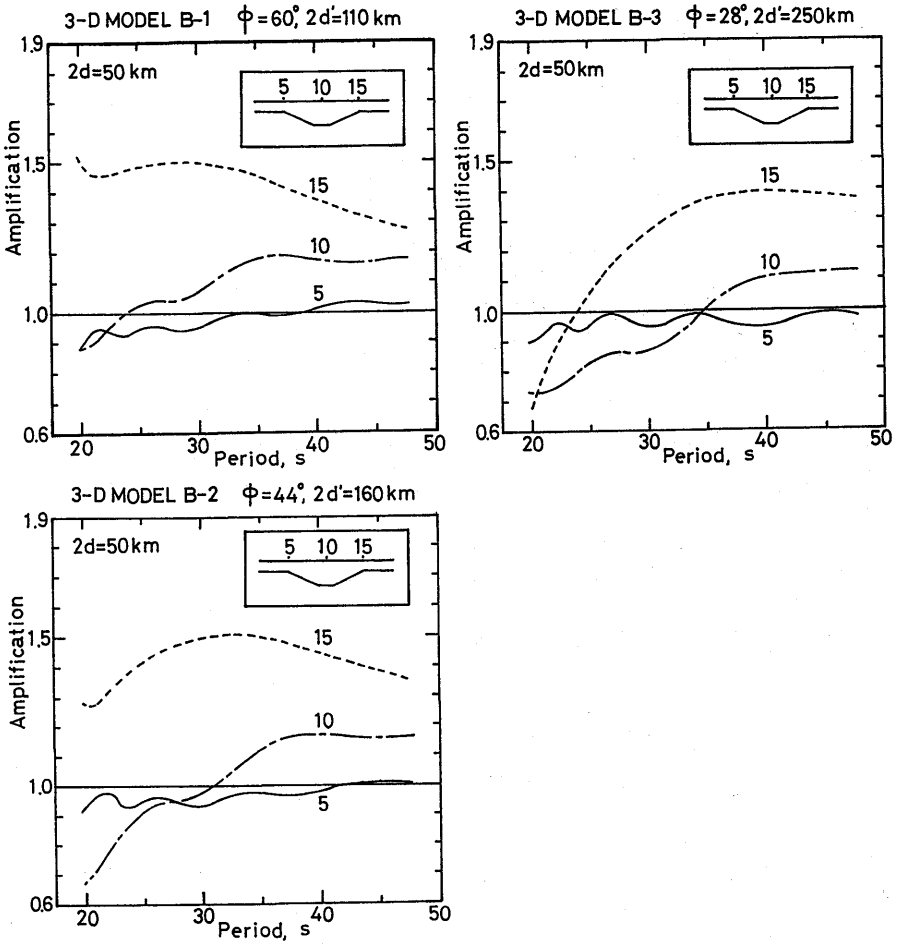

Fig. 50. Transmission coefficients (amplifications) for 3-D Models B–1, B–2 and B–3.

scattered waves are not so different for different angles of incidence. An example of scaterred waves is shown in Fig. 57. As a whole, the large amplitudes of transmission coefficients near a period of 20 sec appeared for 2-D media, which were interpreted as the superimposition of SH waves in Part 4, and do not appear for 3-D media. This phenomenon seems to be caused by the topographical effect that the SH scattered waves generated at the windward edge progress towards the heterogeneous boundary in the transverse direction, thereby the energy of the SH waves do not remain over the mountain root.

From 3-D simulations it was understood that the characteristics of the transmission coefficients for 3-D Models A–3, A–4, B–3, C–1, C–2 and C–3 are almost equivalent to those for 2-D Model E. In Fig. 52, only the transmission coefficients for 3-D Models A–3 and A–4 are shown together with those for 2-D Model E, and also those obtained by taking multiple reflections of Love waves into consideration inside

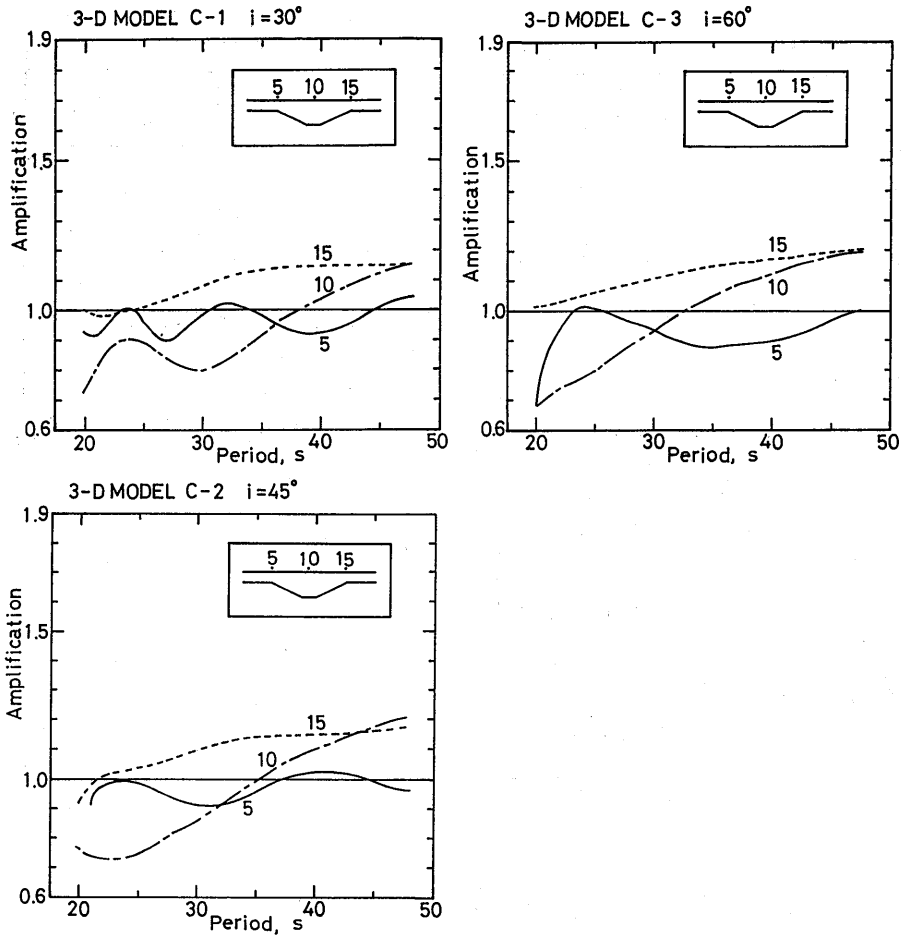

Fig. 51. Transmission coefficients (amplifications) for 3-D Models C–1, C–2 and C–3.

the 2-D mountain root, given in Part 4. The figure clearly shows that the characteristics of transmission coefficients at every site are very similar to each other except near a period of 20 sec. As was described previously, the large amplitudes near that period for 2-D media disappear in 3-D media because SH waves generated at the windward edge (the site 5) go round the heterogeneous boundary in the transverse direction.

5.3.3 Characteristics of Phase Perturbation

In Fig. 53 the phase shift for 2-D media, which is defined in Part 2 as the difference between the phase spectra of the waves for the mountain root and those for a horizontal structure, are reproduced from Fig. 11 in Part 2. Here, we compare the characteristics of phase shift for 2-D media with those for 3-D media. The phase shifts obtained for 3-D Models A, B and C are shown in Figs. 54, 55 and 56, respectively. It is notable that the characteristics of the phase shift for 3-D Models

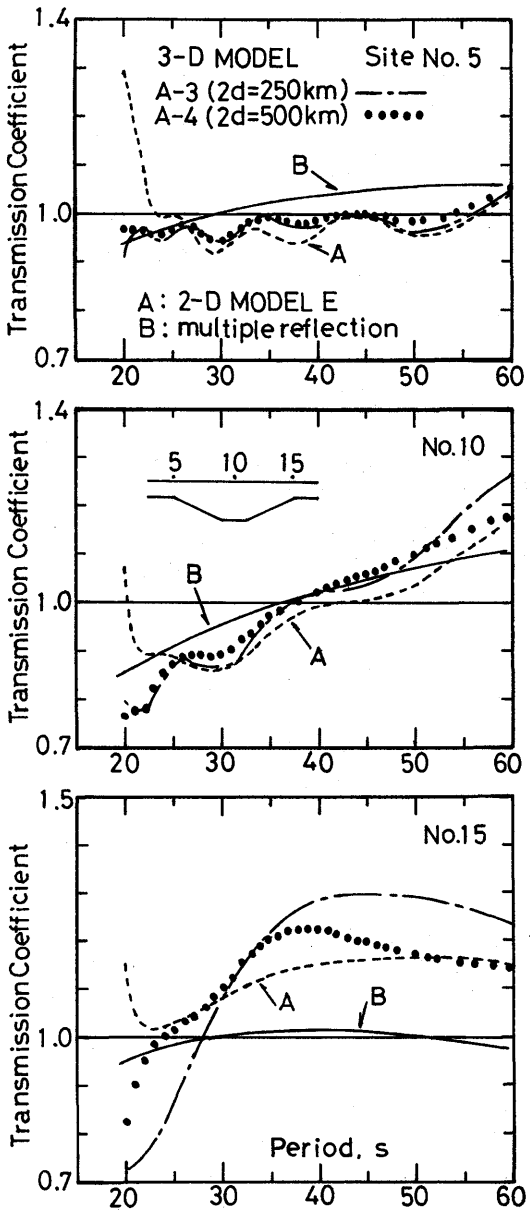

Fig. 52. Transmission coefficients for 3-D Models A–3, A–4 and 2-D Model E, together with those obtained taking the multiple reflection into consideration using the ray theory for 2-D Model E.

A–3, A–4, B–3 and C–1 are very similar to each other, as was observed for the transmission coefficients.

Comparing the phase shifts for these 3-D Models with those for 2-D Model E (Fig. 53), the phase shifts for the former have larger values than the latter at periods

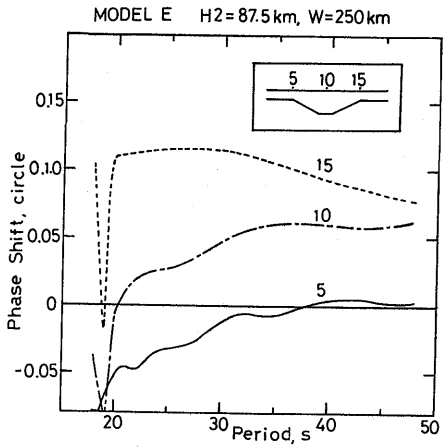
MODEL E H2=87.5km, W=250km
5 10 15
0.15
0.10
0.05
0
-0.05
Phase Shift, circle
15
10
5
20
30
Period, s
40
50

Fig. 53.

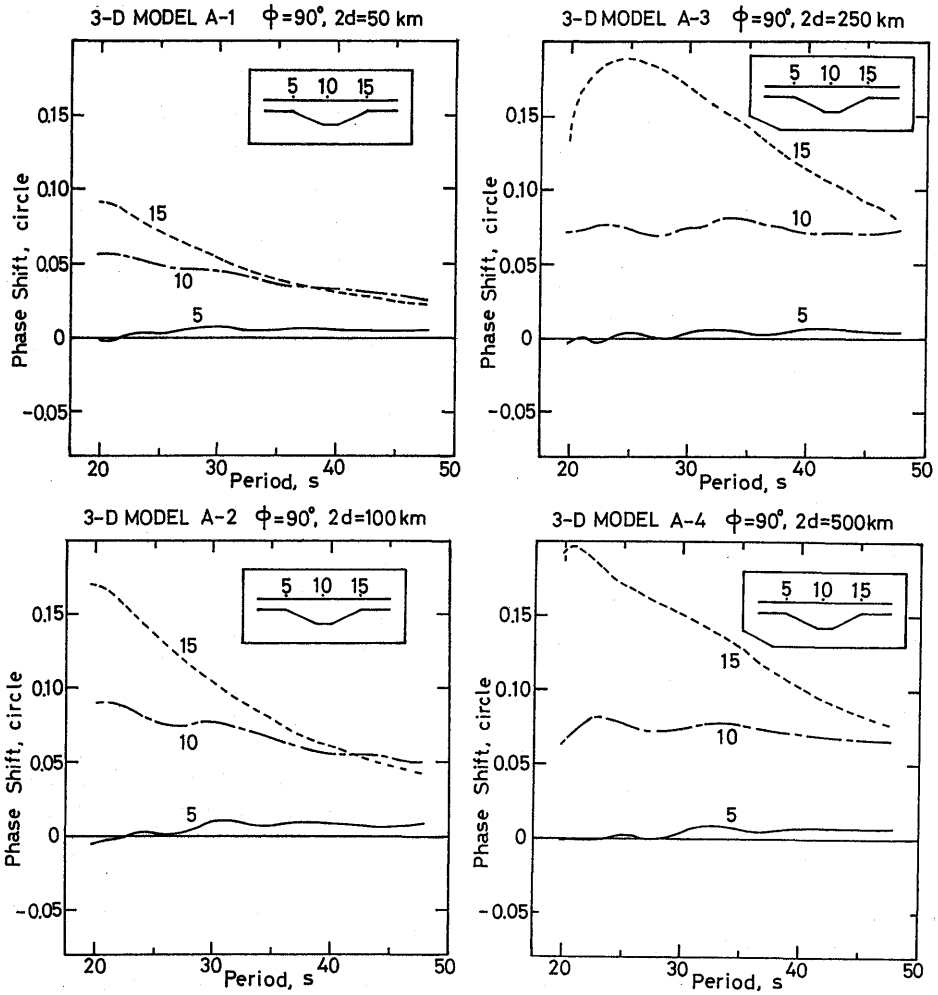
3-D MODEL A-1 ϕ=90°, 2d=50 km
3-D MODEL A-3 ϕ=90°, 2d=250 km
3-D MODEL A-2 ϕ=90°, 2d=100 km
3-D MODEL A-4 ϕ=90°, 2d=500km
5 10 15
0.15
0.10
0.05
0
-0.05
Phase Shift, circle
15
10
5
20
30
Period, s
40
50

Fig. 54.

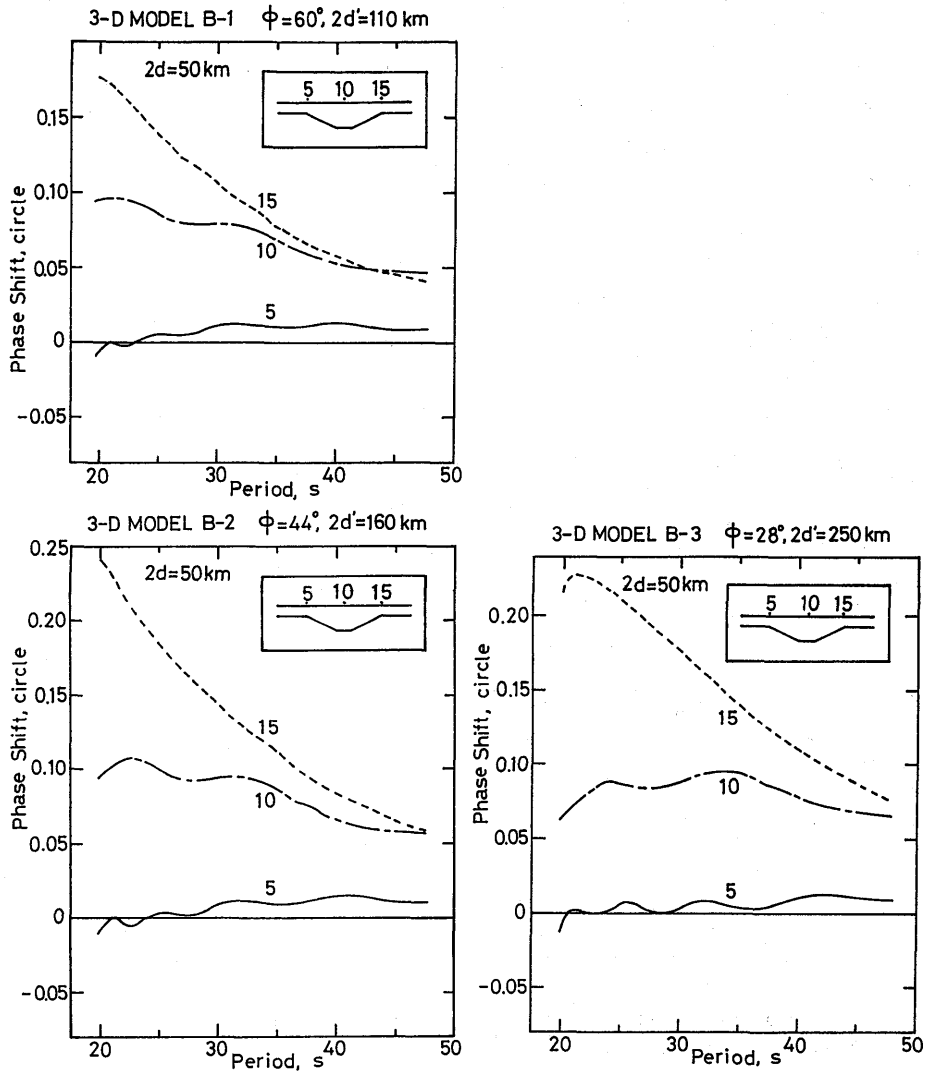

Fig. 55. Perturbation of phase spectra of waves for 3-D Models B–1, B–2 and B–3. For the phase shift see the caption of Fig. 53.

Fig. 53. Perturbation of phase spectra of waves at sites 5, 10 and 15 for 2-D Model E obtained by a Fourier transformation. The phase shift denotes the phase spectral difference between the spectra of waves for the nonuniform wave guide and those for the uniform wave guide in units of a circle (1 circle=2π radian).

Fig. 54. Perturbation of phase spectra of waves for 3-D Models A–1, A–2, A–3 and A–4. For the phase shift see the caption of Fig. 53.

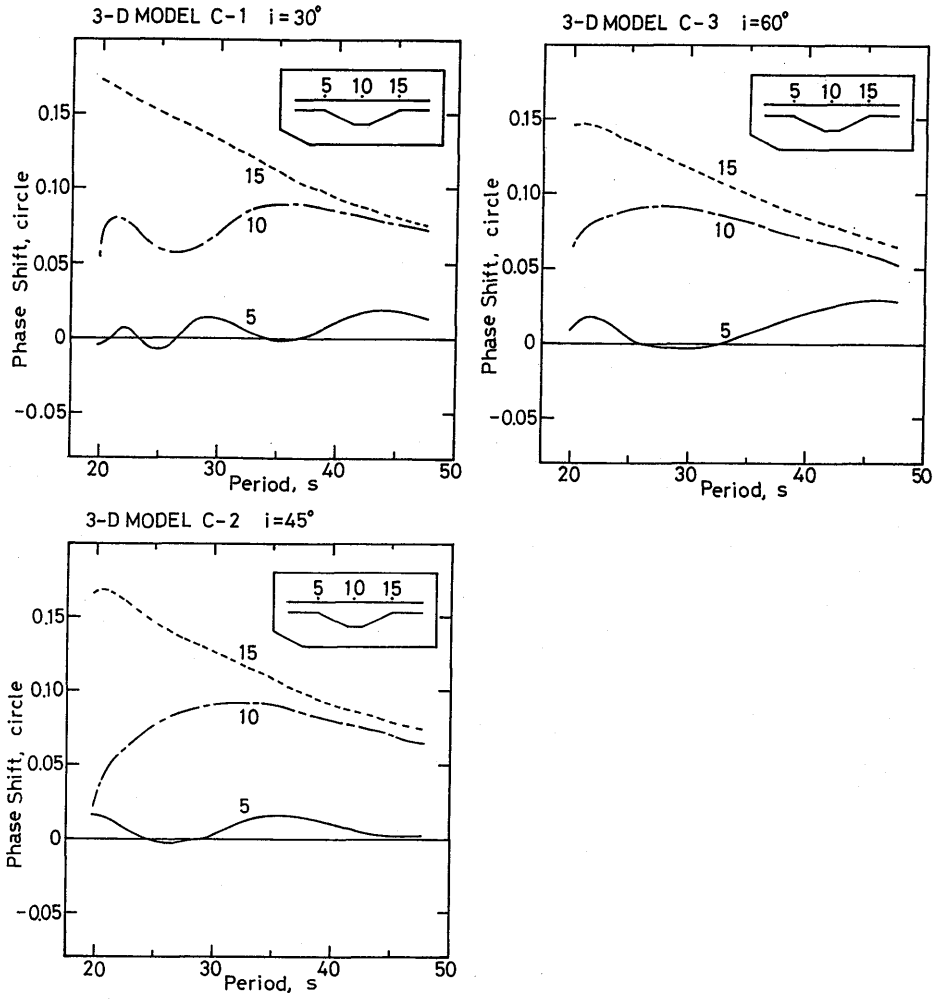

Fig. 56. Perturbation of phase spectra of waves for 3-D Models C–1, C–2 and C–3. For the phase shift see the caption of Fig. 53.

near 20 sec. This phenomenon suggests that SH waves generated at the windward edge directly influence the phase component for 2-D media, decreasing the phase shift. However, the phase components for 3-D media are not influenced by SH waves, because the SH waves can travel along heterogeneous boundaries in the transverse direction.

For 3-D Models A–1 and A–2, phase shifts at site 15 are different from those for 3-D Models A–3 and A–4. The smaller shifts for the former two models suggest that the diffracted waves traveling round the heterogeneous boundaries in the transverse direction are suppressing phase shifts at site 15. The phase shifts at site 15 for 3-D Models B–1 and B–2 with sloping boundaries in the transverse direction are also in the same situation at periods longer than about 35 sec. For 3-D Models C–2 and C–3, the

effects of oblique incidence are especially strong at sites 10 and 5 for angles of incidence of 45 and 60 degrees, respectively. This means that the oblique incidence influences phase components at selected sites along the great circle path over the mountain root.

Figure 57 shows the wave forms for the oblique incidence of Love waves, at sites 5, 10 and 15. The angle of incidence is sixty degrees. In these figures we can see that the waves of radial (RA) and vertical (UD) components, which can be interpreted as SV- and P-waves, respectively, are clearly generated. However, their amplitudes are very small compared to those of transverse components (TR), the maximum amplitudes being less than one tenth that of transverse component.

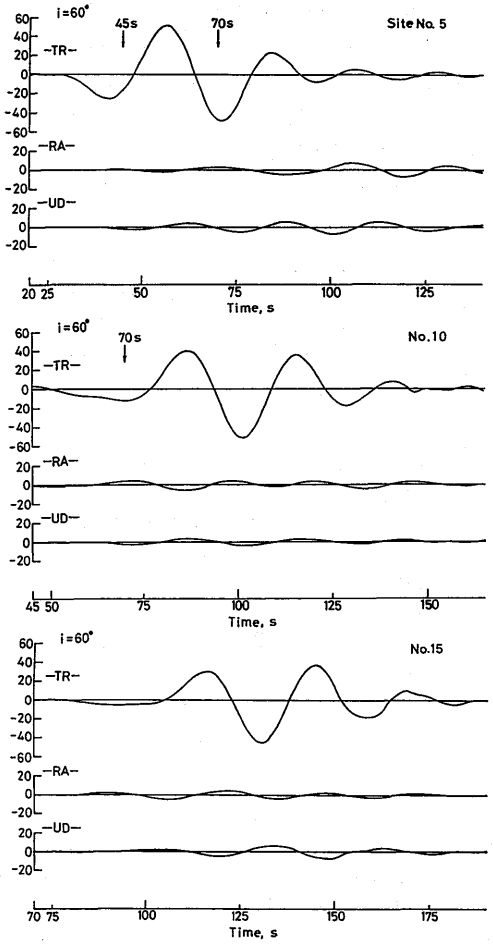

Fig. 57. Wave forms of the transverse (TR), radial (RA) and vertical (UD) components at sites 5, 10 and 15 for the oblique incidence of Love waves. The angle of incidence is sixty degrees (3-D Model C-3). Vertical arrows attached to 45 and 70s at site 5 indicate the start time of the wave plot at sites 10 and 15, respectively.

5.3.4 Distinct Oblique Incidence of Love Waves

In this section, the characteristics of the propagation of Love waves, for grazing and oblique incidences upon irregular fronts of the mountain root, are investigated. For this purpose, 3-D Models Y–1, Y–2 and Y–3, respectively corresponding to the cases of the angles of incidence $i=30$, 45 and 60 degrees were constructed (Fig. 58). These models are different from 3-D Models C–1, C–2 and C–3 (Fig. 43(c)) previously studied in the following geometrical situations. Namely, the great circle paths for the former three models differ from the latter three models. The locations of sites 5, 10 and 15 for 3-D Models C–1, C–2 and C–3, did not vary for different angles of incidence. However, the locations of sites 5′, 10′ and 15′ for 3-D Models Y–1, Y–2 and Y–3, which correspond to the windward edge, the midpoint and the leeward edge of the mountain root structure, respectively, are different for different angles of incidence, except site 5′, because the great circle path depends on the angle of incidence of the waves. The lengths of the great circle path between sites 5′ and 15′ for 3-D Models Y–1, Y–2 and Y–3 are 290, 350 and 500 km, respectively.

Comparing 3-D Models Y–1, Y–2 and Y–3 with 3-D Models C–1, C–2 and C–3, the incident waves for the former three models more strongly graze the surface of the irregular fronts in the transverse direction than for the latter three models, with

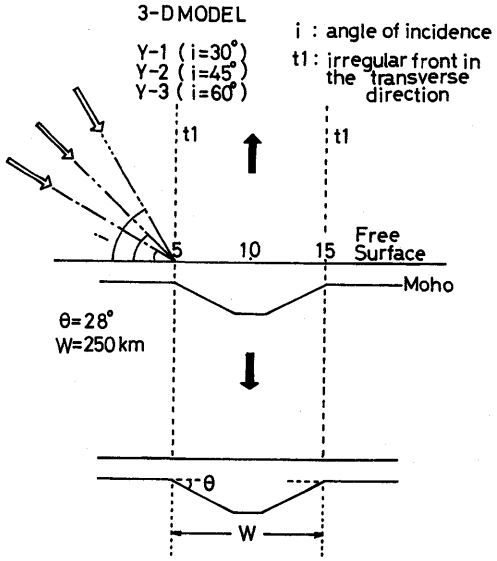

Fig. 58. 3-D Models (Y–1, Y–2 and Y–3) for the grazing and oblique incidence of the waves. The irregular fronts in the transverse direction, lying on sites 5 and 15 (denoted as for 2-D problems), are denoted by t1. The direction of the incidence of the waves is indicated by open arrows and the angle of incidence by i. The great circle path is extended to the direction of the propagation of the waves. Henceforth, the site numbers for windward edge, midpoint and leeward edge of the mountain root structure are denoted anew as 5′, 10′ and 15′. The solids arrows indicate the direction the mountain root extends infinitely. For θ and W see the caption in Fig. 43(a).

increasing angles of incidence.

For 3-D Models Y–1, Y–2 and Y–3 the waves were simulated for sites 5′, 10′ and 15′. The phase velocities (Fig. 59) and the transmission coefficients (amplifications) (Fig. 60) over the mountain root structure were calculated. Their characteristics for $i=30°$ (3-D Model Y–1), as were obtained for 3-D Model C–1, have similar patterns to those for 2-D Model E, although for 3-D Model Y–1 the discrepancy of phase velocities between downdip and updip propagations is rather small and transmission coefficients near 30 sec at the site 15′ are rather large, compared to those for 3-D Model C–1 (Figs. 48 and 51). The characteristics of phase velocities and transmission coefficients for $i=45°$ (3-D Model Y–2) are partly close to those for $i=30°$, but those for $i=60°$ (3-D Model Y–3) are remarkably different from those for $i=30°$.

In Fig. 61 the phase shifts at sites 5′, 10′ and 15′ for $i=30°$, 45° and 60° are shown. The figures show that the characteristics of phase shifts for $i=30°$ (3-D

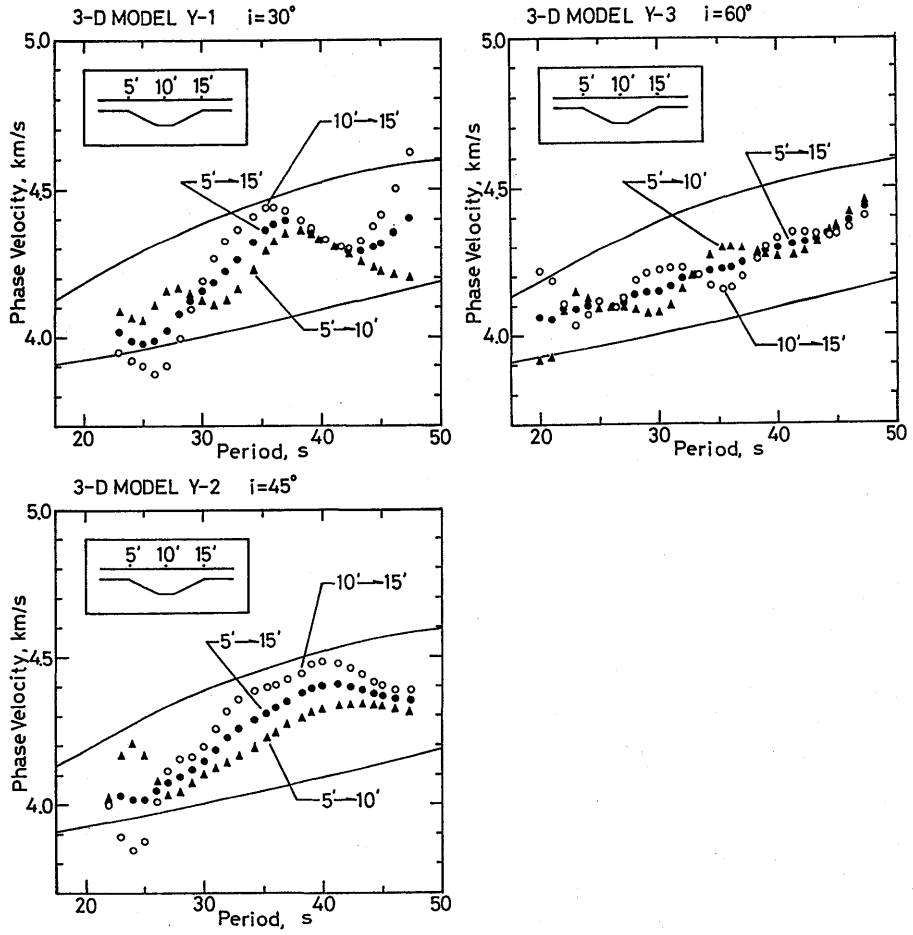

Fig. 59. Phase velocities for 3-D Models Y–1, Y–2 and Y–3. For two solid curves see the caption of Fig. 45.

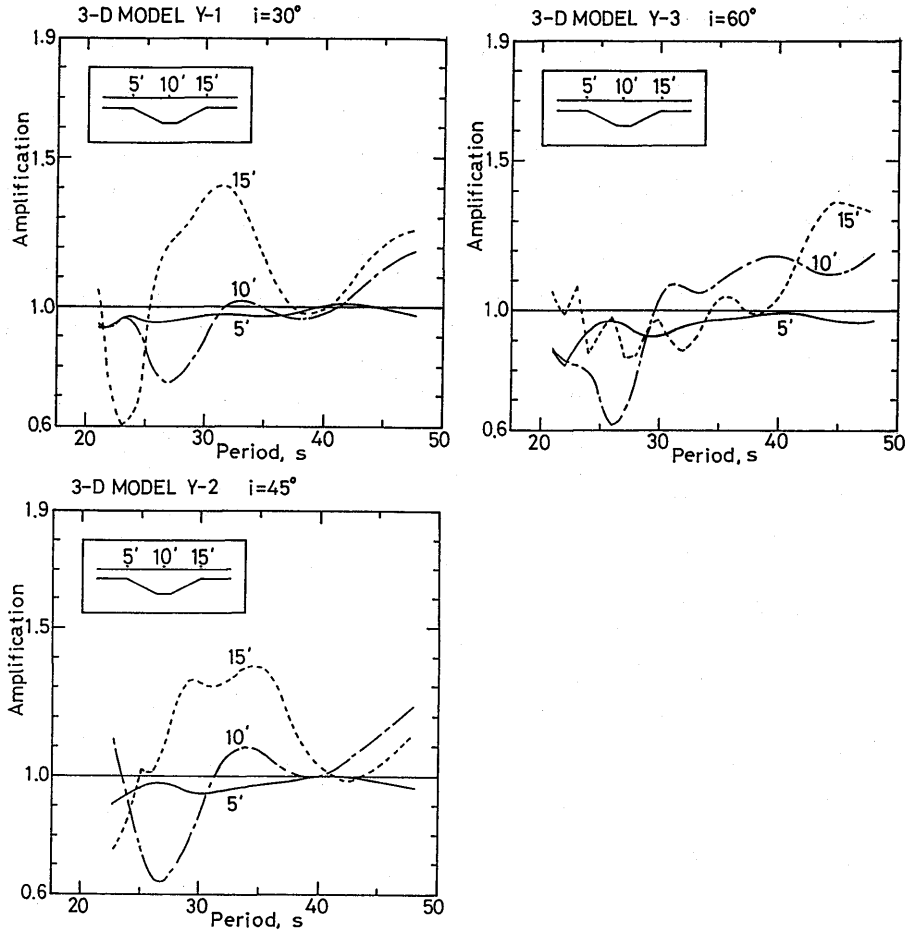

Fig. 60. Transmission coefficients (amplifications) for 3-D Models Y–1, Y–2 and Y–3.

Model Y–1) are closest to those for 3-D Model C–1 (Fig. 56), accordingly to 2-D Model E. With increasing angles of incidence and increasing lengths of great circle path (3-D Models Y–2 and Y–3), the phase characteristics differ from those for $i=30°$, especially at site 15′. It is inferred that the interference of scattered waves generated at irregular boundaries in the transverse direction is strongest at the leeward edge as the angle of incidence increases.

Thus it is concluded from 3-D simulations for 3-D Models Y–1, Y–2 and Y–3 that the information with respect to phase velocities, transmission coefficients and phase shifts over the mountain root structure, obtained for 2-D problems, is approximately applicable to 3-D problems for the grazing and oblique incidences for angles of incidence less than about thirty degrees. With an increasing angle of incidence, the leeward edge suffers most strongly from the influence of scattered waves generated at irregular boundaries in the transverse direction.

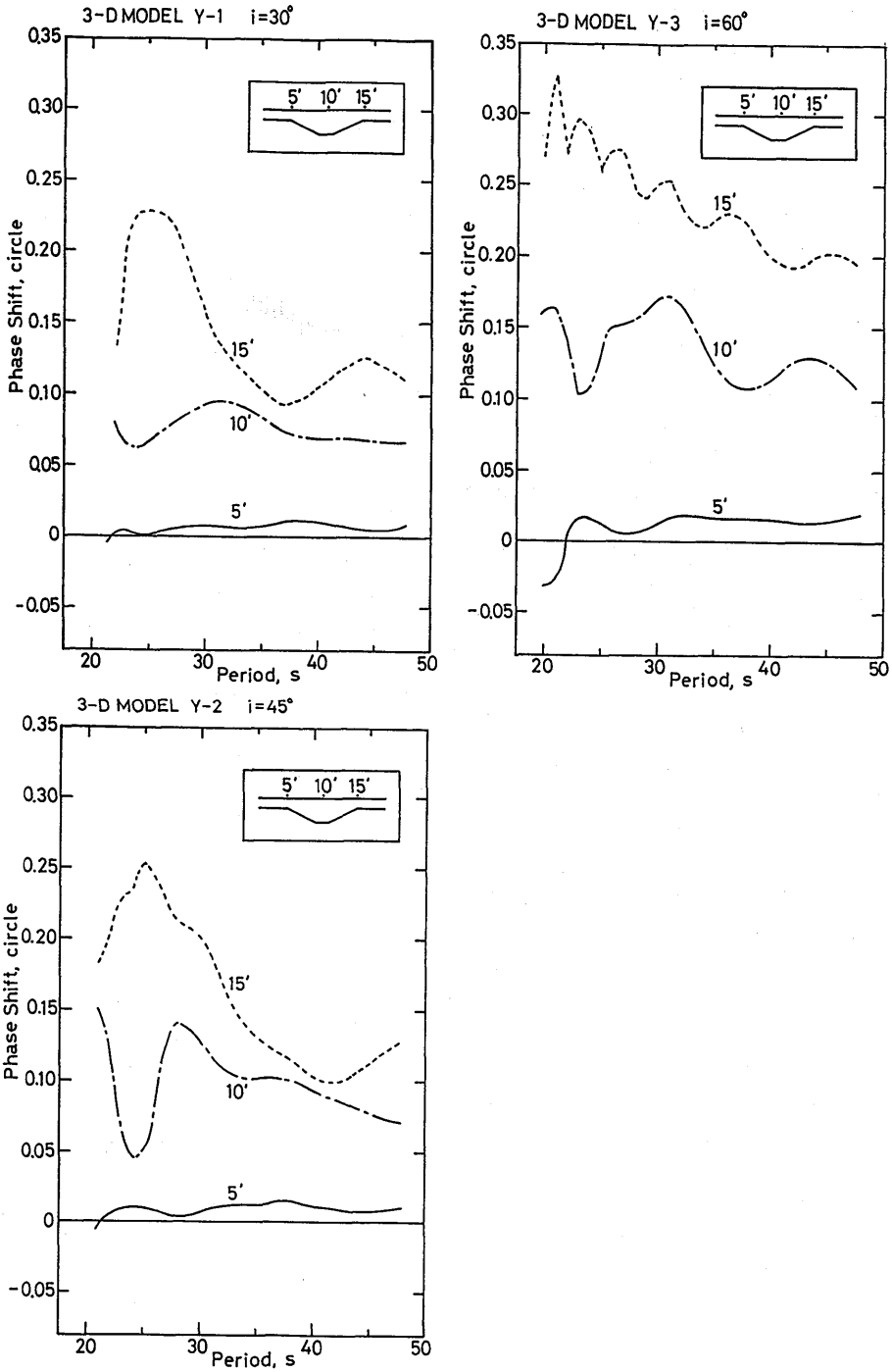

Fig. 61. Perturbation of phase spectra of waves for 3-D Models Y–1, Y–2 and Y–3. For the phase shift see the caption of Fig. 53.

5.4 Concluding Remarks of Part 5

3-D simulations have been performed to investigate the effects of tilted or vertical heterogeneous boundaries of the Moho discontinuity in the transverse direction on Love wave propagation over a mountain root structure. The effects of heterogeneous boundaries are summarized as follows.

Both the characteristics of the phase velocity dispersion and the transmission coefficient for 3-D media are equivalent to those for 2-D media in three cases (1, 2, 3):

1) The vertical boundary in the transverse direction is far from the great circle path, by more than half of the maximum wavelength of the incident waves.

2) The slope angle of the tilted heterogeneous boundary in the transverse direction is less than about thirty degrees.

3) The angle of incidence of the waves, obliquely incident on the heterogeneous front in the transverse direction, is less than about thirty degrees.

4) As far as the oblique incidence is concerned, their effects upon amplitude are very weak. Namely, transmission coefficents do not depend on the angle of oblique incidence.

5) The waves of P–SV components, generated due to the lateral heterogeneous boundaries in the transverse direction, were shown together with dominant Love waves. The maximum amplitudes of the former is less than ten percent of those of the latter.

6) When the effects of the lateral heterogeneous boundaries in the transverse direction are weak, the characteristics of the transmission coefficient at a short period near 20 sec agree well with those obtained from the ray theory of multiple reflections of Love waves inside the mountain root structure, and more finely for 3-D simulations than for 2-D simulations.

Summary of Conclusions

The conclusions obtained throughout Part 1, Part 2, Part 3, Part 4 and Part 5 are summarized as follows.

(1) The phase velocities for downdip propagation are higher than those for updip propagation at short periods. The inverse is true at long periods.

(2) The phase velocities for downdip propagation oscillate several times over the whole period range, while the phase velocities for updip propagation increase monotonously with increasing period, for a concave structure with a set of steps of the Moho discontinuity.

(3) The mean phase velocity dispersion curve across the mountain root structure shows the middle one between the dispersion curves for downdip and updip propagations.

(4) The mean dispersion curve across the mountain root structure does not show the middle one between two typical dispersion curves for the thinnest (S-structure) and thickest (D-structure) crustal structures.

(5) The mean dispesion curve is close to that for the D-structure at short periods and approaches that for the S-structure at long periods.

(6) The mean dispersion curve is explained by the medium made by synthetic elastic parameters using the "weighting coefficient" defined as the ratio of the area of the layer possessing an arbitrary medium to the area of the laterally heterogeneous layer.

(7) The phase velocity anisotropy and the anomaly are caused by spectral phase shifts between the nonuniform and uniform wave guides.

(8) Phase spectral shifts between nonuniform and uniform wave guides are oscillated to a small extent at the windward edge, to some extent at the center and are greatest at the leeward edge along the interface.

(9) The interference between the incident Love waves and the scattered waves generated at the concave interface makes peculiar phase and amplitude distributions on the free surface, as well as near the irregular boundaries of the Moho discontinuity.

(10) Tomographic snap shots of particle displacement show that the amplitude distributions for the nonuniform wave guide at the leeward portions are reversed between ground surface and midcrust. They also show that the continuously extended amplitude distributions in the crust and the mantle are split into two clusters in the deep region.

(11) The interference between scattered waves generated at different locations along the concave interface makes a new incorporated scattered wave.

(12) Scattered waves, consisting of transmiitted and reflected waves and body waves, possess two resonance wavelengths: One is the resonance related only to the uniform waveguide, while the other is that caused by the coupling between the concave structure and the uniform wave guide.

(13) The scattering characteristics of Love waves can be explained by those of long waves at the mouth of estuaries bordering on a continental shelf.

(14) The energy of the scattered waves of Love waves across the mountain root structure on the free surface is largest at the leeward edge, intermediate at the center, and weakest at the windward edge along the concave interface.

(15) At the windward edge of the concave interface, the transmission coefficients at long periods can be explained by multiple reflections. However, the interference of the body waves is too strong to explain the transmission coefficients at short periods.

(16) At the midpoint of the concave interface, the transmission coefficients can be explained by multiple reflections of Love waves over the entire period range. It suggests that the effects of diffraction of body waves are comparatively weak at this location.

(17) At the leeward edge of the concave interface, the interference of the scattered waves is strong at long periods for a concave structure whose slopes consist of several steps, but it is weak for a concave structure whose slopes consist of oblique lines. For the former structure, the transmission coefficients cannot be explained by multiple reflections, while for the latter structure, they can be explained by multiple reflections.

(18) The transmission coefficients at the midpoint of the interface are almost equivalent to those for downdip propagation in the medium model with a step, the model consisting of two crustal thicknesses corresponding to the thinnest and thickest ones of the concave interface.

(19) For a concave structure whose slopes vary smoothly, the transmission coefficients over the interface can be explained well by the theory of multiple reflections, except at a few short periods.

(20) In the process of Love wave propagation across the irregular concave structure, the waves suffer both from interference of multiple reflections of Love waves and the converted body waves. The intensity of the influences of the two kinds of interference upon the transmission of Love waves depends on not only the site position over the interface but also the period of the waves.

(21) Both the characteristics of phase velocity dispersion and the transmission coefficient for 3-D media are equivalent to those for 2-D media in three cases (a, b, c):

(a) The vertical boundary in the transverse direction is far from the great circle path, by more than half of the maximum wavelength of the incident waves;

(b) The slope angle of the tilted heterogeneous boundary in the transverse direction is less than about thirty degrees;

(c) The angle of incidence of the waves, obliquely incident on the heterogeneous front in the transverse direction, is less than about thirty degrees.

(22) Scattered waves of P–SV components, generated due to the lateral heterogeneous boundaries in the transverse direction, were shown together with dominant Love waves. The maximum amplitudes of the former are less than ten percent of those of the latter.

(23) When the effects of heterogeneous boundaries in the transverse direction are weak, the characteristics of the transmission coefficient at short periods near 20 sec agree well with those obtained from the ray theory of multiple reflections of Love waves inside the mountain root, more finely for 3-D simulations than for 2-D ones.

Acknowledgements

The author wishes to express his deepest gratitude to Professors M. Mizoue and T. Yamashita for their support and encouragement throughout this study. Thanks are due to Professor T. Yamashita who read the manuscript and gave many valuable suggestions. The author also wishes to express gratitude to Professors K. Shimazaki, K. Abe, T. Tsukuda and R. J. Geller for their valuable suggestions and encouragment. The author thanks Professors I. Murata, N. Hirata, I. Iwasaki, T. Miytake and H. Kawakatsu for their valuable discussions and suggestions. The author wishes to express thanks to Professors T. Momoi, K. Koketsu and Professor emeritus T. Maruyama for their valuable discussions at the early stage of this study. The author is grateful to Professor emeritus Y. Sato who encouraged him throughout this study

and gave helpful suggestions on the computation method for the normal mode eigenfunction. This study is a Ph.D. Thesis accepted by the Faculty of Science, the University of Tokyo. The computations were carried out at the Earthquake Information Center, the Earthquake Research Institute, and at the Computer Center, the University of Tokyo.

The author is grateful to two anonymous reviewers for their critical reading of the manuscript and to Prof. Y. Sasai and Dr. S. Yoshida for their helpful suggestions in preparing the present paper.

References

ABE, M. and Z. SUZUKI, 1970, A model seismological study on the propagation of Rayleigh waves in a medium with a dipping boundary superficial layer and basement, *Sci. Rep. Tohoku Univ., Ser. 5. Geophys.*, **20**, 1–25.

AKI, K. and K. L. LARNER, 1970, Surface motion of a layered medium having an irregular interface due to incident plain SH waves, *J. Geophys. Res.*, **75**, 933–954.

AKI, K. and P. G. RICHARD, 1980, Quantitative seismology theory and method, Vol. II, 728–729, W. H. Freeman and Company.

ALSOP, L. E., 1966, Transmission and reflection of Love waves at a vertical discontinuity, *J. Geophys. Res.*, **71**, 3969–3984.

BANERJEE, P. K. and R. P. BUTTERFIELD, 1977, Boundary element methods in geomechanics, in Finite Elements in Geomechanics (ed. Gudehus, G.), 529–570.

BARD, P.-Y. and M. BOUCHON, 1980a, The seismic response of sediment-filled valleys. Part 1. The case of incident SH waves, *Bull. Seismol. Soc. Amer.*, **70**, 1263–1286.

BARD, P.-Y. and M. BOUCHON, 1980b, The seismic response of sediment-filled valleys. Part 2. The case of incident P and SV waves, *Bull. Seismol. Soc. Amer.*, **70**, 1921–1941.

BÅTH, M., 1974, Spectral analysis in geophysics, Elsevier, 316–323.

BERG, P., F. IF and O. SKOVGAARD, 1990, A spectral method for seismic wave propagation in an elastic media, *Wave motion*, **12**, 415–427.

BOLT, B. A. and L. A. DRAKE, 1986, Love mode dispersion across subduction zones by finite element modelling, *Geophys. J. R. Astr. Soc.*, **84**, 515–528.

BOORE, D. M., 1970, Love waves in nounuiform guides: Finite difference calculations, *J. Geophys. Res.*, **75**, 1512–1527.

BOORE, D. M., 1972, Finite difference methods for seismic propagation in heterogeneous materials, *Methods Comput. Phys.*, **12**, 1–31.

BOSTOCK, M. G., 1991, Surface wave scattering from 3-D obstacles, *Geophys. J. Int.*, **104**, 351–370.

BOUCHON, M. and K. AKI, 1977, Near-field of a seismic source in a layered medium with irregular interface, *Geophys. J. R. Astr. Soc.*, **50**, 669–684.

BOUCHON, M., 1985, A simple complete numerical solution to the problem of diffraction of SH waves by an irregular surface, *J. Acous. Soc. Amer.*, **77**, 1–5.

ČERVENÝ, V., 1983, Synthetic body wave seismograms for laterally varying layered structures by the Gaussian beam method, *Geophys. J. R. Astr. Soc.*, **73**, 389–426.

CHANG, W. F. and G. A. MCMECHAN, 1989, Absorbing boundary condition for 3-D acoustic and elastic finite-difference calculations, *Bull. Seismol. Soc. Amer.*, **79**, 211–218.

CHEN, W. P. and P. MOLNAR, 1981, Constraints on the seismic wave velocity structure beneath the Tibetan Plateau and their tectonic implications, *J. Geophys. Res.*, **86**, 5937–5962.

CLAYTON, R. and B. ENGQUIST, 1977, Absorbing boundary conditions for acoustic and elastic wave equations, *Bull. Seismol. Soc. Amer.*, **67**, 1529–1540.

CLAYTON, R. and B. ENGQUIST, 1980, Absorbing boundary conditions for wave equation migration, *Geophysics*, **45**, 895–904.

DAUDT, C. R., L. W. BRAIL, R. L. NOWACK and C. S. CHAING, 1989, A comparison of finite difference method and Fourier method calculations of synthetic seismograms, *Bull. Seismol. Soc. Amer.*, **79**, 1210–1230.

DRAKE, L. A. and B. A. BOLT, 1980, Love waves normally incident at a continental boundary, *Bull. Seismol. Soc. Amer.*, **70**, 1103–1123.

DRAVINSKI, M., 1982, Influence of interface depth upon strong ground motion, *Bull. Seismol. Soc. Amer.*, **72**, 597–614.

DRAVINSKI, M. and T. K. MOSSESSIAN, 1987, Scattering of plane harmonic P, SV, and Rayleigh waves by dipping layers of arbitrary shape, *Bull. Seismol. Soc. Amer.*, **77**, 212–235.

DZIEWONSKI, A. M. and A. L. HALES, 1972, Numerical analysis of dispersed seismic waves, in Methods in computational physics, Volume II, editted by B. A. BOLT, Academic Press, 39–85.

FRANKEL, A. and J. VIDALE, 1992, A three-dimensional simulation of seismic waves in the Santa Clara Valley, California, from a Loma Prieta aftershock, *Bull. Seismol. Soc. Amer.*, **82**, 2045–2074.

FUJII, K., S. TAKEUCHI, Y. OKANO and M. NAKANO, 1984, Rayleigh wave scattering at various wedge corners, *Bull. Seismol. Soc. Amer.*, **74**, 41–60.

FURUMURA, T. and H. TAKENAKA, 1992, Numerical simulation and visualizaation of seismic wavefield, Rep. Cent. Infor. Process. Educ., Center for Information Processing Education, *Hokkaido Univ.*, **11**, 25–34.

GELLER, R. J., G. A. FRAZIER and M. W. MCCANN, Jr., 1979, Dynamic finite element modeling of dislocation in a laterally heterogeneous crust, *J. Phys. Earth*, **27**, 395–407.

GILLULY, J., A. C. WATERS and A. D. WOODFARD, 1968, Principles of Geology (3rd ed.), pp. 687, W. H. Freeman, San Francisco.

GREGERSEN, S. and L. E. ALSOP, 1974, Amplitudes of horizontally refracted Love waves, *Bull. Seismol. Soc. Amer.*, **64**, 535–553.

HIGASHI, S. and K. KUDO, 1992, Polarization and frequency-wavenumber spectrum analysis for the strong-motion array data in Ashigara Valley, *Japan, J. Phys. Earth*, **40**, 5–25.

HIGUCHI, S., 1932, Aru hukuzatu na kosei wo yusuru Tihyo ni okeru Love-ha no Denpan ni tutite (On the propagation of Love waves on a free surface over a complicated underground structure), *Zisin*, 1st series, Vol. **4**, 271–274.

HINO, M., 1988, Review—On numerical scheme of non-reflection and free-transmission open boundary, Technical Report, No. 39, Department of Civil Engeneering, Tokyo Institute of Technology, Nov., 1–8.

HISADA, Y., S. YAMAMOTO and S. TANI, 1991, An analytical method for Love wave field generated in alluvial valley and sedimentary basins, *J. Struc. Constr. Engng., AIJ*, **419**, 135–143.

HISADA, Y., K. AKI and T. L. TENG, 1993, 3-D simulations of surface wave propagation in the Kanto sedimentary basin, Japan, Part 2: Application of the surface wave BEM, *Bull. Seismol. Soc. Amer.*, **83**, 1700–1720.

HONDA, S. and H. SAKAI, 1988, Himaraya sanmyaku no keisei II, —Tairiku shoutotsugata zozan undo no mekanizumu—, *Kagaku*, **58**, 570–579.

HORIKE, M., 1988, Analysis and simulation of seismic ground motions observed by an array in a sedimentary basin, *J. Phys. Earth*, **36**, 135–154.

HORIKE, M., H. UEBAYASHI and Y. TAKEUCHI, 1990, Seismic response in three-dimensional sedimentary basin due to S wave incidence, *J. Phys. Earth*, **38**, 261–284.

HUDSON, J. A. and L. KNOPOFF, 1964, Transmission and reflection of surface waves at a corner, *J. Geophys. Res.*, **69**, 275–280.

ISHII, H. and K. YAMAZAKI, 1973, Exact solution of Head and Reflected waves for an SH line pulse source in a dipping layer overlying an elastic media, *Zisin 2*, **26**, 142–159.

ITS, E. N. and T. B. YANOVSKAYA, 1983, Reflection and refraction of surface waves on a curved interface, In: Earthquake prediction and the study of earth structure, Computational Seismol-

ogy, 15, Moscow, Nauka, 87–92 (in Russian).

ITS, E. N. and T. B. YANOVSKAYA, 1985, Propagation of surface waves in a half-space with vertical, inclined or curved interface, *Wave Motion*, **7**, 79–84.

ITS, E. N., 1989, Calculation of Reflection and transmission coefficients, in Seismic surface waves in a laterally inhomogeous Earth, edited by C. I. KEILIS-BOROK, Kluwer Academic Publishers, 112–126.

JACKSON, D. D. 1972, Interpretation of inaccurate, insufficient and inconsistent data, *Geophys. J. R. Astron. Soc.*, **28**, 97–109.

KANAMORI, H., 1982, Chikyu no kouzou, pp. 77, in Chikyu no kagaku 1, edited by UEDA, S. and H. MIZUTANI, Iwaniami Shoten.

KATO, K., K. AKI and T. L. TENG, 1993, 3-D simulations of surface wave propagation in the Kanto sedimentary basin, Japan—Part 1: Application of the surface wave Gaussian beam method, *Bull. Seismol. Soc. Amer.*, **83**, 1676–1699.

KAWASE, H., 1988, Time domain response of a semi-circular canyon for incident SV, P, and Rayleigh waves calculated by the discrete wavenumber boundary element method, *Bull. Seismol. Soc. Amer.*, **78**, 1415–1437.

KAWASE, H. and K. AKI, 1989, A study on the response of a soft basin for incident S, P and Rayleigh waves with special reference to the long duration observed in Mexico city, *Bull. Seismol. Soc. Amer.*, **79**, 1361–1382.

KELLY, D. E., G. G. W. MUSTOE and O. C. ZIENKIEWCZ, 1979, Coupling boundary element methods with other numerical methods: in Development in Boundary Element Methods, Vol. 1, (ed. P. K. BANERJEE and R. P. BUTTERFIELD), Applied Science Publishers, London, 251–285.

KNOPOFF, L. and J. A. HUDSON, 1966, Trasmission of Love waves past a continental margin, *J. Geophys. Res.*, **69**, 1649–1653.

KOKETSU, K., 1987, 2-D reflectivity method and synthetic seismograms for irregulary layered structure—1. SH wave generation, *Geophys. J. R. Astr. Soc.*, **89**, 821–839.

KOKETSU, K. and H. TAKENAKA, 1989, Review: Theories on wave propagation in the near field of seismic waves, *Zisin 2*, **42**, 391–403.

KOKETSU, K., B. L. KENNETT and H. TAKENAKA, 1991, 2-D reflectivity method and synthetic seismograms for irregularly layered structures—II. Invariant embedding approach, *Geophys. J. Int.*, **105**, 119–140.

KOSLOFF, D., M. RESHELF and D. LOEWNTHAL, 1984, Elastic wave calculations by the Fourier methods, *Bull. Seismol. Soc. Amer.*, **74**, 875–891.

LEVANDER, A. R., 1985, Finite difference calculation of dispersive Rayleigh wave propagation, *Techtonophysics*, **113**, 1–30.

LYSMER, J. and L. A. DRAKE, 1971, The propagation of Love waves across nonhorizontally layered structures, *Bull. Seismol. Soc. Amer.*, **61**, 1233–1251.

MAL, A. K. and I. HERREA, 1965, Scattering of Love waves by a constriction in the crust, *J. Geophys. Res.*, **70**, 5125–5133.

MALISCEWSKI, P., 1976, Surface waves in media having lateral inhomogeneities, *Pure and Applied Physics*, **114**, 833–843.

MATSU'URA, M. and N. HIRATA, 1982. General least-squares solutions to quasi-linear inverse problems with a priori information, *J. Phys. Earth*, **30**, 451–468.

MOMOI, T., 1981, Scattering of long waves at the mouth of estuaries bordering on a continental shelf. Part III, *J. Phys. Earth*, **29**, 187–200.

NIAZY, A. and M. N. KAZI, 1980, On the Love wave scattering problem for welded layered quater-spaces with applications, *Bull. Seismol. Soc. Amer.*, **70**, 2071–2095.

OHORI, M., K. KOKETSU and T. MINAMI, 1990, Seismic response analysis of sediment-filled valley due to incident plane waves by three-dimensional Aki–Larner method, *Bull. Earthq. Res. Inst., Univ. Tokyo*, **65**, 433–461 (in Japanese).

POLLITZ, F. F., 1994, Surface wave scattering from sharp lateral discontinuities, *J. Geophys. Res.*, **99**, 21891–21909.

REGAN, J. and D. G. HARKRIDER, 1989, Numerical modelling of SH Lg waves in and near continental margins, *Geophys. J. Int.*, **98**, 107–130.

SAITO, M., 1967, Excitation of free oscillations and surface waves by a point source in a vertically heterogeneous earth, *J. Geophys. Res.*, **72**, 3689–3699.

SAITO, M., 1983, Singular value decomposition and least square method, *Geophys. Explor.*, **36**, 36–48.

SANCHEZ-SESMA, F. J. and J. A. ESQUIVEL, 1979, Ground motion on alluvial valleys under incident plane SH waves, *Bull. Seismol. Soc. Amer.*, **69**, 1107–1120.

SANCHEZ-SESMA, F. J., 1985, Diffraction of elastic SH waves by wedges, *Bull. Seismol. Soc. Amer.*, **75**, 1435–1446.

SANCHEZ-SASMA, F. J., M. A. BRAVO and I. HERREA, 1985, Surface motion of topographical irregularities for incident P, SV, and Rayleigh waves, *Bull. Seismol. Soc. Amer.*, **75**, 263–269.

SANCHEZ-SESMA, F. J., 1990, Elementary solutions for response of a wedge-shaped medium to incident SH and SV waves, *Bull. Seismol. Soc. Amer.*, **80**, 737–742.

SANCHEZ-SESMA, F. J. and M. CAMPILLO, 1991, Diffraction of P, SV, and Rayleigh waves by topographic features: A boundary integral formulation, *Bull. Seismol. Soc. Amer.*, **81**, 2234–2253.

SATO, R., 1961, Love waves propagated across transmitted zone, *Japan J. Geophys.*, **2**, 117–134.

SATO, R., 1966, Group velocity in a layered medium with varying thickness, *Zisin 2*, **19**, 147–148.

SATO, Y., 1955, Analysis of dispersed surface waves by means of Fourier transform I., *Bull. Earthq. Res. Inst., Univ. Tokyo*, **33**, 33–48.

SATO, Y., 1958, Attenuation, dispersion, and the wave guide of the G wave, *Bull. Seismol. Soc. Amer.*, **48**, 231–251.

SATO, Y., 1972, A numerical experiment on wave propagation in an elastic quarter space, *J. Phys. Earth*, **20**, 287–299.

SATO, Y., 1973, Diffraction of SH elastic waves by a crack and the interception of sound by a rigid wall, *J. Phys. Earth*, **21**, 393–400.

SATO, Y., 1978, Dansei hado ron (Theory of elastic waves), Iwanami shoten, 418–420.

SEZAWA, K. and K. KANAI, 1939, On shallow water waves transmitted in the direction parallel to a sea coast, with special reference to Love waves in heterogeneous media, *Bull. Earthq. Res. Inst., Univ. of Tokyo*, **17**, 685–694.

SHINOZAKI, Y., 1988, High frequency response of a sediment-filled valley for incident plane SH waves, Proceedings of the IASPEI/IAEE Joint Working Group on Effects of Surface Geology on Seismic Motion Second Workshop, V, 18.

SMITH, W. D., 1974, A nonreflecting plane boundary for wave propagation problems, *J. Comp. Phys.*, **15**, 492–503.

SNIEDER, R., 1986, 3-D linearized scattering of surface waves and a formalism for surface wave holography, *Geophys. J. R. Astr. Soc.*, **84**, 581–605.

SUN, R. and G. A. MCMECHAN, 1987, Line sourves for seismic modeling by finite difference in a inhomogeneous media, *Geoexploration*, **24**, 183–196.

SUZUKI, T. and M. HAKUNO, 1984, Application of the dynamic finite element metod with non-reflecting boundary for three dimensional wave propagation, *Bull. Earthq. Res. Inst., Univ. Tokyo*, **59**, 327–360.

TAKENAKA, H., 1993, Computational methods for seismic wave propagation in complex subsurface structures, *Zisin 2*, **46**, 191–205.

TAKENAKA, H., 1995, Modeling seismic wave propagation in complex media, *J. Phys. Earth*, **43**, 351–368.

TAKEUCHI, H., 1973, Zisin no kagaku (Science of earthquakes), NHK Shuppan Kabushiki Kaisha, 66–67.

TOSHINAWA, T. and T. OHMACHI, 1992, Love wave propagation in a three-dimensional sedimentary basin, *Bull. Seismol. Soc. Amer.*, **82**, 1661–1677.

TRIFUNAC, M. D., 1971, Surface motion of a semi-cylindrical alluvial valley for incident plane SH waves, *Bull. Seismol. Soc. Amer.*, **61**, 1755–1770.

TSUKUDA, T., 1972, An approximate theory for elastic waves propagated through a heterogeneous medium and its application, *J. Phys. Earth*, **20**, 377–395.

UTSU, T., 1984, Zisingaku, pp. 94, Kyoritsu Zensho.

VIDALE, J. E. and D. V. HELEMBERGER, 1988, Elastic finite-difference modeling of the 1971 San Fernando, California earthquake, *Bull. Seismol. Soc. Amer.*, **78**, 122–141.

VIRIEUX, J., 1984, Wave propagation in heterogeneous media: velocity-stress finite difference method, *Geophysics*, **49**, 1933–1957.

WATERMAN, P. C., 1969, New formulation of acoustic scattering, *J. Acoust. Soc. Amer.*, **45**, 1417–1429.

WATERMAN, P. C., 1976, Matrix theory of elastic wave scattering, *J. Acoust. Soc. Amer.*, **60**, 567–580.

WERNER, D. and E. KISSLING, 1988, A geodynamic model for the lithosphere of the Swiss Alps, *Phys. Earth Planet. Interiors*, **51**, 153–154.

WIGGINS, R. A., 1972, The general linear inverse problem: Implication of surface waves and free oscillations for earth structure, *Rev. Geophys. Space Phys.*, **10**, 251–285.

WONG, H. L., 1979, Diffraction of P, SV, and Rayleigh waves by surface topographies, Dep. of Civil Engng., Report No. CE79–05, Los Angles, Univ. of Southern Cal.

WONG, H. L. 1982, Effect of surface tomography on the diffraction of P, SV, and Rayleigh waves, *Bull. Seismol. Soc. Amer.*, **72**, 1167–1183.

YAMADA, T. and R. SATO, 1976, SH-wave propagation in a medium having step-shaped discontinuity, *J. Phys. Earth*, **24**, 105–130.

YAMANAKA, H., K. SEO and T. SAMANO, 1989, On the seismic motions observed in the southwestern Kanto plain during an earthquake near the Izu-Oshima island, Japan, Proceeding of the national symposium on effects of surface geology on seismic motion, 55–60.

YAMAZAKI, K. and H. ISHII, 1973, Study of phase and group velocities in a dipping layer overlying an elastic medium using theoretical seismograms, *J. Phys. Earth*, **21**, 445–462.

YOMOGIDA, K., 1989, State-of-the-art computational technique for wavefield in laterally heterogeneous media: mainly the Gaussian beam method, *Zisin 2*, **42**, 117–129.

YOSHIDA, M., 1982, Accuracy of the initial phase and the phase velocity of surface waves with special reference to the single station method, *Bull. Earthq. Res. Inst., Univ. of Tokyo*, **57**, 627–652.

YOSHIDA, M., 1983, Surface wave polarization anisotropy in the West Pacific as revealed from group velocities and synthetic waves, *Bull. Earthq. Res. Inst., Univ. Tokyo*, **58**, 571–589.

YOSHIDA, M., 1986, Group velocity partial derivatives of Rayleigh and Love waves near the East Pacific Rise: Modelling the shear wave velocity structures of the asthenosphere, *J. Phys. Earth*, **34**, 427–440.

YOSHIDA, M., 1990a, Characteristics of the vertically heterogeneous and anisotropic plate structure in the Pacific: Implication of the plate thickness, *J. Phys. Earth*, **38**, 57–73.

YOSHIDA, M., 1990b, Trade-off curves on surface wave inverse problems, Programme and abstracts, The Seism. Soc. of Japan, No. 1, 54.

YOSHIDA, M. and I. KAWASAKI, 1991, A density profile of the upper mantle in the Western Pacific as inferred from Rayleigh wave dispersion, *Zisin 2*, **44**, 53–57.

YOSHIDA, M., 1992, Love wave propagation in laterally heterogeneous media: Basin structure (1), Programme and Abstracts The seismological Society of Japan, No. 1, 88.

YOSHIDA, M., 1993, Love wave propagation in laterally heterogeneous media—Phase velocity anomaly of Love waves across a mountain root structure—, *Zisin 2*, **45**, 385–394.

YOSHIDA, M. and A. YAMADA, 1993, Contour detection of underground cylindrical cavities by means of acoustic pulse reflection method, *Jpn. J. Apply. Phys.*, **32**, 2466–2468.

ZAWA, M., 1981, Behavior of the elastic wave propagating through the irregular structures. III. Love waves propagating through the nonhorizontal structures, *Bull. Earthq. Res. Inst., Univ. of Tokyo*, **56**, 761–777.